# INVESTIGATION OF THE PROPERTIES OF FORMAMIDINATE BRIDGED PHOTOACTIVE DIRHODIUM (II,II) COMPLEXES

A Dissertation

by

ELLEN SONG

Submitted to the Graduate and Professional School of
Texas A&M University
in partial fulfillment of the requirements for the degree of

DOCTOR OF PHILOSOPHY

| | |
|---|---|
| Chair of Committee, | Kim R. Dunbar |
| Co-Chair of Committee, | Marcetta Y. Darensbourg |
| Committee Members, | Jean-Phillipe Pellois |
| | Hong-Cai Zhou |
| Head of Department, | Simon W. North |

May 2022

Major Subject: Chemistry

# ABSTRACT

Dirhodium (II,II) molecules are an extensively studied class of metal-metal bonded compounds. The population of a long-lived triplet excited state ($^3$ES) allows for these complexes to be used as photosensitizers for applications such as photodynamic therapy (PDT) or in the construction of dye sensitized solar cells (DSSCs).

Dirhodium partial paddlewheel complexes featuring electron donating bridging ligands and electron accepting chelating diimine ligands have been shown to act as excellent PDT agents due their ability to bind and photocleave DNA as well to generate $^1O_2$ upon irradiation. A mixed bridging ligand compound, $[Rh_2(F_2Form)(OAc)(dppn)_2]^{2+}$ (**2**; $F_2$Form = *N,N'*-2,6-*o*-difluoroformamidinate, dppn = benzo[i]dipyrido[3,2-a:2',3'-c]phenazine) was prepared from the starting material $Rh_2(F_2Form)(OAc)_3$ **(1)** which is the first such partial paddlewheel of its kind with a 1:3 ratio of different bridging ligands. Compound **2** has a relatively high singlet oxygen quantum yield of 0.58(8) and, upon irradiation with visible light, photocleaves plasmid DNA and induces cell death *via* apoptotic and necrotic mechanisms. The photocytotoxicity of **2** against HeLa cells was found to increase by a factor of 25.3 upon irradiation with visible light, an impressive increase compared to related compounds. The mixed bridging ligand motif is a promising platform for the development of novel $Rh_2$-based photosensitizers for PDT applications.

Exploration of the functionalization of the bridging formamidinate ligands was undertaken by systematic investigation of the effect of halogen substitution on the photophysical properties of the dirhodium complexes. The bridging ligands F-Form, Cl-

Form, Br-Form and I-Form were used in the synthesis of series of a homologous series of dirhodium complexes. Single crystal X-ray diffraction, DFT calculations and time-dependent NMR studies revealed differences in the lability of coordinating solvent ligands and trends in electronic structure.

The ability to functionalize the coordinating ligands of the dirhodium core allows for convenient modification of the complex for other applications. Carboxylic acid functionalized, axial blocking ligands were used to prepare formamidinate bridged dirhodium complexes. The carboxylic acid substituent allows the complexes to bind to $TiO_2$ or NiO and act as photosensitizers in the construction of dye-sensitized solar cells. Methods to tune the coordinating ligands and improve the photosensitizing properties of these complexes as well as to introduce new functionalities are described in this dissertation.

# DEDICATION

To my parents for their unwavering love and support in my growth as a scientist.

# ACKNOWLEDGEMENTS

First and foremost, I would like to thank my advisor Professor Kim R. Dunbar for giving me the opportunity and independence in her group to explore my areas of interest as a synthetic inorganic chemist. This work would not be possible without her. Professor Dunbar's passion for fundamental research is prevalent every day and I thank her for all of her guidance and mentorship these past number of years, which has truly helped me develop as a scientist.

A long-time collaborator of the Dunbar group, Professor Claudia Turro at the Ohio State University has been a key part of my learning and development as a chemist as well. Thank you for providing guidance and advice and helping me reach a greater understanding of inorganic photochemistry.

I would also like to thank my committee co-chair Professor Marcetta Y. Darensbourg for her feedback and support during my time at Texas A&M University. I am grateful for her welcoming me to her group meetings and allowing me an avenue to broaden my scientific scope. Thank you as well to my committee members Professor Jean-Philppe Pellois and Professor Hong-Cai Zhou. In particular, Professor Pellois opened his laboratory and space to me, and provided valuable input on the biological aspects of this work.

I am grateful that I was lucky to spend many years in such a collaborative and welcoming environment in the Dunbar Group at Texas A&M. Thank you to my lab mates past and present: David Kempe, Francisco Birk, Sayan Saha, Brian Dolinar, Dimitrios

Alexandropoulos, Haomiao Xie, Sayan Saha, Vignesh Radhakrishnan, Mukesh Singh, Eryn White, Kelsey Schulte, Haomiao Xie, An Vu, Ryan Coll and Junjie Huang. I was privileged to have mentored excellent undergraduate students during my time here, and I would like to acknowledge the work of Santiago Quevedo and Benjamin Clayville. In particular, I would like to recognize my lab mate Agustin Millet, with whom I collaborated closely. I thank him being someone with who I could always share ideas with, for his friendship and for always bringing the fun to science.

During my time in the Department of Chemistry, I am grateful to have had many opportunities for personal and professional development. My time volunteering with many outreach events have only confirmed my passion for science and I am so grateful for the many relationships and friendships I was able to build through these experiences. I would also like to thank Sandy Horton in the graduate office for all the advice and guidance she has provided.

I deeply appreciate my friends and loved ones, near and far. To those back home in Canada and to those I met in Texas, your unwavering friendship and belief in me mean so much. I am so lucky to have made so many memories and shared so many experiences. Thank you.

Finally, I would like to thank my family, Jun, Lihua and Michelle. Thank you to my parents Jun Song and Lihua Fan for encouraging my love of science since I was a child. I would not be here pursing my goals if it were not for their unconditional love and support, and it is to them I dedicate this dissertation.

CONTRIBUTORS AND FUNDING SOURCES

## Contributors

This work was supervised by a dissertation committee consisting of Professor Kim R. Dunbar of the Department of Chemistry as committee chair, Professor Marcetta Y. Darensbourg of the Department of Chemistry as committee co-chair, and Professor Hong-Cai Zhou of the Department of Chemistry and Professor Jean-Philippe Pellois of the Department of Biochemistry and Biophysics as committee members.

The biological studies presented in Chapter II were performed in collaboration with Professor Jean-Philippe Pellois in the Department of Biochemistry and Biophysics at Texas A&M University. The confocal microscopy and flow cytometry studies were performed with help from Dr. Helena Kondow-McConaghy in the Pellois Group. The time-resolved experiments were performed by Dr. Congcong Xue and Sean Steinke from the Turro Group at the Ohio State University

The crystallographic refinements reported in Chapter III were performed with help from Dr Haomiao Xie from the Dunbar group.

The preliminary synthesis of the complexes discussed in Chapter IV were developed and performed in collaboration with Dr Agustin Millet in the Dunbar group. The crystallographic data were collected at the Advanced Photon Source at Argonne National Laboratory.

Computational calculations were performed with computing time and software provided by the High Performance Research Computing Center at Texas A&M University

as well as with support provided by Dr Lisa M. Perez at the Laboratory for Molecular Simulation in the Department of Chemistry at Texas A&M University. Mass spectrometry experiments were performed by the Laboratory for Biological Mass Spectrometry at Texas A&M University.

All other work conducted for the dissertation was completed by the student independently.

**Funding Sources**

Graduate studies were supported by funds from the Welch Foundation (Grant Number A-4449) and the National Science Foundation (Grant Number CHE-2102508).

The Advanced Photon Source at the Argonne National Laboratories is a U.S. Department of Energy (DOE) Office of Science User Facility operated under Contract Number DE-AC02-06CH11357. ChemMatCARS Sector 15 is supported by the National Science Foundation under Grant Number NSF/CHE-1346572.

The X-ray diffractometers and crystallographic computing systems in the X-ray Diffraction Laboratory at the Texas A&M University Department of Chemistry were purchased with funds provided by the National Science Foundation (CHE-9807975, CHE-0079822, and CHE-0215838).

TABLE OF CONTENTS

Page

LIST OF FIGURES

Page

LIST OF TABLES

Page

# CHAPTER I

# INTRODUCTION

## Metal-Metal Bonding

The first metal-metal multiple bond was described by Prof. F.A. Cotton in 1964 in his highly influential publication featuring the crystal structure of the octachlorodirhenate anion.[1, 2] While compounds with metal-metal bonds had been synthesized previously, their bonding character was not understood or described correctly. In fact, the dirhenate complex was first reported in 1954, but it was not until a decade later that the quadruple Re-Re bond was elucidated through crystallographic studies and Molecular Orbital Theory justifications[3]. Up until that point, transition metal chemistry was focused on the concept of a metal center fully surrounded by other ligands, and the idea of a metal atom interacting with another metal atom was hotly debated. Following the recognition of the dirhenium quadruple bond, multiple bonds between metal atoms for elements were then soon discovered for elements such as technetium with the $[Tc_2Cl_8]^{3-}$ ion and molybdenum with the $Mo_2(O_2CCH_3)_4$ complex. Since that time, the area of metal-metal bonding has grown significantly. Thousands of such complexes have now been described spanning a much broader range of transition metal elements, and have been studied extensively by experimental, spectroscopic and computational methods.[3, 4]

The metal-metal bond is formed through the interactions of metal atom d-orbitals.[3] In considering the possible non-zero orbital overlaps between two metal atoms, there are only five ways in which these interactions can occur, and those are between the

corresponding pairs of d-orbitals. The combinations are as follows: a σ bond from the overlap of the $d_z^2$ orbitals, two π bonds from overlap of the two degenerate $d_{xz}$ and $d_{yz}$ orbitals, and a δ bond from overlap of two $d_{xy}$ orbitals. The antisymmetric combination of these orbitals results in the antibonding interactions between the metal atoms. It should be noted that, while the remaining pair of $d_x^2$-$_y^2$ orbitals can also form bonding or antibonding interactions, they have very little to do with metal-metal bonding as those orbitals are used primarily for ligand overlap. The energy of the orbitals are ordered based on the Hückel concept in that MO energies are proportional to their overlap integrals. The σ overlap is the largest, followed by π and then δ. The qualitative MO diagram and the resultant ordering of $\sigma < \pi < \delta < \delta^* < \pi^* < \sigma^*$ is shown in Figure I.1.

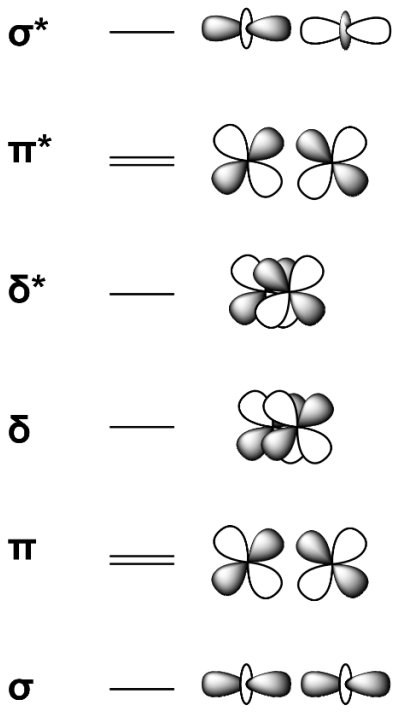


**Figure I.1** Qualitative molecular orbital diagram depicting generalized bonding between two metal atoms

*Metal-Metal Bonded Rhodium Complexes*

Perhaps one of the most highly investigated class of metal-metal bonded complexes are those featuring rhodium. Dirhodium complexes are of great interest due to their large variety of potential applications including catalysis for stereospecific C-C coupling reactions and other organic transformations, biomedical therapeutics, and photosensitization.[4-7] This diverse reactivity is due to the stable Rh(II)-Rh(II) bond and the highly tunable platform that is afforded by rational ligand design. The $Rh_2^{4+}$ core of these dirhodium (II,II) complexes is composed of a Rh-Rh bond with a bond order of one, and a bond length typically around 2.5 Å. As each $Rh^{II}$ atom has seven electrons, there is a total of 14 electrons populating the molecular orbitals formed by the metal overlap. The electronic structure is described as $\sigma^2\pi^4\delta^2\delta^{*2}\pi^{*\ 4}\sigma^{*0}$ and is shown in Figure I.2. However, it should be noted this structure is not representative of all classes of dirhodium complexes.[8] Specifically, the $\delta$ and $\delta^*$ molecular orbitals formed by the metal-metal interaction are of the correct symmetry to interact with $\pi$ and $\pi^*$ orbitals of the coordinating ligands. Oftentimes, destabilization of the $Rh_2(\delta^*)$ is observed, resulting in an electronic structure of $\sigma^2\pi^4\delta^2\pi^{*4}\delta^{*2}\sigma^{*0}$, and a qualitative depiction of this is shown in Figure I.3.

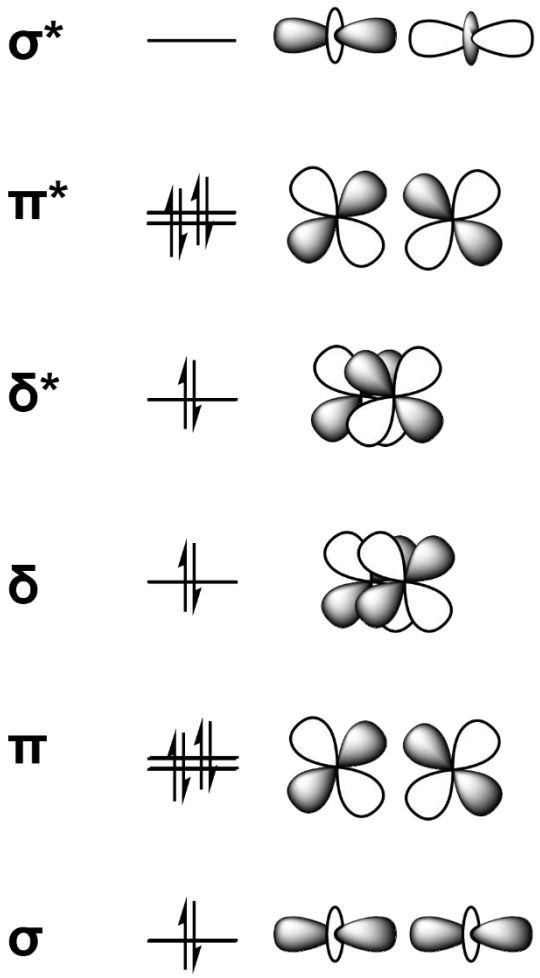


**Figure I.2** Qualitative molecular orbital diagram depicting generalized bonding between two rhodium atoms.

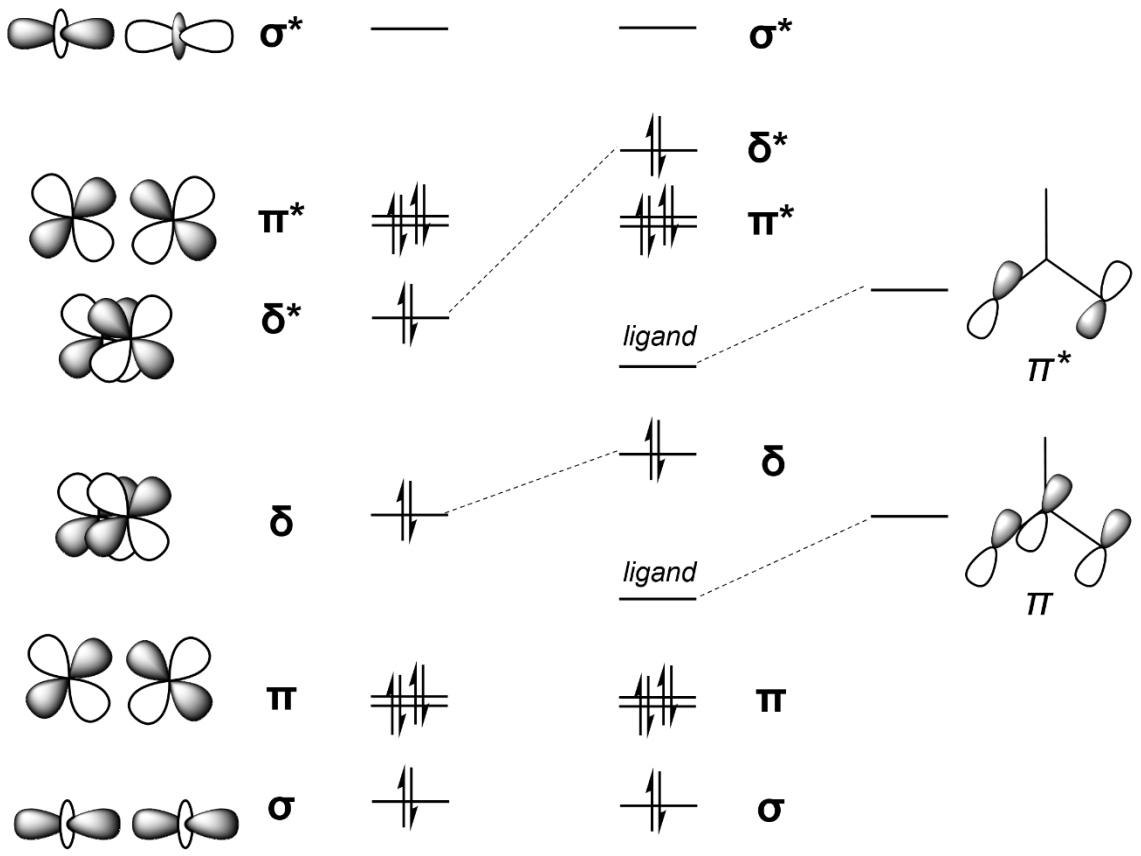


**Figure I.3** Schematic representation for the effect of formamdinate bridging ligands on the dirhodium molecular orbitals. .

The majority dirhodium complexes adopt a paddlewheel or partial paddlewheel geometry, in which the dirhodium core is supported by bidentate bridging ligands. The most widely studied class of dirhodium complexes are those with carboxylate bridges[9] as shown in Figure I.4. In addition, a large number of other compounds supported by bridging ligands such as thiocarboxylates, carboxamidates, 6-X-oxopyridinates and amidinates, among many others, which are shown in Figure I.5, have been synthesized and characterized (ref).

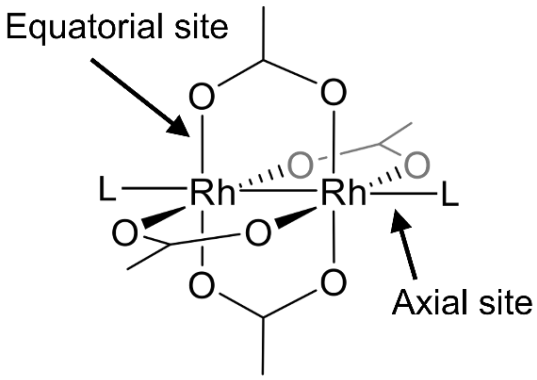


**Figure I.4** Structural representation of $Rh_2(O_2CCH_3)_4L_2$, with the axial and equatorial coordination sites labelled.

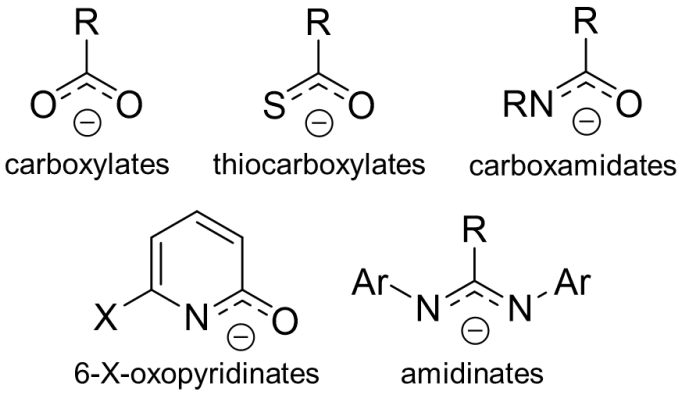


**Figure I.5** Examples of bridging ligands used in the synthesis of dirhodium (II,II) complexes.

The bridging ligands coordinate through the equatorial positions on the dirhodium core, of which there are a total of eight. Typically, ligands in the equatorial positions interact and influence the $Rh_2(\pi)$ and $Rh_2(\delta)$ type orbitals; tuning these ligands has the greatest effect on the structural and electronic properties of the complex. Paddlewheel complexes feature four bidentate bridging ligands in the equatorial positions.[3] The compounds described as partial paddlewheels, which are commonly studied in the Dunbar group, have two supporting bridging ligands and feature other bidentate chelating ligands or monodentate ligands in the remaining four equatorial positions. The axial ligands of a dirhodium complex interact primarily with the σ type orbitals and are typically quite labile which is important when considering the mechanism of various chemical transformations that are catalyzed by dirhodium complexes. The formation of adducts through the axial coordination sites has been extensively investigated especially for complexes of the type $Rh_2(O_2CR)_4L_2$ where L is an axially coordinating ligand. Axial ligands influence the energy of the σ* orbital, which is the LUMO for these complexes. As such, this is evidenced by the wide range of colors depending on the nature of the donor ligand at the axial site.[10]

Dirhodium complexes have been of interest to researchers for more than 60 years. The first dinuclear rhodium complex supported by carboxylate bridging groups was reportedly synthesized in 1960.[9, 11] In the early 1970's, tetracarboxylate complexes of this type gained recognition for their applications organic synthesis, were pioneered by Teyssie and co-workers[12]. These complexes were also recognized for their use as anti-tumor agents, a topic taht will be discussed in further detail in later sections. In the Dunbar group,

it has been of interest to use these complexes for applications in medicine, energy and catalysis. Within the scope of this dissertation, dirhodium complexes have been investigated as photosensitizers for biomedical therapeutics and for solar energy conversion through dye-sensitized solar cell applications.

## Metals in Medicine

### *Cancer*

Cancer is one of the leading causes of death in the United States (Figure I.6) and worldwide, according to the American Cancer Society and the World Health Organization.[13, 14] It is estimated that in 2021, 1.9 million new cases will be diagnosed, and more than 600 000 deaths will be attributed to cancer.[15]

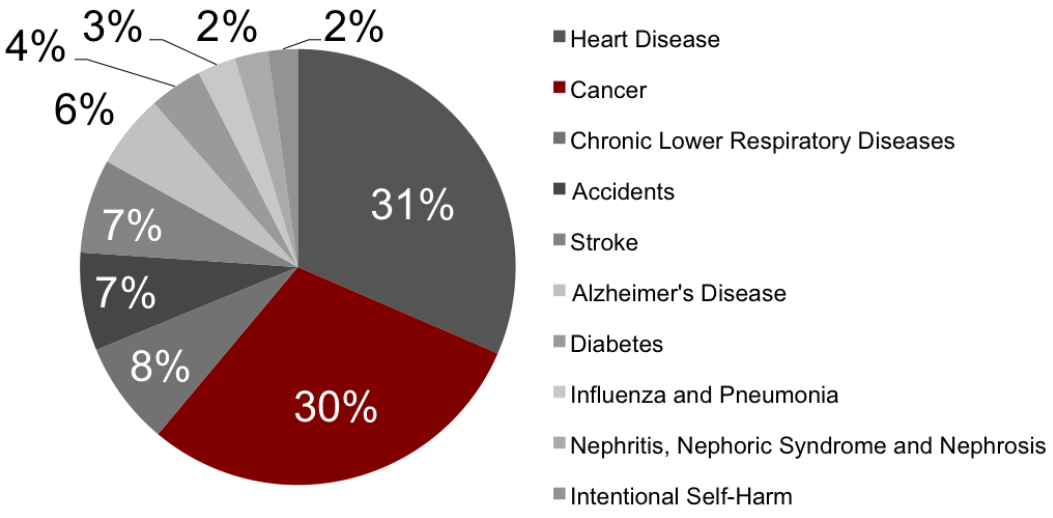


**Figure I.6** Leading causes of death in the United States in 2018.

Cancer is a collection of diseases characterized by abnormal, malignant cell growth.[16] There is a loss of control over cell replication and cell death, and there is the potential for these cells to spread to other parts of the body as well. A number of environmental facts such as tobacco, radiation, pollutants, infectious diseases, and diet are attributed to increasing the risk of developing cancer. However, approximately 5-10 cases are caused by innate factors such as inherited genes and mutations.[17] Cancer is treated and managed in several ways, including surgery, radiation, and chemotherapy. While the treatments used are dependent on a number of factors such as the type and location of the cancer and the patients' preferences, many of the methods currently adopted are aimed at removing or killing the cancer cells.[18] It is through this avenue that synthetic inorganic tools can be harnessed for developing new treatments against cancer.

*Cisplatin*

Metal compounds have long been used in the treatment of disease over the course of history.[19, 20] However, it was the discovery of cisplatin [*cis*-diamine dichloroplatinum(II)] *cis*-$[Pt(NH_3)_2Cl_2]$ as an anti-cancer agent marked the advent of modern medicinal inorganic chemistry[21, 22]. Cisplatin was first described in 1845 and the structure was deduced in 1893.[23] It was not until 1965, however, that a serendipitous discovery by Barnett Rosenburg and co-workers, who observed that bacterial binary fission was inhibited upon the electrolysis of platinum electrodes, led to the use of cisplatin to treat tumors and the drug was quickly approved by the FDA for testicular cancers.[21, 22]

In the cellular environment, the chloride concentration is much lower than in the extracellular space. When administered intravenously, cisplatin remains in the *cis*-

[$Pt(NH_3)_2Cl_2$] form due to the high chloride concentration of approximately 100 mM. Upon entering the cell where the chloride concentration is only approximately 4 mM, one of the chloride ligands is slowly displaced by a water molecule.[23] This aquation process yields the product *cis*-[$Pt(NH_3)_2(H_2O)Cl$], which is shown in Figure I.7. As a result, this complex can bind to DNA, because the water ligand can be easily displaced by *N*-heterocyclic bases. Binding is preferential to guanine bases, and, when the second chloride is displaced, crosslinking occurs. A crystal structure of this interaction was determined in 1995 by Lippard and coworkers. (Figure 1.8).[24, 25] When the DNA is in its crosslinked and kinked structure, replication can no longer occur, and so this triggers cell cycle arrest and programmed cell death.

Cisplatin is now one of the most widely used chemotherapeutic agents.[26] It is used to treat many types of cancers such as Hodgkin's lymphoma, ovarian cancer, advanced lung cancer, among others. The characterization of the biological fate of cisplatin and its mechanisms has inspired new generations of platinum complexes for anti-cancer applications, as well as the development of new classes of chemotherapeutic agents with other transition metals.

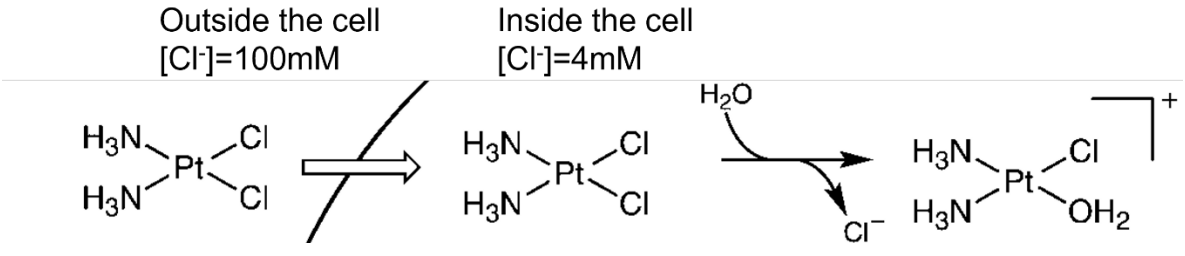


**Figure I.7** Schematic of the cisplatin aquation reaction

a)

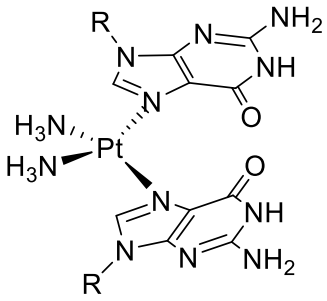


b)

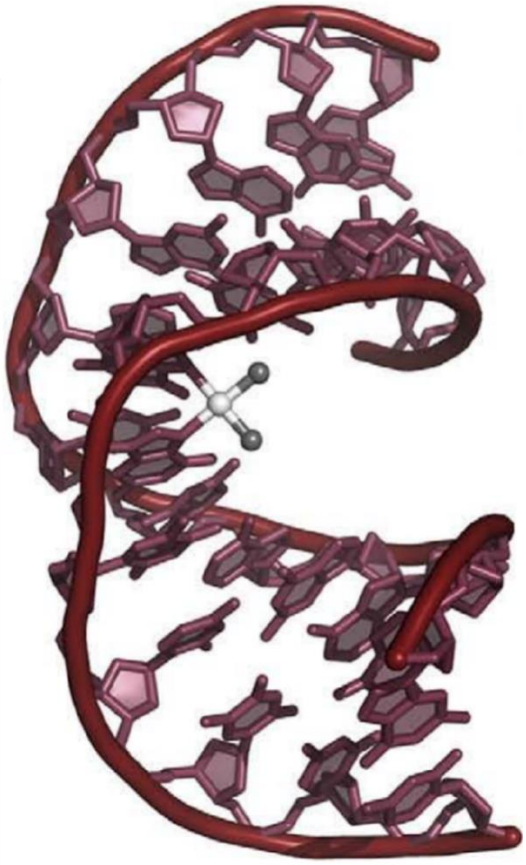

**Figure I.8** a) Representation of cisplatin binding to nucleotide bases and b) crystal structure showing the interaction of cisplatin with double stranded DNA (adapted from reference 24).

*Other Metal-Based Anti-Cancer Drugs*

After the FDA approval of cisplatin for use in the treatment of cancer, other series of platinum complexes have been designed and clinically tested (Figure I.9).[23] Two of the compounds, carboplatin and oxaliplatin are used worldwide, whereas nedaplatin, lobaplatin and heptaplatin are approved for use in certain countries. The development of these new molecules serves to address the issues of severe side effects that are caused by cisplatin. It should be noted that the mechanism of action for the new generation of platinum complexes is similar to that of cisplatin.

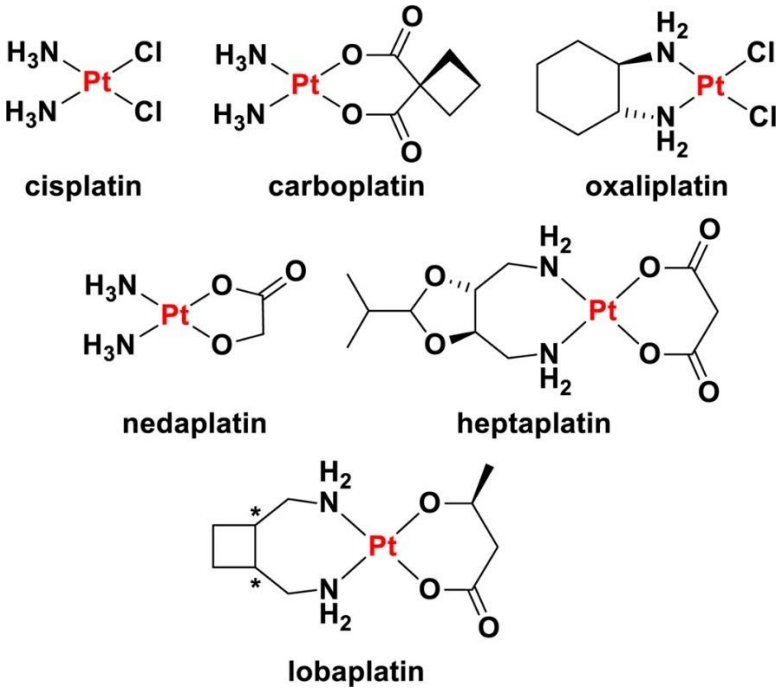


**Figure I.9** Structures of platinum-based drugs that are approved for cancer treatment and used commercially.

Carboplatin is known to have a more favorable toxicity profile than cisplatin, due to the presence of the bidentate dicarboxylate ligand instead of the two chloride ligands.

As such, the DNA binding kinetics and reactivity are altered due to the slower ligand dissociation process afforded by the bidentate ligand, which limits off-target toxicity.[27] The bidentate ligand is featured in the other platinum-based drugs as well. In the case of nedaplatin, for example, the glycolate ligand also serves to increase the water solubility of the molecule.[28] Current investigations in the development of new platinum anti-cancer agents continues to involve tuning the molecular framework to impart optimal biological properties.[23]

There is a crucial need to develop novel anti-cancer agents that can exhibit alternative mechanisms of action or bind to different cell targets and so numerous other metal complexes have also been investigated for anti-cancer properties.[20] Complexes that are currently being studied include those of titanium, gold, ruthenium and rhodium among many others, and several are currently undergoing clinical trials (Figure I.10).[29]

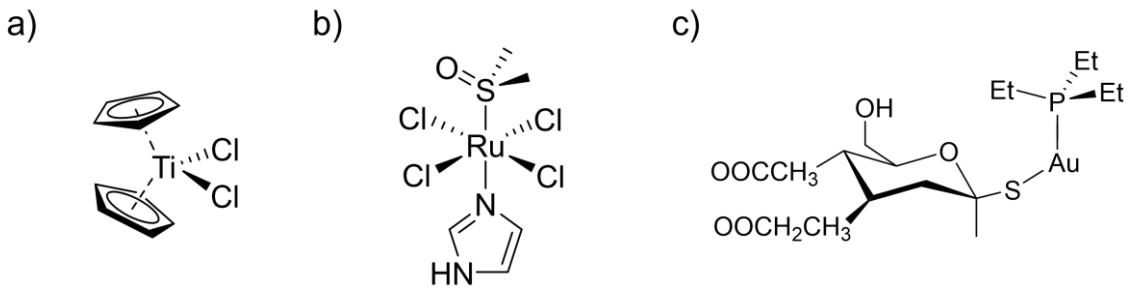


**Figure I.10** Schematic representations of examples of non-platinum based drugs a) titanocene dichloride b) NAMI-A c) Auranofin.

A few examples to highlight the breadth of this field include titanocene dichloride, ($Cp_2TiCl_2$), which is the first metallocene discovered to have anti-tumor activity.[30] This is a promising avenue of investigation as there was no evidence of nephrotoxicity, unlike with platinum-based compounds. A ruthenium complex of note is the anti-metastatic complex NAMI-A ([$H_2$im][*trans*-Ru(Him) (S-DMSO)$Cl_4$] where Him = imidazole and DMSO = dimethyl sulfoxide) which reached clinical trials.[31] Ruthenium complexes are also known to accumulate through iron transport mechanisms, which allows for new avenues of cellular uptake. In some cases, metal-based drugs that were FDA approved for other uses are currently under investigation for their anti-cancer properties as is in the case of the Au(I) complex Auranofin, which is sold under the brand name Ridaura and used to treat rheumatoid arthritis.[32]

Dirhodium (II,II) complexes have been known to function as anti-cancer agents since 1974 when dirhodium(II,II) tetracarboxylate compounds of the type $Rh_2(O_2CR)_4$ (R= Me, Et, Pr and Bu) were shown to exhibit anti-tumor activity against Erlich ascites in mice by Bear and coworkers.[33, 34] It was also observed that modification of the carboxylate bridge with increasing lipophilic substituents results in increased uptake of the complexes and improved tumor suppression activity.[35, 36] To understand the mechanisms by which dirhodium carboxylate complexes cause cell death, the Dunbar group studied the binding motif of these complexes with DNA by 1D and 2D NMR and MS experiments.[37-39] From these studies, it was found that dirhodium complexes undergo ligand exchange and bind to nucleotide bases of double-stranded DNA, not dissimilar to the mechanism of action of cisplatin (Figure I.11).[40] Molecular modeling of the pGpG dinucleotide showed that, while

there was a binding mode like that of cisplatin, the second rhodium atom afforded the complex the ability to also bind the ketone moiety on guanine. By reacting dirhodium complexes with analogues of adenine and guanine, it was determined that these bases form a variety of different products through binding to both the axial or equatorial positions, with examples shown in Figure I.12.

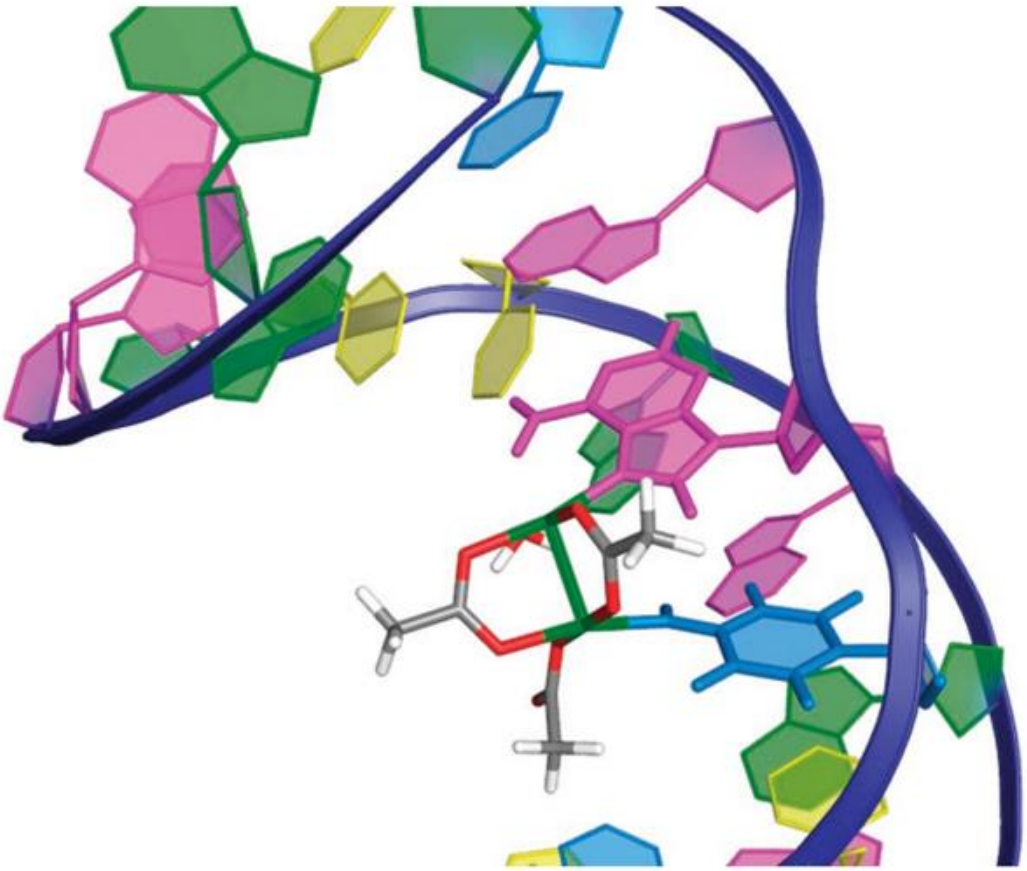

**Figure I.11** Representation of how *cis*-[$Rh_2(\mu\text{-}O_2CCH_3)_2(\eta^1\text{-}O_2CCH_3)]^+$ binds with the DNA dodecamer d(CTCTCAACTTCC)·d(GGAAGTTGAGAG). (Adapted from reference 40).

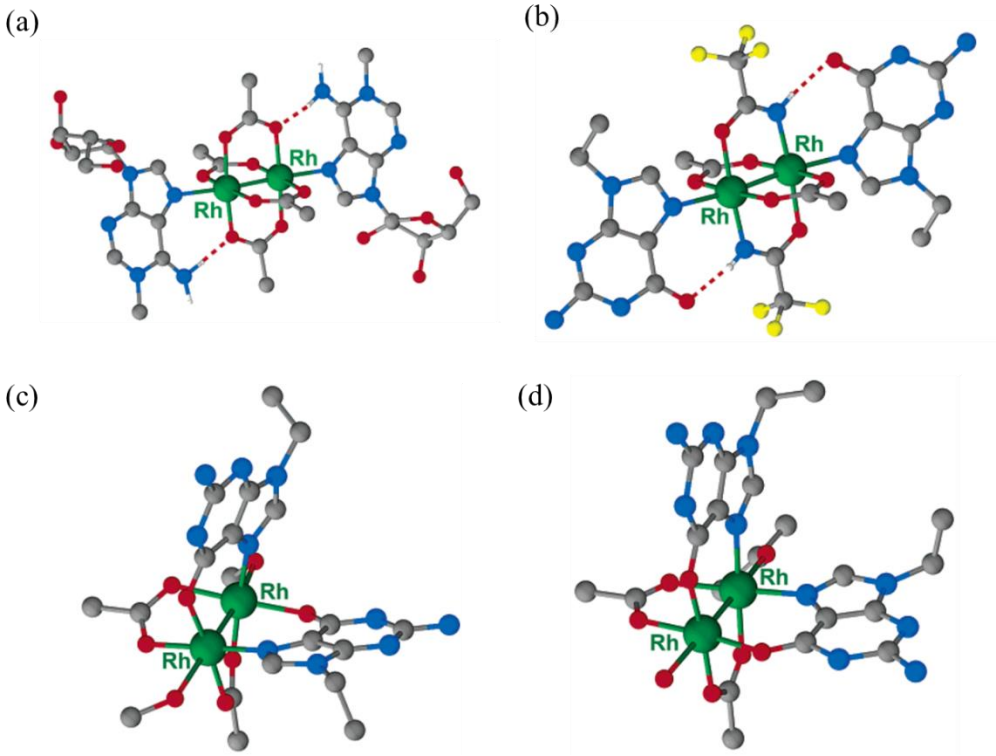


**Figure I.12** Examples of axial and equatorial binding of nucleotide analogues with dirhodium complexes and the resulting products a) $Rh_2(\mu\text{-}O_2CCH_3)_4(1\text{-MeAdo})_2$, b) *trans*-$[Rh_2(\mu\text{-}O_2CCH_3)_2(\mu\text{-}NHCOCF_3)_2(9\text{-EtGuaH})_2]$, c) H-T *cis*-$[Rh_2(\mu\text{-}O_2CCH_3)_2(9\text{-EtGua})_2(CH_3OH)_2]$, and (d) H-H *cis*-$[Rh_2(\mu\text{-}O_2CCH_3)_2(9\text{-EtGua})_2(Me_2CO)(H_2O)]^{2+}$ (Adapted from references 37-39).

Dirhodium complexes with other bridging ligands were also studied by the Dunbar group for their nucleotide base binding ability. For example, the compound *cis*-$[Rh_2(\mu\text{-DTolF})_2(\mu\text{-}O_2CCF_3)_2(H_2O)_2]$ (DTolF = *N*,*N*'-di-*p*-tolylformamidinate), forms H-H right-handed cross-links with the dinucleotides d(ApA), d(GpA), and d(ApG).[41, 42] This compound was, in fact, first investigated for its anti-cancer properties against Yoshida ascites and T8 sarcomas[43] before being studied by the Dunbar group. Dirhodium complexes consisting of alternative ligand binding motifs have also been extensively studied. The cytotoxicity of partial paddlewheel complexes bearing two bridging ligands

and two chelating diimine ligands of the type $[Rh_2(\mu\text{-}O_2CCH_3)_2(\eta^1\text{-}O_2CCH_3)(L)(CH_3OH)]^+$ (where L = bpy (2,2′-bipyridine) , phen (1,10-phenanthroline), dpq (dipyrido[3,2-*f*:2′,3′-*h*]quinoxaline), dppz (dipyrido[3,2-*a*:2′,3′-*c*]phenazine), dppn (benzo[*i*]dipyrido[3,2-*a*:2′,3′-*c*]phenazine), and dap (4,7-dihydrodibenzo[*de*,*gh*][1,10]phenanthroline) also were investigated.[44, 45] While the complex bearing the most highly conjugated dppn ligand interacts most strongly with DNA, $[Rh_2(\mu\text{-}O_2CCH_3)_2(\eta^1\text{-}O_2CCH_3)(dppz)(CH_3OH)]^+$ is the most cytotoxic, a fact that is attributed to differences in the lipophilicity of the complexes which affects cellular uptake. While tuning the ligands around the dirhodium core offers many opportunities to affect the interactions of the complex with various biomolecules and optimizes their anti-cancer properties, a drawback of these metal complexes and other chemotherapeutic agents previously described is their lack of selectivity for cancer cells versus healthy cells.

*Photodynamic Therapy*

Photodynamic therapy (PDT) is an alternative to traditional chemotherapeutic methods in which spatial and temporal control is afforded by the use of a photosensitizing drug which is only active upon irradiation with low energy visible light.[46-50] In terms of clinical use, the patient is administered a photochemotherapeutic drug which is distributed throughout the body. Light is then only introduced in the area where the cancer cells are localized. Because the photosensitizer exhibits cytotoxicity only upon irradiation, only the areas with the cancerous cells are targeted, thus sparing the healthy cells (Figure I.13)[46]

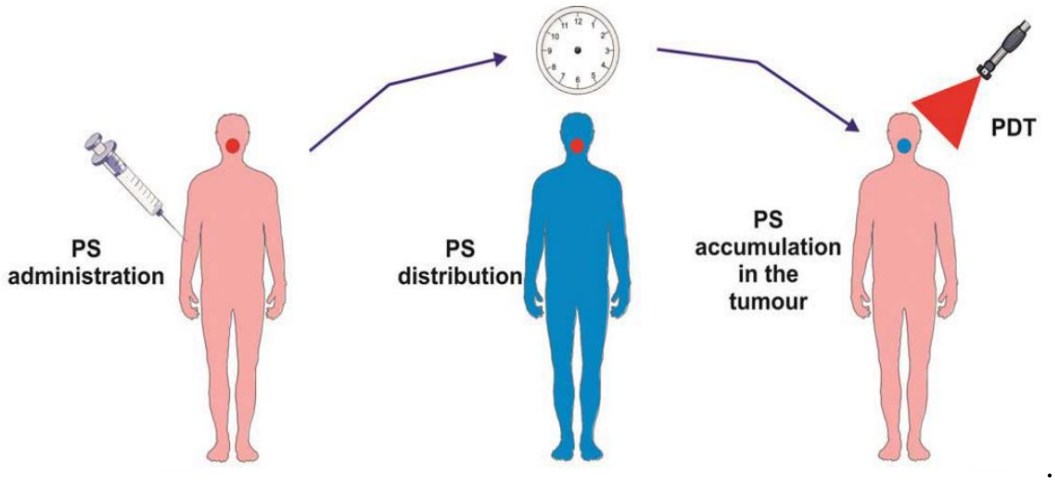


**Figure I.13** Depiction of PDT treatment.

Low energy visible light is required for PDT applications to facilitate deeper tissue penetration. The optimal range for irradiation is known as the "PDT window" and spans 500 nm to 900 nm.[51] As such, PDT is typically used to treat cancers that are on the surface of the body or accessible endoscopically. When light is shone on a photosensitizing compound, it can be excited from a singlet ground state ($^1$GS) to a singlet excited state ($^1$ES). From the $^1$ES, a triplet ground state ($^3$ES) can be populated via intersystem crossing (ISC), and it is from this state that the mechanisms resulting in cell death can occur (Figure I.14). Type I, or electron transfer processes can occur, by which radicals or other reaction oxygen species (ROS) are generated.[46, 52] These highly reactive species can oxidize biomolecules or other biological targets, resulting in cell damage and subsequent death. The type II, or energy transfer mechanism, involves the sensitization of singlet oxygen ($^1O_2$). Similar to other ROS pathways, $^1O_2$ is highly reactive and can cause significant damage to cells. In the case of photo-activated chemotherapy (PACT), irradiation of the

drug can result in the population of the excited triplet state which ultimately results in ligand dissociation.[52, 53] The ligand, the resulting compound or both may be bioactive, with respect to the initial prodrug. This approach does not require oxygen and the mechanisms for cell death do not need to include ROS.

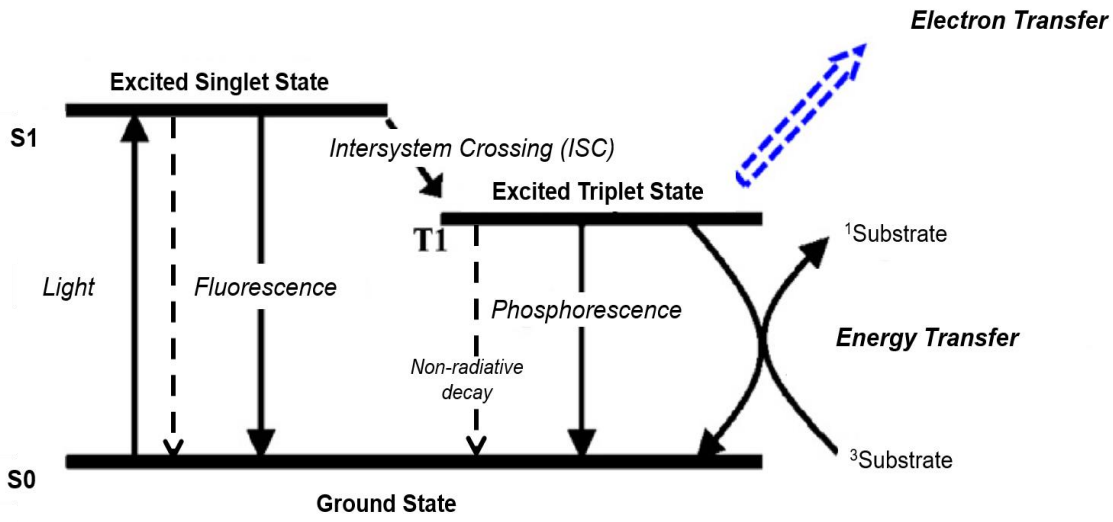


**Figure I.14** Generalized Jablonski diagram of a PDT photosensitizer.

The current FDA approved PDT drugs typically feature a porphyrin-based backbone or molecules that, when metabolized, form porphyrin type structures. The first approved PDT agent on the market is Photofrin© which is an oligomeric mixture of hematoporphyrin.[47, 48, 54] There are some drawbacks, however, including a weak absorption in the PDT window at its irradiation wavelength of 630 nm, a molar absorptivity of 3000 $M^{-1}cm^{-1}$, and a low quantum yield of $^1O_2$ (~15 %). Moreover, Photofrin© is known to have the undesirable side effect of causing extended photosensitivity in patients due to slow clearance from the body.[48] Newer generations of PDT drugs serve to address these drawbacks. More recently, 5-aminolevulinic acid (5-

ALA), trade name Levulan©, was FDA approved in 2017. The drug is a precursor to hemaoporphyrin, which is generated *in situ* after administration to the patient. Because Levulan© can be applied topically in its prodrug form, the side effects that patients experience from Photofrin© are mitigated.[55] To improve the $^1O_2$ quantum yield, metal ions that facilitate ISC due to the heavy atom effect and spin-orbit coupling can be incorporated into the design of new PDT platforms.[52]

*Photoactive Dirhodium Anti-Cancer Agents*

Dirhodium complexes, in addition to being explored as anti-cancer agents due to their DNA binding properties, have been investigated for their potential as photosensitizers for PDT applications. The photophysical and photochemical properties of $Rh_2(O_2CCH_3)_4L_2$, (L= alcohol, $PPh_3$, pyridine, THF and $H_2O$) were investigated by Turro and coworkers in 2001.[56] Long lived excited states ($\tau$ = 3.5-5.0 μs) were accessed by visible light irradiation. Furthermore, DNA photocleavage was observed upon irradiation in the presence of 3-cyano-1-methylpyridinium tetrafluoroborate ($py^+$) (Figure I.15).

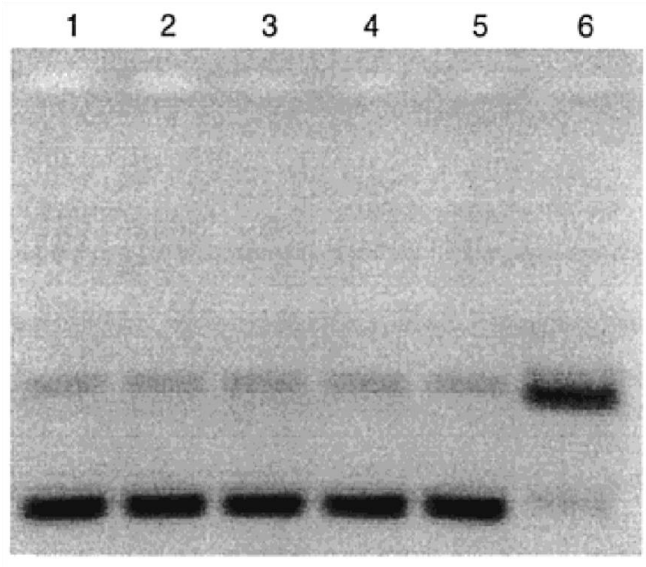


**Figure I.15** Ethidium bromide stained agarose gel of $Rh_2(O_2CCH_3)_4^{2+}$ with pUC18 plasmid DNA. Lane 1: pUC18, dark. Lane 2: pUC18, irradiated. Lane 3: pUC18, [$Rh_2$], irradiated. Lane 4: pUC18, $py^+$, irradiated. Lane 5: pUC18, [$Rh_2$], $py^+$, dark. Lane 6: pUC18, [$Rh_2$], $py^+$, irradiated. (Adapted from reference 54).

With respect to PACT, the light activated DNA binding properties were observed for the *cis*-$[Rh_2(\mu\text{-}O_2CCH_3)_2(CH_3CN)_6]^{2+}$ partial paddlewheel complex.[57] Upon irradiation with visible light ($\lambda > 455$ nm), a photoaquation reaction occurs, generating the *cis*-$[Rh_2(\mu\text{-}O_2CCH_3)_2(CH_3CN)_2(H_2O)_4]^{2+}$ species which binds to ds-DNA (Figure I.16). Selective toxicity upon irradiation was exhibited by this complex towards Hs-27 human skin cells. Upon irradiation with visible light for 30 minutes, a 34-fold decrease in the $LC_{50}$ was observed.[57] Recent work from the Dunbar group continued the investigation of these partially solvated complexes and includes the use of more electron donating ligands such as amidates and 2-oxypyridinates which serve to red-shift the absorption profiles into the PDT window. Compounds of the type *cis*-$[Rh_2(xhp)_2(CH_3CN)_n][BF_4]_2$ ($n$ = 5 or 6) were synthesized where xhp = 6-R-2-oxypyridine ligands, R = $-CH_3$ (mhp), −F (fhp), −Cl

(chp). The more electron rich bridging ligands exert a stronger *trans* effect on the labile equatorial $CH_3CN$ ligands, and, in the case of *cis*-$[Rh_2(chp)_2(CH_3CN)_6][BF_4]_2$, a 16.4-fold increase in cytotoxicity was observed when tested against HeLa cells.[58]

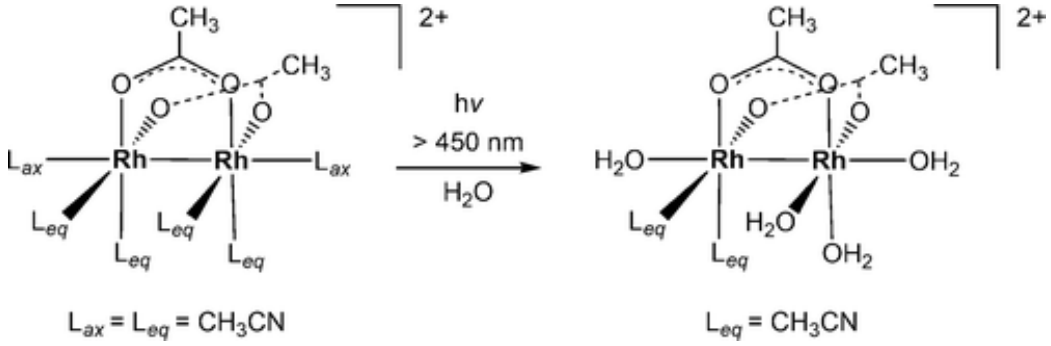


**Figure I.16** Schematic representation of the photoaquation process observed for *cis*-$[Rh_2(\mu\text{-}O_2CCH_3)_2(CH_3CN)_6]^{2+}$.

Another avenue that has been pursued in the design and optimization of dirhodium complexes for PDT applications has been the use of chelating diimine ligands, the increased conjugation of which servse to red-shift the absorption of the complexes into the PDT window. The diimine ligands used in the Dunbar group are shown in Figure 1.17 and include bpy (2,2′-bipyridine) , phen (1,10-phenanthroline), dpq (dipyrido[3,2-*f*:2′,3′-*h*]quinoxaline), dppz (dipyrido[3,2-*a*:2′,3′-*c*]phenazine), and dppn (benzo[*i*]dipyrido[3,2-*a*:2′,3′-*c*]phenazine).

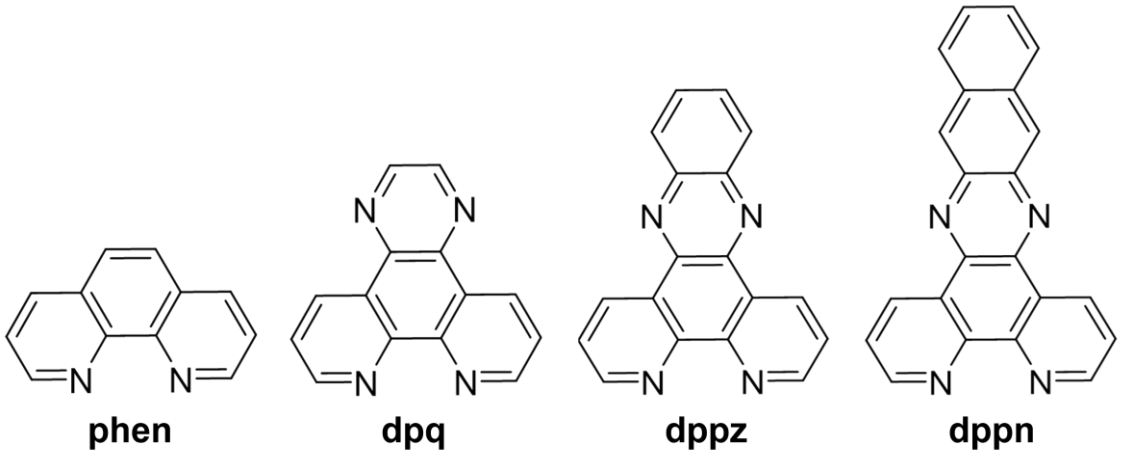


**Figure I.17** Chemical structures of various diimine ligands.

A series of carboxylate bridged dirhodium partial paddlewheel complexes of the type *cis*-$[Rh_2(O_2CCH_3)_2(NN)_2]^{2+}$ where NN = diimine ligand were synthesized.[59] The complex *cis*-$[Rh_2(O_2CCH_3)_2(dppz)_2]^{2+}$ was found to be capable of cleaving plasmid DNA in the absence of $O_2$, and to exhibit a 3.4-fold increase in cytotoxicity against Hs-27 human skin cells upon irradiation ($\lambda_{irr}$ = 400-700 nm, 30 min). The complex *cis*-$[Rh_2(O_2CCH_3)_2(dppn)_2]^{2+}$ displays a substantial increase in cytotoxicity against Hs-27 cells when irradiated, specifically a 24-fold increase was observed. This complex is able to generate $^1O_2$ due to having an accessible dppn-based $^3\pi\pi^*$ excited state, which is an important design consideration for analogous dirhodium PDT photosensitizers. The ability to tune the ligand field and influence the photophysical and photochemical properties of these complexes is of great importance for other applications as well.

**Solar Energy**

A heavy reliance on fossil fuels and other non-renewable resources has placed an enormous strain on the ability to uphold the current standard of living in a way that is clean and sustainable.[60] As energy demands are projected to continue increasing, it is of paramount importance to develop technologies and alternatives to fossil fuels. Currently, renewable sources constitute approximately 11% of the energy that is consumed in the United States (Figure 1.18). Within that amount, biomass sources make up 45%, followed by hydroelectric (25%), wind (21%), solar (6%) and geothermal (2%).[61] However, it has been calculated that the incoming solar radiation absorbed by the atmosphere, land and oceans of the Earth per year totals almost 4 million exajoules and, in one hour, this would be enough to power the world for a year.[62] Solar energy is considered to be the cleanest and most abundant renewable energy source, therefore methods by which this energy can be harnessed more efficiently is a very attractive area of research.

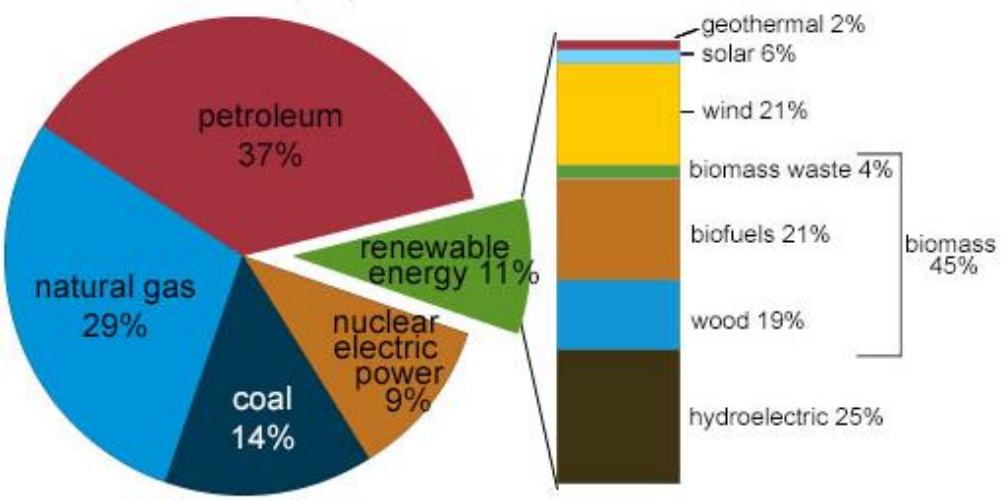


**Figure I.18** US energy consumption by energy sources

**Traditional Solar Cells**

Photovoltaic (PV) cells, or solar cells, are the primary means of converting sunlight to electricity.[63] The oldest solar cell arrays date back to the late 1800's, and were based on selenium with an efficiency of ~1%.[64] It was not until the mid-late 1900's that the development of solar cell technology began to accelerate due to energy demands. Currently, traditional residential and commercial solar cells have efficiencies between 15-20%.[63] Currently, the highest experimentally measured solar conversion efficiency for a solar cell is 46.0%, which is composed of a multijunction GaInP/GaAs; GaInAsP/GaInA cell in a concentrator photovoltaic system.[65]

Traditional silicon based solar cells function on the basis of the photovoltaic effect.[63, 66] Two silicon based semiconductor layers are stacked and encased in a translucent-anti reflective material.n electron deficient p-type layer is stacked above an electron rich n-type layer. At the interface of the two layers, known as the p-n junction, local charges build up from each layer and absorption of photons by the n-type layer induces a directional flow of electrons toward the anode. Simultaneously, absorption of photons from sunlight by the p-type layer induces a hole migration across the p-n junction in the opposite direction (Figure I.19).[66]

*Dye Sensitized Solar Cells*

Dye-sensitized solar cells (DSSC), otherwise known as Grätzel cells as they were first developed by Grätzel and co-workers in 1988,[67-70] are considered to be a part of the third generation of PV cells and overcome some of the drawbacks that are encountered with traditional silicon single junction solar cells. They offer a good price-to-performance

ratio and are flexible and durable.[70] Furthermore, DSSCs can work even in low-light conditions, or under incident light angles at which traditional solar cells would fail to work. A DSSC is composed of a transparent conducting layer on which there is a semiconducting layer with an anchored dye photosensitizer, a counter electrode, and a binary redox couple for regenerating the photosensitizer. Upon photoexcitation of the dye, an electron or hole can be injected into the semiconductor material (Figure I.20). [71]

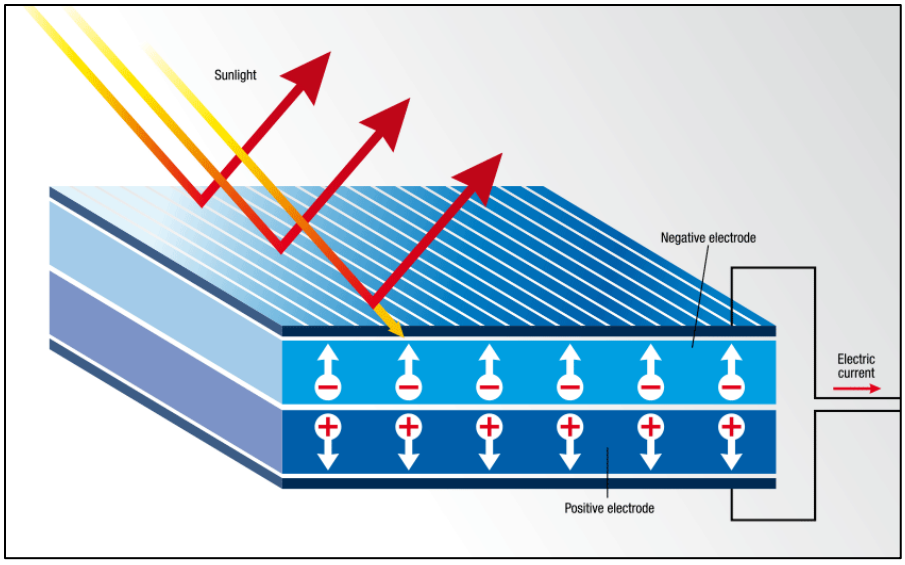


**Figure I.19** Schematic of a single junction silicon based solar cell.

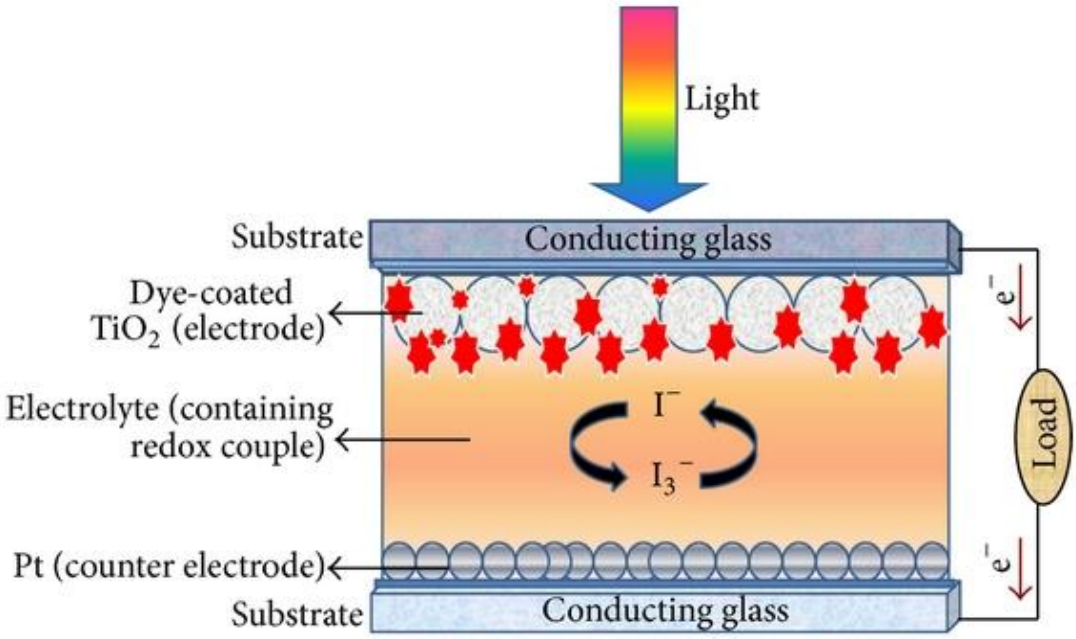


**Figure I.20** Schematic of a DSSC (Adapted from reference 69).

Numerous considerations must be taken into account when designing a DSSC, and various avenues of investigation are currently pursued for each component of the cell.[70, 72, 73] The theoretical efficiency limit of these devices can be calculated and it is 33 % for n-type sensitized DSSCs and 44 % in the case of n- and p-type tandem cells, but that has not yet been achieved.[74] The transparent conducting substrate is often made up of FTO (fluorine-doped tin oxide) or ITO (indium tin oxide). The semiconductor layer can be composed of various materials such as $TiO_2$ or NiO. Much research has been conducted and is ongoing to optimize the performance of the DSSC through tuning the porosity and particle size of the semiconductor material.[75, 76] The design of the sensitizing dye is an extremely important consideration in the development of DSSCs and for enhancing their efficiencies. Sensitizers should be chemically and thermally stabile, absorb strongly in the visible and near-IR region, possess HOMO/LUMO energy levels that allow charge transfer to occur from the excited state of the compound to the semiconductor, and be functionalized with anchoring groups such as carboxylates such that the dye can adsorb onto the surface of the semiconductor material.[70] To date, both organic and inorganic dyes have been thoroughly investigated. Organic compounds designed around a D-π-A structure are of particular interest.[77-79] Photoinduced charge separation occurs when irradiation shifts electron density from the donor moiety (D) through the π-conjugated linker to the acceptor moiety (A). Porphyrin derivatives and perylene type molecules are also of great interest for their use as photosensitizers.[80]

*Metal Based DSSC Sensitizers*

Among the inorganic compounds, of which there are complexes containing metals such as rhenium, iron, and copper among others, complexes with a Ru(II) center are considered the gold standard for DSSC dyes and are the most widely studied.[81] Examples of various ruthenium sensitizers are shown below in Figure I.21.

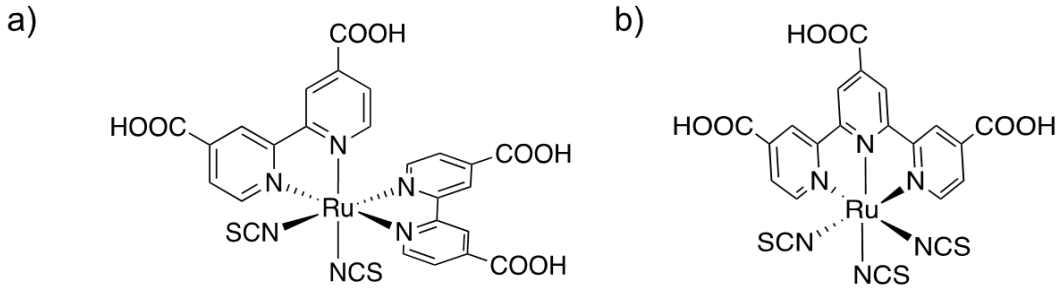


**Figure I.21** Chemical structures of benchmark ruthenium dyes for DSSC applications a) N3 b) N749.

The N3 "red dye" $[Ru(dcbpyH_2)_2(NCS)_2]$ was reported in 1993 with a power conversion efficiency (PCE) of 10%. The N749 dye $[Ru(4,4',4''\text{-}(COOH)_3\text{-terpy})(NCS)_3]$, known as "black dye" due to its visual appearance, is also of note.[68, 70, 82] The ruthenium is supported by a terpyridine functionalized by carboxylate anchoring groups. N479 has a reported PCE of 10.4%. Other polypyridyl ruthenium complexes have since been developed, although none exceed PCE values of ~11%.[72, 81] This situation may be due to the absorption profile of most ruthenium complexes, which do not absorb strongly beyond ~600 nm, and thus cannot harness the full potential of the visible solar spectrum. It is therefore an avenue of interest and investigation in this field to develop other metal-based

photosensitizers which can overcome the obstacles presented by these ruthenium complexes.

**Dissertation Objectives and Outline**

Dirhodium complexes are highly tunable and functionalized scaffolds with promising photophysical properties for a wide variety of applications in medicine and energy. Careful design of the ligand field environment around the dirhodium core yields desired properties for their respective applications. In order to achieve these goals, it is important to understand the fundamental structural and electronic properties of these complexes so that they can be optimized in the future. Additionally, the coordination modes of ligands around the dirhodium core opens unique possibilities for exploring new and interesting geometries and platforms for these complexes.

In Chapter II, the synthesis and characterization of a new class of dirhodium complexes featuring a mixed bridging ligand motif is discussed in the context of PDT. The compound with this new motif iss successful in inducing photocytoxicity, and the biological activity of this complex is contrasted with the non-mixed bridged analogues.

In Chapter III, a systematic investigation was undertaken to determine the effect of halogen substituents on the formamidinate bridging ligands of partially solvated dirhodium complexes. Experimental and theoretical studies of the structural and electronic properties as well as ligand dissociation kinetics are presented.

Chapter IV describes the development and adaptation of axially blocked dirhodium complexes with panchromic absorption for DSSC applications. Two series of complexes

were synthesized and characterized for n-type and p-type sensitization. The potential of these complexes as dyes is assessed in this chapter.

Conclusions and future directions for dirhodium photosensitizers within the scope of PDT agents and DSSC dyes is discussed in Chapter V.

# CHAPTER II

# INVESTIGATION OF MIXED BRIDGING LIGAND DIRHODIUM (II,II) COMPLEXES AS A NEW SCAFFOLD FOR PHOTODYNAMIC THERAPY

## Introduction

Cancer continues to be a leading cause of death worldwide and it is of paramount importance that research efforts target new treatment strategies with high efficacy and selectivity.[13, 15] Dirhodium(II,II) complexes have long been investigated as metallodrugs for anticancer applications, in part due to their ease of ligand functionalization and high stability. Variations to the coordination sphere of the complex result in tunability including control over their excited state properties,[83, 84] which renders them excellent candidates as photosensitizers for photodynamic therapy (PDT), a non-invasive technique that affords spatial and temporal control over cancer treatment.[46] In typical PDT therapy, irradiation with low-energy visible light results in the population of a long-lived triplet excited state able to undergo energy transfer to generate $^1O_2$ from $^3O_2$, leading to a cytotoxic tissue response.[46, 47, 52]

Examples of dirhodium complexes that have been investigated for their anticancer properties include dirhodium(II,II) tetracarboxylate compounds of the type $Rh_2(O_2CR)_4L_2$ (R= Me, Et, Pr and Bu; L= axial solvent) that were shown to exhibit antitumor activity against Erlich ascites in mice.[33-36] Investigations into the nature of the antiproliferative activity by the Dunbar group led to the finding that dirhodium complexes bind to ds-DNA, as evidenced by NMR spectroscopy and mass spectrometry.[37-39, 85] In 2001, the

photophysical and photochemical properties of $Rh_2(O_2CCH_3)_4$ were studied by the Turro group who reported a long-lived excited state and DNA photocleavage upon irradiation in the presence of an electron acceptor.[57] Dirhodium(II,II) complexes with chelating diimine ligands have since been prepared in the Turro and Dunbar groups and found to exhibit DNA photocleavage and cellular cytotoxicity against various cancer cell lines upon irradiation.[44, 45, 86, 87] The use of more electron donating bridging ligands has also been an avenue of exploration due to their lower energy absorption profiles compared to acetate bridged analogues. These examples include dirhodium compounds with nitrogen donor bridges, such as *cis*-$[Rh_2(HNOCCH_3)_2(CH_3CN)_6]^{2+}$, which undergo photoinduced DNA binding following acetonitrile photodissociation.[88] In addition, upon substitution of two acetonitrile molecules with the diimine ligand dppn (benzo[i]dipyrido[3,2-a:2',3'-c]phenazine), $^1O_2$ was sensitized with a quantum yield, Φ, of 0.22.[89] It should also be noted that the mixed bridge dirhodium compound $[Rh_2(DTolF)_2(O_2CCF_3)_2(H_2O)_2]$ (DTolF = p-tolyl formamidinate), first reported by Piraino and coworkers, exhibits anticancer activity similar to that of cisplatin and $[Rh_2(O_2CCH_3)_4]$ with increased survival rates in mice bearing Yoshida ascites and T8 sarcoma.[43]

The mixed ligand scaffold in combination with electron accepting chelating diimine ligands remains an under-explored topic in the design and synthesis of potential dirhodium PDT agents. A dirhodium paddlewheel complex with two different types of bridging ligands in a ratio of 1:3 is presented and discussed in detail.

The new compound $Rh_2(F_2Form)(O_2CCH_3)_3$ (**1**) was prepared and subsequently used as a building block to synthesize the partial paddlewheel compound

$[Rh(F_2Form)(OAc)(dppn)_2]^{2+}$ (**2**) which features a mixed bridging ligand motif that consists of one acetate and one formamidinate ligand in combination with two chelating diimine dppn ligands (Figure II.1). The photophysical properties of **2** were investigated along with its cytotoxicity against HeLa cells.

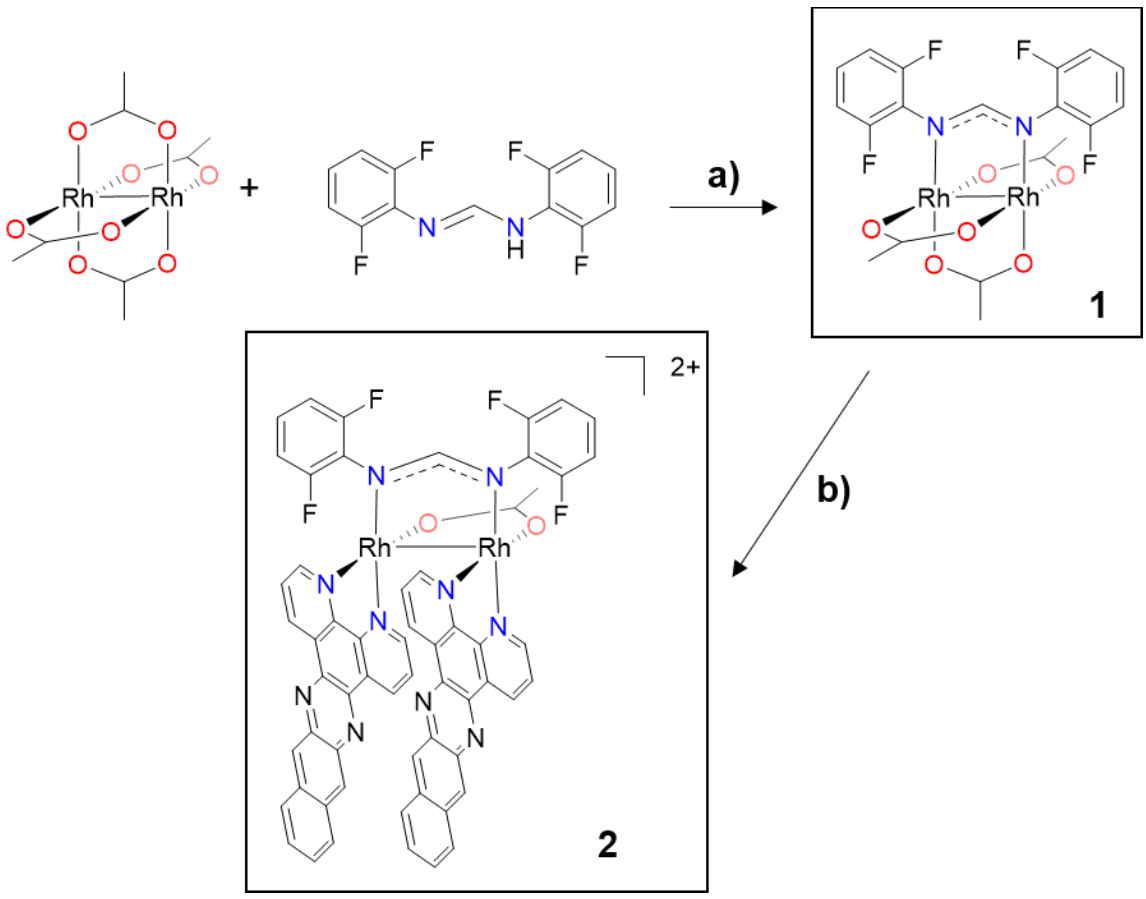


**Figure II.1** (a) dirhodium tetraacetate and deprotonated F2-Form with KOtBu in dry THF/MeCN (50% v/v) at room temperature for 24 h to yield **1** and (b) $Rh_2(F_2Form)(O_2CCH_3)_3$ refluxed with 2 eq. of dppn in dry $CH_3CN$ to yield **2**.

## Experimental

*Materials.*

The $Rh_2(\mu\text{-}O_2CCH_3)_4$ precursor was purchased from Pressure Chemicals and used without further purification. The compound *N,N'*-bis(2,6-difluorophenyl)formamidine (*o*-$HF_2$form) was synthesized by a slightly modified published procedure[90] from 2,6-difluoroaniline and triethyl orthoformate purchased from TCI which were used without further purification. Potassium tertbutoxide ($KO^tBu$) was used as purchased from TCI. The ligand benzo[i]dipyrido[3,2-a:2',3'-h]phenazine (dppn) was prepared according to published procedures.[91] Analytical thin layer chromatography was carried out on glass-backed sheets coated with neutral aluminum oxide F254 adsorbent (Sorbtech). Flash chromatography was performed with aluminum oxide, neutral, Brockmann I, for chromatography, 50-200 μm, 60A, purchased from ACROS Organics. Toluene and diethyl ether were of ACS grade and used as received, ACS grade tetrahydrofuran was stored over 3Å molecular sieves, and ACS grade acetonitrile was dried over 3Å molecular sieves and distilled under a $N_2$ atmosphere. Standard Schlenk-line and glove box techniques under a $N_2$ atmosphere were used during synthesis, while work-up and isolation of products was performed in air unless otherwise stated.

Cell culture reagents included Dulbecco's modified Eagle medium (Invitrogen), fetal bovine serum (Atlanta Biologicals), Leibovitz's L-15 Medium without phenol red (Life Technologies), Phosphate-Buffered Saline solution (Life Technologies), and Resazurin (Sigma). The Annexin V-FITC and propidium iodide apoptosis assays

(ThermoFisher) and MitoProbe® JC-1 assay (Life Technologies) were used according to the manufacturer's protocol. The HeLa cell line was obtained from the American Type Culture Collection (cell line CCL-2)

**$Rh_2$($\mu$-o-$F_2$form)($\mu$-$O_2CCH_3$)$_3$•2$O_2CCH_3$ (1):** Quantities of o-$HF_2$form (72 mg, 0.26 mmol) and KO$^t$Bu (28 mg, 0.25 mmol) were dissolved in 20 mL of THF and the reaction mixture was stirred at room temperature for 4 h. The resulting tan solution was added dropwise to a solution of $Rh_2(\mu\text{-}O_2CCH_3)_4$ (123 mg, 0.24 mmol) in 20 mL of dry acetonitrile The reaction mixture was stirred for 24 h at room temperature. The resulting maroon solution was filtered through Celite® and the solvent was removed under reduced pressure to give a maroon solid which was purified by flash chromatography ($Al_2O_3$, toluene/acetonitrile 0-40% gradient elution). Yield 67 mg (36 % yield) of a dark purple powder. X-ray quality crystals were obtained by slow diffusion of diethyl ether into a concentration solution of the compound in acetonitrile. $^1$H-NMR (500 MHz, $CD_3CN$-d3), δ(ppm): 1.74 (s, 6H, $CH_3$), 1.85 (s, 3H, $CH_3$), 7.00 (m, 4H, Ar H), 7.21 (m, 2H, Ar H). Anal. Calcd. For $C_{21}H_{21}F_4N_3O_7Rh_2$: 35.56, N 5.92, H 2.98 %. Found C 35.31, N 6.00, H 3.12%.

**[$Rh_2$($\mu$-o-$F_2$form)($\mu$-$O_2CCH_3$)(dppn)$_2$]($O_2CCH_3$)$_2$ (2):** A Schlenk flask was charged with dppn (97.5 mg, 0.29 mmol) and **1** (100.6 mg, 0.15 mmol) and 20 mL of dry acetonitrile and the reaction mixture was refluxed for one week to give a dark brown solution. Upon cooling to room temperature, the solution was concentrated by evaporation under reduced pressure and the product was precipitated with diethyl ether. The brown

product was collected by filtration on a fine frit and washed with copious amounts of diethyl ether to obtain the acetate salt. Yield: 154.2 mg (82 % yield).

*Instrumentation and Methods.*

$^{1}$H NMR spectra were collected on an Inova 500 MHz spectrometer; the chemical shifts are reported in ppm. The residual peak of the residual $CD_3CN$-$d_3$ deuterated solvent signal at 1.94 ppm[92] was used as the reference for the chemical shifts. Electrospray ionization mass spectra (ESI-MS) was performed by the Laboratory for Biological Mass Spectrometry at Texas A&M University using a PE Sciex (Concord, Ontario, Canada) API Qstar Pulsar with an Ionwerks time-to-digital converter, TDCx4, for data recording. Elemental analyses were performed at Atlantic Microlabs Inc. Electronic spectroscopy measurements were performed on a Shimadzu UV-1601PC spectrophotometer using 1 x 1 cm quartz cuvettes, and absorption spectra was obtained in triplicate.

Single crystals of **1** were selected under ambient conditions from oil using a MiTeGen microloop. The X-ray data set was collected on a Bruker CCD APEX diffractometer with graphite monochromated Mo Kα radiation (λ = 0.71073 Å). Single crystals of **2** were selected under ambient conditions from oil using a glass capillary. The data set was collected at the Advanced Photon Source at Argonne National Laboratory with synchrotron radiation (λ = 0.41328 Å), on beamline 15-ID-B. For compound **1,** the initial unit cell was determined using SAINT from a set of three ω-scans consisting of 0.5° frames and a sweep width of 15°. APEX2 was used to determine the data collection to collect all independent reflections to a resolution of at least 0.82 Å. Full details of the data

collection and refinement parameters are presented in Table II.1. The data were corrected for absorption using SADABS[93] and the space group was determined from analysis of the systematic absences and E-statistics using XPREP. The structures were solved using the intrinsic phasing routine in SHELXT or by direct methods implemented in SHELXS. The non-hydrogen atoms were located from Fourier difference maps by least-squares refinement of the structure using SHELXL-2014.[94] All non-hydrogen atoms were refined anisotropically and hydrogen atoms were placed in calculated positions and refined with thermal parameters constrained to their parent atoms. DIAMOND was used to generate the molecular graphics.

Density Functional Theory (DFT) calculations for molecular and electronic structures were performed using the Gaussian (16) program package.[95] The MPW1PW91[96-98] correlation and exchange functional was used with the Stuttgart RSC 1997 Electron Core Potential (ECP)[99] basis set for the Rh atoms and the 6-31G†[100] basis set for the C, N, O, F, H atoms. The starting points for the gas-phase optimizations were taken from the crystal structure of the complexes, excluding the counterions and solvent molecules. Time-Dependent Density Functional Theory (TD-DFT) calculations were performed using the polarized continuum model (PCM)[101] with acetonitrile as the solvent. From the optimized singlet ground state geometry, the first sixty lowest singlet-to-singlet excited states were calculated. The graphic software 'Gaussview' was used to plot the molecular orbitals with iso-values of 0.03. The Chemissian Visualization Computer Program was used to analyze molecular orbital contributions.[102]

Singlet oxygen quantum yields were performed using $[Ru(bpy)_3]^{2+}$ as a standard ($\Phi_\Delta$ = 0.81 in MeOH), 1,3-diphenylisobenzofuran (DPBF) as a $^1O_2$ trapping agent, and following a previously established procedure.[103] Femtosecond transient absorption spectroscopy was performed using a modified instrument whose details were previously reported.[104] Briefly, the fundamental 800 nm from a Ti:Sapph Astrella laser system (Coherent) was 8 mJ. Part of this output (3 mJ) was used to pump an OPA (OPerA Solo) which was used to generate all excitation wavelengths. White light continuum was generated using $CaF_2$ on a rotating mount. The samples were excited at 2.0 to 2.5 μJ at the sample. The instrument response function was determined to be 85 fs via the optical Kerr effect in cyclohexane. All samples were flowed in a 1 mm path-length flow cell (Harrick Scientific) equipped with 1 mm $CaF_2$ plates. The polarization angle between the pump and probe pulses was set to the magic angle to account for the effects of rotational diffusion. Multiple retroreflector cycles were taken, and all samples were measured via steady-state UV-Vis before and after to ensure no sample decomposition occurred.

Nanosecond transient absorption spectroscopy was performed on a previously reported instrument.[104] For these experiments, the second (532 nm) or third harmonic (355 nm) of a Nd:YAG laser (Quanta-Ray INDI, Spectra-Physics) were used as the pump pulse and the output of a continuous 150 W xenon arc lamp gated with a Uniblitz shutter was used as the probe. The excitation and probe pulses were overlapped at a 90° geometry at the sample. Sample concentrations were adjusted such that they absorbed ~ 0.5 at the excitation wavelength in a 1 × 1 quartz cuvette.

The DNA interactions upon irradiation and in the dark were investigated using gel electrophoresis mobility assays. In the dark, compound **2** was dissolved in Milli-Q and diluted to working concentrations of 1, 10 and 100 μM. The compounds were added to solutions of 15mg/mL pUC18 plasmid in 10mM phosphate (pH =7.5), in two groups. The "light" group was irradiated with a 300W xenon arc lamp for 1 h, after which time they were incubated at 37ºC for 24h in the dark, while the other group was kept in the dark and incubated at 37ºC for 24 h. The mobility shift assays were performed with 1% agarose gels with ethidium bromide staining, in 1× TAE buffer (40 mM Tris-acetate, 1 mM EDTA) at 100 V.

The photocytotoxicity of **2** was determined by the resazurin cell viability assay. Monolayers of HeLa cells were cultured in DMEM containing 10% FBS, 50 μg/mL of gentamicin, 4.5 mg/mL of glucose, and 4 mM of L-glutamine. The cells were incubated in a humidified atmosphere containing 5% $CO_2$ at 37ºC and allowed to grow to approximately 70% confluency. For cell viability studies, the cells were seeded into 96-well plates, which were incubated for 8 hours. Compound **2** was dissolved in PBS with 4% v/v DMSO, diluted to working concentrations, and added to the plates at this time. After incubating for 16 hours at 37 ºC in a 5% $CO_2$ atmosphere, the media in each well was replaced with L15 media (containing 10% FBS and 1% penicillin/streptomycin). Plates were then either kept in the dark at 37ºC or irradiated in a UV/vis photoreactor LZC-14 (LuzChem Research, Inc.) equipped with 14 lamps ($\lambda_{irr}$>400 nm) for 1 hour. The cells were then incubated for 24 hours at 37 ºC in a 5% $CO_2$ atmosphere, after which time the resazurin cell viability assay was performed by adding 10μL of 0.6 mM resazurin in

PBS to each well followed by 2 hours of incubation. The fluorescence signal was measured using a Promega Glomax Multi microplate reader. Each experiment was performed in triplicate.

To determine mitochondrial depolarization, the JC-1 assay was performed. Following the procedure for the cell viability assays, HeLa cells were seeded at 70% confluency and were incubated for 8 hours. Compound 2 was dissolved in PBS with 4% v/v DMSO, diluted to working concentrations and added to the plates. Following 16 hours of incubation at 37 ºC in a 5% $CO_2$ atmosphere, the media in each well was replaced with L15 media (containing 10% FBS and 1% penicillin/streptomycin). Plates were either kept in the dark at 37ºC or irradiated in a UV/vis photoreactor LZC-14 (LuzChem Research, Inc.) equipped with 14 lamps ($\lambda_{irr}$>400 nm) for 1 hour. The cells were then incubated for 24 hours at 37 ºC in a 5% $CO_2$ atmosphere. To assay for mitochondrial permeabilization, cells were stained with JC-1 according to the manufacturer's protocol and Hoechst 33342 (5 μM). Cells were imaged on an inverted epifluorescence microscope (Olympus IX-81). Images were taken using a Rolera-MGI Plus back-illuminated electron-multiplying charge-coupled device camera (QImaging). Filter cubes used included FITC (λex/λem = 450–490/500–550 nm) and RFP (λex/λem = 535–580/570–670 nm) (Chroma Technology). To quantify the extent of mitochondrial permeabilization within the populations, the cells were also analyzed by flow cytometry. Signals corresponding to the monomeric form of the JC-1 probe and the J-aggregate form were detected on a flow cytometer (BD Accuri C6 model) using standard FL1 (λex/λem = 488/533 ± 30 nm) and

FL2 ($\lambda ex/\lambda em$ = 488/585 ± 40 nm) channels, respectively. Data were acquired at a flow rate of 66 µL/min with 40,000 events.

To determine the presence of apoptotic cells, the Annexin V apoptosis assay was performed. Following the procedure for the cell viability assays, HeLa cells were seeded at 70% confluency and incubated for 8 hours. Compound 2 was dissolved in PBS with 4% v/v DMSO, diluted to working concentrations and added to the plates. Following 16 hours of incubation at 37 ºC in a 5% $CO_2$ atmosphere, the media in each well was replaced with L15 media (containing 10% FBS and 1% penicillin/streptomycin). Plates were then either kept in the dark at 37 ºC or irradiated in a UV/vis photoreactor LZC-14 (LuzChem Research, Inc.) equipped with 14 lamps ($\lambda_{irr}$>400 nm) for 2 hours. The cells were then incubated for 24 hours at 37 ºC in a 5% $CO_2$ atmosphere. To assay for apoptosis, cells were stained with FITC-Annexin V and propidium iodide following the manufacturer's protocol. Cells were then imaged on an EVOS M7000 Imaging System (Invitrogen). Filter cubes used included GFP ($\lambda_{ex}/\lambda_{em}$ = 459–481/500–550 nm) and RFP ($\lambda ex/\lambda em$ = 511–551/573–613 nm). To quantify the apoptotic responses of the populations, the cells were also analyzed by flow cytometry. Signals corresponding to FITC and propidium iodide were detected using FL1 and FL2 channels, respectively. Data were acquired as previously described.

## Results and Discussion

*Synthesis and Crystallography*

The mixed bridging ligand paddlewheel starting material **1** was synthesized by the dropwise stoichiometric addition of *N,N'*-bis(2,6-difluorophenyl)formamidine, deprotonated with $KO^tBu$ into a solution of $Rh_2(O_2CCH_3)_4$. The air and water stable product was purified by flash chromatography and characterized by $^1$H-NMR spectroscopy (Figure II.2) and X-ray crystallography (Figure II.3) Select bond distances are listed in Table II.1 and refinement parameters are summarized in Table II.2. The cationic $[Rh_2]^{4+}$ unit is supported by three acetate bridge groups and one $[F_2form]^-$ ligand with the axial positions being occupied by $CH_3CN$ ligands (Figure II.3). The Rh-Rh bond distance is 2.4114(10), which is in the range of other dirhodium carboxylate (2.35 – 2.45 Å) and formamidinate (2.37 – 2.45 Å) derivatives. Due to the *trans* influence, the average Rh-O (*trans* to $[F_2form]^-$) bond distance is 2.0595(9) Å, which is slightly longer than that of the acetates *cis* to the $[F_2form]^-$.

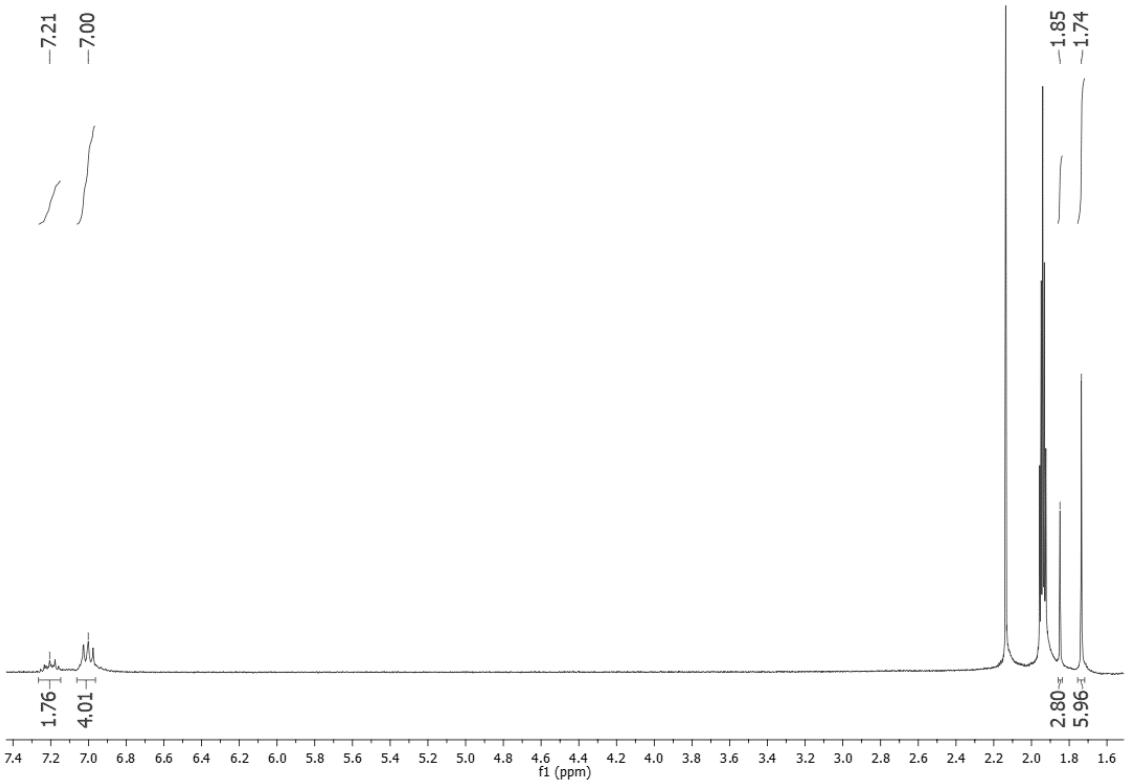


**Figure II.2** Full $^{1}$H-NMR spectrum of **1** in $CD_3CN$. Residual solvent peaks (ppm): 1.94 (acetonitrile); 2.13 (water).

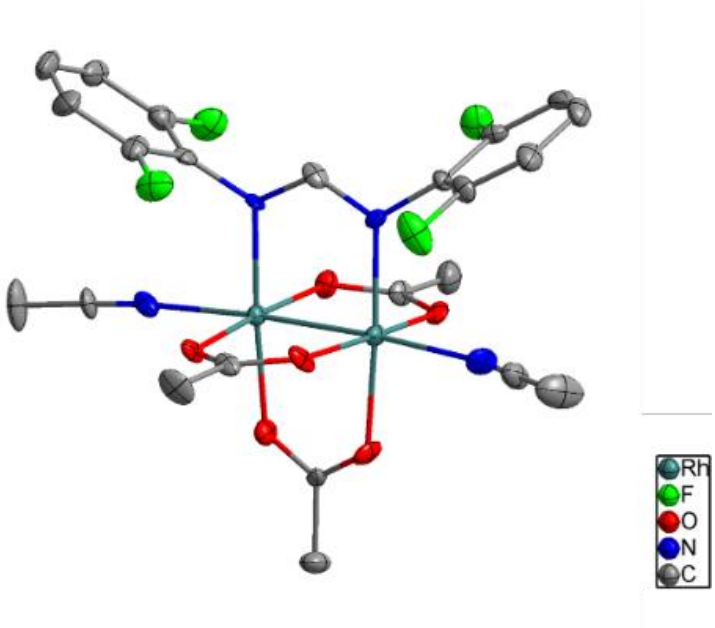


**Figure II.3** Thermal ellipsoid plot for 1 drawn at the 50% probability level. Interstitial solvent molecules and hydrogen atoms have been omitted for the sake of clarity

**Table II.1** Select bond distances and angles for **1**.

| **Bond** | **Length (Å)** | **Bond Angle** | **Angle (°)** |
|---|---|---|---|
| Rh1-Rh2 | 2.4114(1) | Rh2-Rh1-N3 | 176.116(4) |
| Rh1-O2 | 2.03808(14) | Rh1-Rh2-N4 | 176.556(3) |
| Rh1-O4 | 2.0513(7) | **Dihedral** | **Angle (°)** |
| Rh1-O6 | 2.0694(14) | N2-Rh1-Rh2-N1 | 6.782(5) |
| Rh1-N2 | 2.0172(8) | O2-Rh1-Rh2-O2 | 4.882(5) |
| Rh1-N3 | 2.2429(17) | O4-Rh1-Rh2-O3 | 6.436(4) |
| Rh2-O1 | 2.0216(15) | O5-Rh1-Rh2-O6 | 5.725(5) |
| Rh2-O3 | 2.0683(7) | | |
| Rh2-O5 | 2.0257(1) | | |
| Rh2-N1 | 2.0325(8) | | |
| Rh2-N4 | 2.2135(15) | | |

**Table II.2 .** Crystal structure parameters and refinement data for **1.**

| **Formula** | $C_{25}H_{25}F_4N_4O_6Rh_2$ |
|---|---|
| **Mol Wt. (g/mol)** | 773.30 |
| **Space group** | P1 |
| **a/Å** | 9.300(4) |
| **b/Å** | 9.846(4) |
| **c/Å** | 10.164(4) |
| **α/°** | 103.085(4) |
| **β/°** | 112.263(4) |
| **γ/°** | 110.373(4) |
| **Volume / A$^3$** | 735.4(5) |
| **Z** | 1 |
| **2 Θ range for data collection** | 52.822º |
| **$R_{int}$** | 0.0252 |
| **Goodness-of-fit (all data)** | 1.069 |
| **$R_1$, $wR_2$ (all data)** | $R_1$ = 0.0456<br>$wR_2$ = 0.0760 |

[a] $R_1 = \Sigma(||F_o| - |F_c||)/\Sigma|F_o|$.
[b] $wR_2 = [\Sigma[w(F_o^2 - F_c^2)^2]/\Sigma[w(F_o^2)^2]]^{1/2}$
$w = 1/[\sigma^2(F_o^2) + (ap)^2 + bp]$, where $p = [\max(F_o^2, 0) + 2F_c^2]/3$.

With this new robust starting material in hand, we capitalized on the substitutional lability of two acetate ligands to coordinate two diimine ligands to the $[Rh_2]^{4+}$ core. Two equivalents of dppn were added to a solution of $Rh_2(F_2Form)(O_2CCH_3)_3$ in acetonitrile and the mixture was refluxed for one week. The product $[Rh(F_2Form)(O_2CCH_3)(dppn)_2](O_2CCH_3)_2$ (**2**) was obtained as an acetate salt (Figure II.1, Figure II.4).

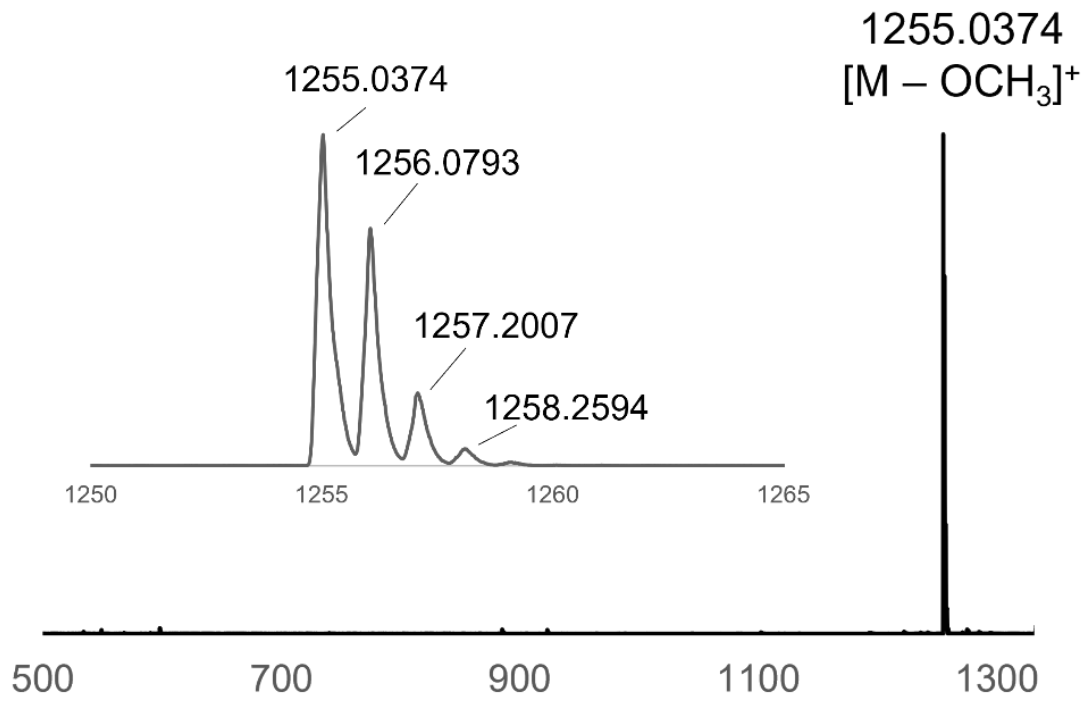


**Figure II.4** ESI-HRMS data for 2.

*Electronic Absorption Spectroscopy*

Electronic absorption spectral data for **1** and **2** in $CH_3CN$ are shown in Figure II.5. The transitions measured for **1** are typical of dirhodium carboxylate compounds.[25-27] More intense dppn $^1\pi\pi^*$ absorption bands at 318 nm ($\varepsilon$ = 104000 $M^{-1}cm^{-1}$) and in the 380–420 nm range ($\varepsilon \sim 20800\ M^{-1}cm^{-1}$) were observed for **2** and obscure the weaker metal-centered d-d transitions. The spectrum of **2** tails beyond 650 nm, and these lower energy features are likely $Rh_2(\delta^*)/F_2Form(\pi^*) \rightarrow dppn(\pi^*)$ charge transfer in nature as observed in related complexes.[28] Importantly, this near-IR region absorption is in the PDT window which is

necessary for tissue penetration in photochemotherapy applications.[46] TD-DFT calculations confirmed the assignment of these transitions

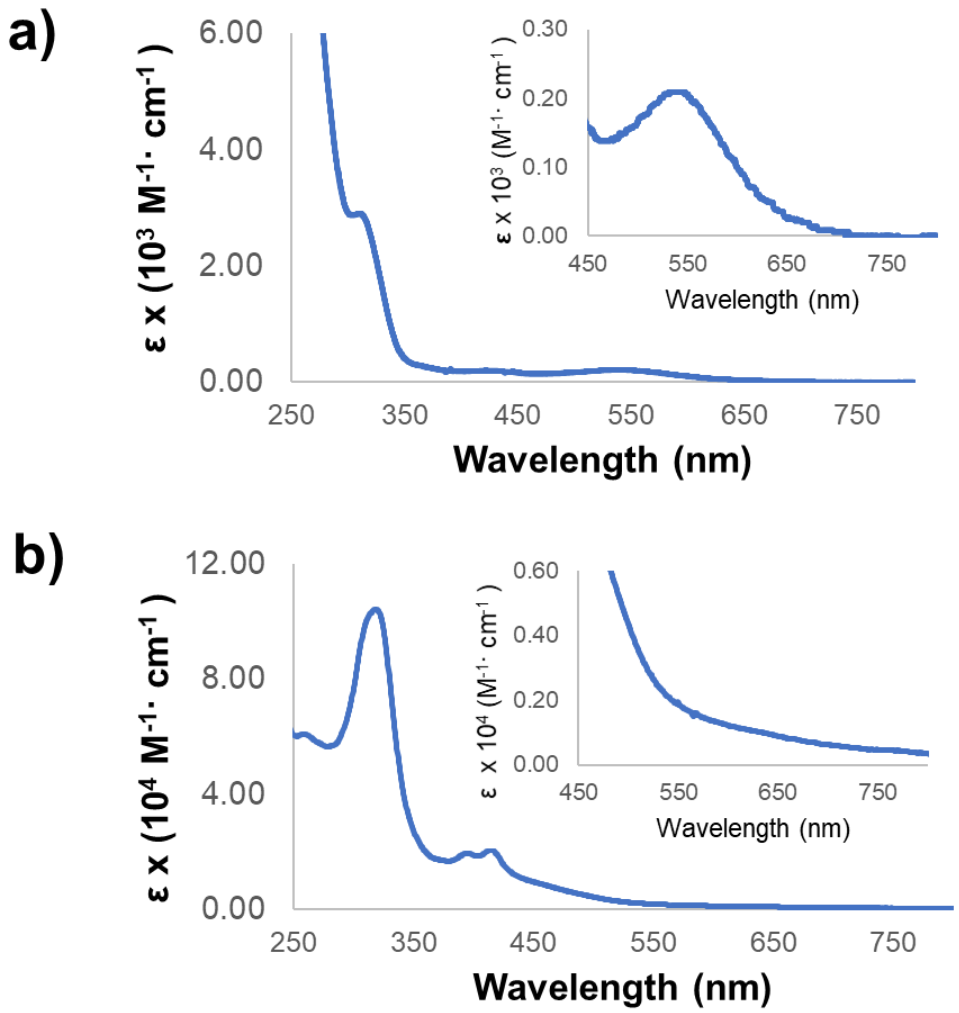


**Figure II.5** Electronic absorption spectra of (a) **1** and (b) **2** in $CH_3CN$.

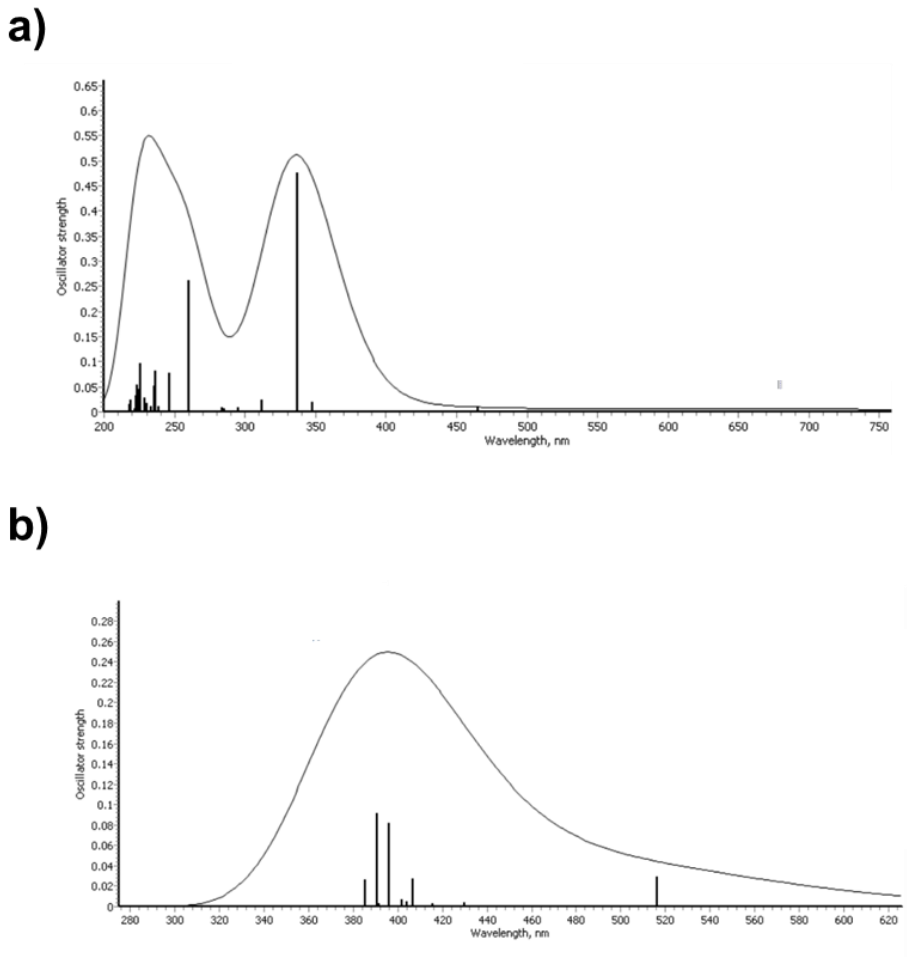


**Figure II.6** Calculated absorption spectra of (a) **1** and (b) **2**

*Transient Absorption Spectroscopy*

Excitation of **2** with a short pulse of light ($\lambda_{exc}$ = 400 nm, fwhm = 85 fs) in DMF:$CH_3CN$ results in the appearance of positive signals at 540 nm and 625 nm (Figure S4). The decay of the absorption feature at 625 nm can be fitted to a biexponential function with $\tau_1$ = 8 ps and $\tau_2$ = 390 ps. In contrast, little intensity change is observed for the peak at 540 nm from 300 fs to 500 ps but the signal begins to decay at ~2.5 ns. Only the broad band with maximum at 540 nm is observed at longer timescales, which decays

monoexponentially with $\tau$ = 318 ns upon 355 nm and 532 nm excitation (fwhm = 8 ns, under argon). The observation of a absoprtion at 540 nm with a long lifetime is consistent with a lowest energy dppn $^3\pi\pi^*$ state as found in related dppn complexes.[58, 87, 105, 106] The feature at 625 nm is attributed to the $Rh_2(\delta^*)/F_2Form(\pi^*) \rightarrow dppn(\pi^*)$ $^{1/3}$ML-LCT (metal/ligand-to-ligand charge transfer) excited state. Based on comparisons with related Ru(II) and $Rh_2$(II,II) complexes with dppn ligands, it is believed that the initially excited $^1$ML-LCT state intersystem crosses to the corresponding $^3$ML-LCT within 8 ps, which then populates the $^3\pi\pi^*$ state with a time constant of 390 ps (Figure II.7).

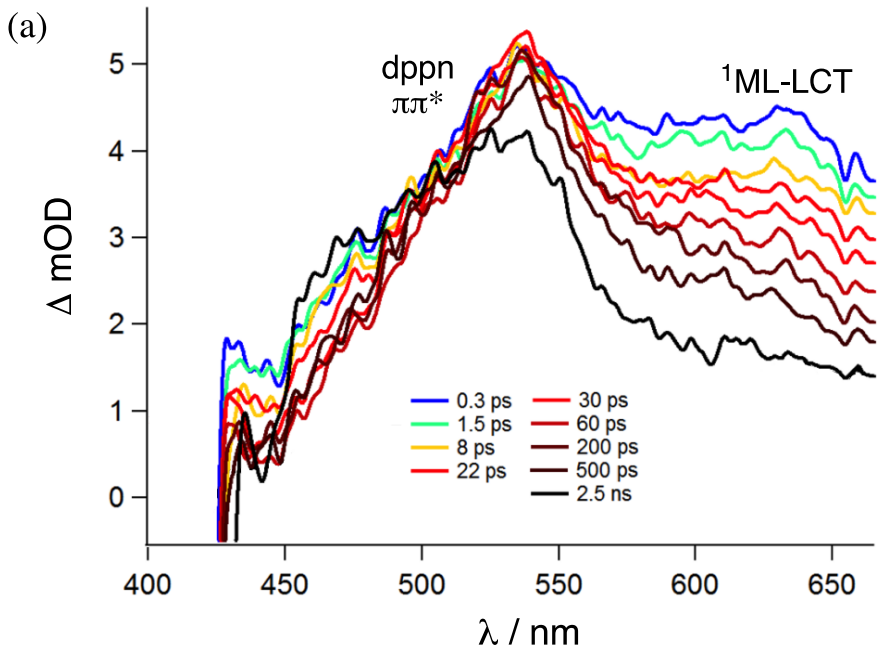


**Figure II.7** Transient absorption spectra of **2** in 1:1 DMF:$CH_3CN$ ($\lambda_{exc}$ = 400 nm, fwhm = 85 fs).

The $^3\pi\pi^*$ state of **2** is generates $^1O_2$ with quantum yield, $\Phi_\Delta$, of 0.58(8), which is similar to related dppn complexes.[106] This value is consistent with the quenching of the $^3\pi\pi^*$ lifetime from 318 ns under an argon atmosphere to 174 ns in air in DMF:$CH_3CN$ (1:1 v:v).

*DNA Photocleavage Experiments*

DNA electrophoretic mobility experiments revealed that **2** photocleaves plasmid DNA upon irradiation with visible light (Figure II.8a). Varying concentrations of **2** were incubated with pUC18 plasmid DNA and then irradiated ($\lambda_{irr} \geq 400$ nm, $t_{irr} = 1$ h) or kept in the dark for the same period of time. In the absence of light, DNA cleavage is not observed at concentrations of 1 μM and 10 μM for **2**, as evidenced by the fact that the relative intensities of supercoiled plasmid (Form I) and nicked circular plasmid (Form II) in lanes 4 and 5 are similar to the those of the control in lane 1 (Figure II.8a). Upon irradiation, there is an increase in the intensity of the band corresponding to Form II and a decrease in the amount of Form I in the presence of 10 μM of **2** (lane 3, Figure II.8a), compared to native DNA (lane 1, Figure II.7a). The ability of **2** to photocleave plasmid DNA is further supported by the irradiation time dependence studies, where an increasing amount of Form II is observed at increasing irradiation times (Figure II.8b).

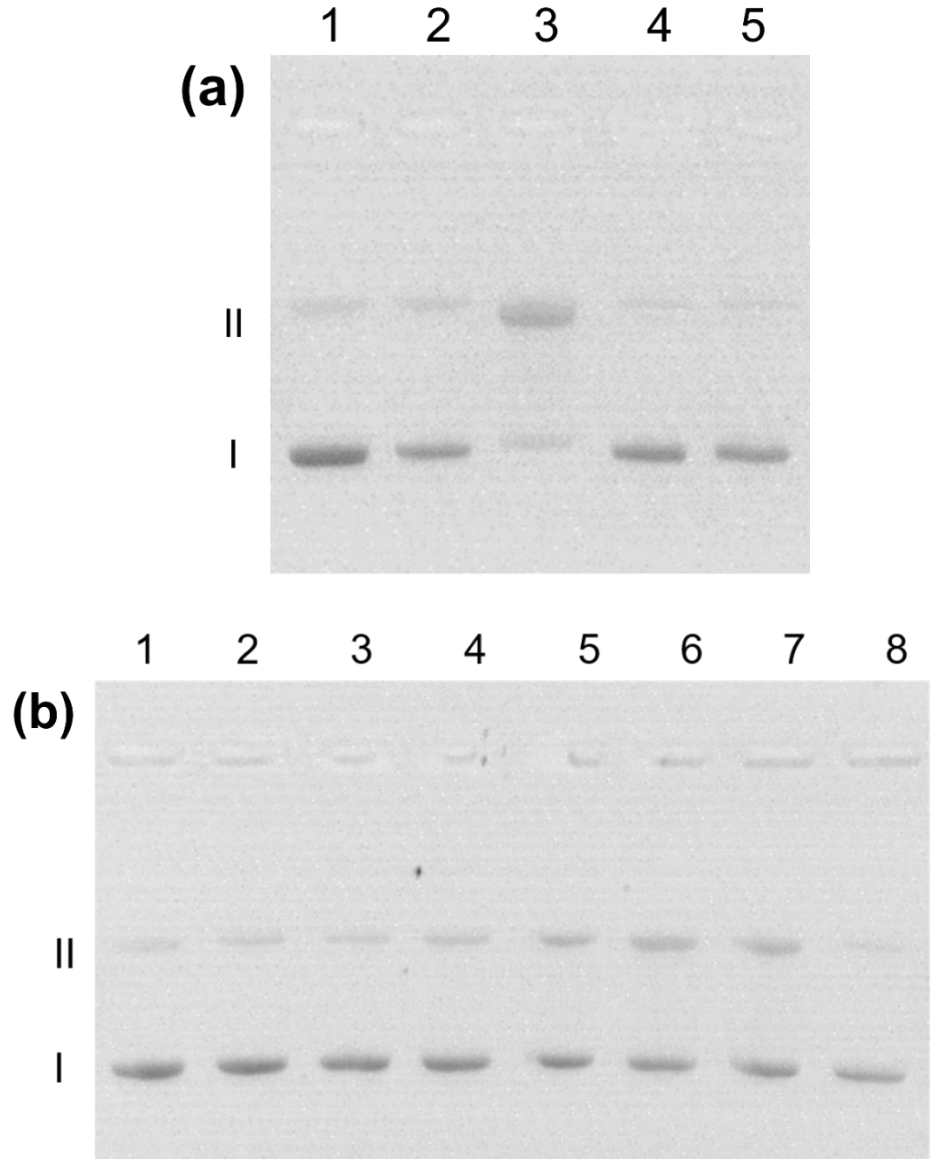


**Figure II.8** Ethidium bromide stained agarose gel of 15μg/μL pUC18 plasmid DNA (10mM TrisCl, pH=7) (a) in the presence of 1 μM (lanes 2, 4) and 10 μM (lanes 3, 5) of 2 in the dark (lanes 4, 5) and upon irradiation (lanes 2, 3); $\lambda_{irr} \geq 400$ nm, $t_{irr} = 1$ h) and plasmid alone (lane 1) and (b) incubated for 30 min total with 10 μM of 2 under increasing irradiation ($\lambda_{irr} \geq 400$ nm) times. Lane 1: plasmid alone; 2: 5 min; 3: 10 min; 4: 15 min; 5: 20 min; 6: 25 min; 7: 30 min; 8: dark

*In vitro Experiments*

The use of compound **2** as a potential PDT agent was additionally investigated by screening its anti-proliferative activity against HeLa cells using the resazurin cell viability assay. The photocytotoxicity index, PI, was determined to be 25.3 based on the ratio of the $LC_{50}$ values of 159 μM and 6.29 μM in the dark and upon irradiation with visible light, respectively. The high PI value exceeds those of previously published dirhodium PDT agents, for example *cis*-$[Rh_2(chp)_2(CH_3CN)_6][BF_4]_2$ with a PI of 16.4 in HeLa cells,[86] and is similar to that reported for *cis*-$[Rh_2(O_2CCH_3)_2(dppn)_2][BF_4]_2$ with a PI of 24 against HS-27 human skin fibroblasts.[31] Furthermore, the significant difference between light and dark toxicities, taken together with its low cytotoxicity in the dark, indicates that **2** is very promising for use as a PDT agent, a fact that merits further investigation with other cell lines.

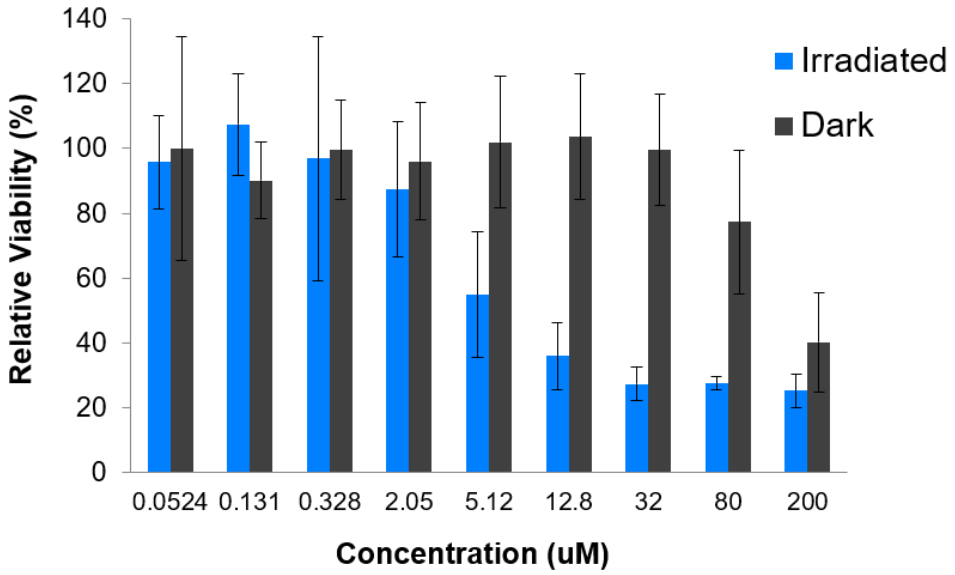


**Figure II.9** Photocytotoxicity of **2** against HeLa cells in the dark and upon irradiation ($\lambda_{irr} \geq 400$ nm $t_{irr} = 2$ h).

Flow cytometry and confocal microscopy methods (Figure II.10, Figure II.11, Figure II.12) were used to further investigate the photocytotoxicity and cell death mechanism of **2.** As some apoptotic pathways begin with, or proceed in conjunction with damage to the mitochondria, the JC-1 probe was used to determine whether **2** has an impact on mitochondrial polarization. Under basal conditions, JC-1 accumulates to form aggregates that emit a red fluorescence. Upon mitochondrial depolarization, the JC-1 probe instead remains in its monomeric form, emitting a green fluorescence. HeLa cells were incubated with **2** and the samples were then irradiated with visible light or kept in the dark for two hours. Cells alone and cells incubated with **2** in the dark displayed an overall red fluorescence of JC-1. However, the cells irradiated following incubation with **2** exhibited a decrease in red fluorescence and an increase in green fluorescence, indicating the mitochondria are less polarized than under basal conditions.

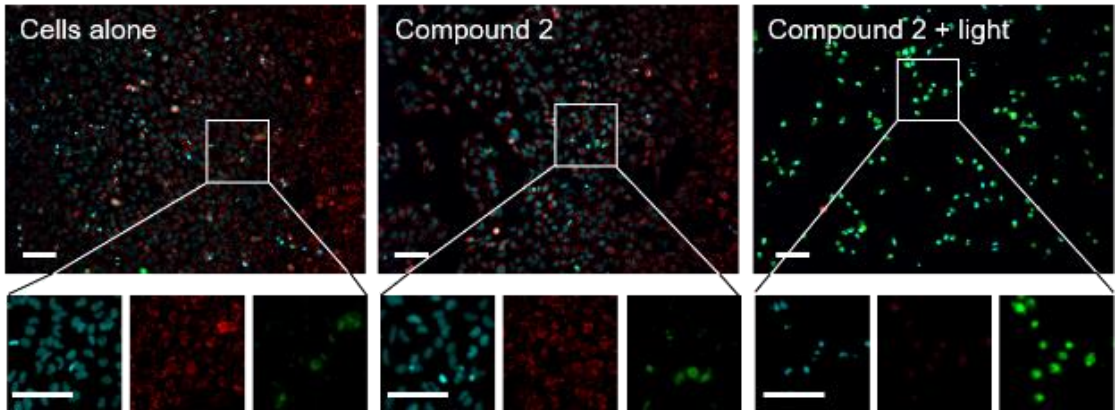


**Figure II.10** HeLa cells stained with JC-1 following incubation with **2** (24 hr), in the absence or presence of visible light (1 hr). Images are pseudo-green for JC-1 monomers, red for aggregate formation, and blue for Hoechst (scale bars = x20: 200 μm).

Annexin-V FITC and propidium iodide staining experiments were performed to determine the presence of apoptotic cells. Annexin V binds reversibly to the plasma membrane lipid phosphatidylserine, which flips to face the outer surface of a cell during apoptosis and emits a green fluorescence. Some propidium iodide staining was detected in the untreated cells, which exhibits a red fluorescence upon DNA binding in cells with compromised plasma membranes, a condition often associated with dead cells undergoing necrosis. Green fluorescence emission was predominantly detected in the treated cells, however, an indication of the binding of Annexin V to cells undergoing apoptosis. Notably, cellular blebbing was observed, which is a morphological signature of apoptosis. Flow cytometry was conducted on these cells to further confirm that irradiation of the cells resulted in increased cell death staining (Figure S5). Collectively, these observations indicate that the phototoxicity of **2** results in cell death that may proceed by either necrotic or apoptotic pathways.

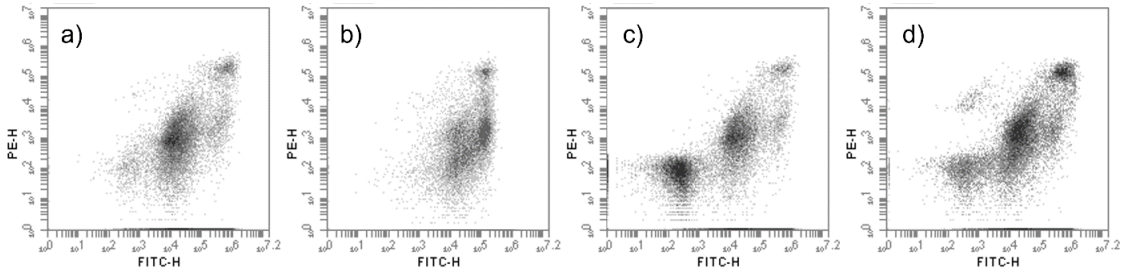


**Figure II.11** HeLa cells stained with FITC-Annexin V and PI, treated under various conditions: (a) Cells alone (b) staurosporine (c) cells + **2**, dark (d) cells + **2**, irradiated.

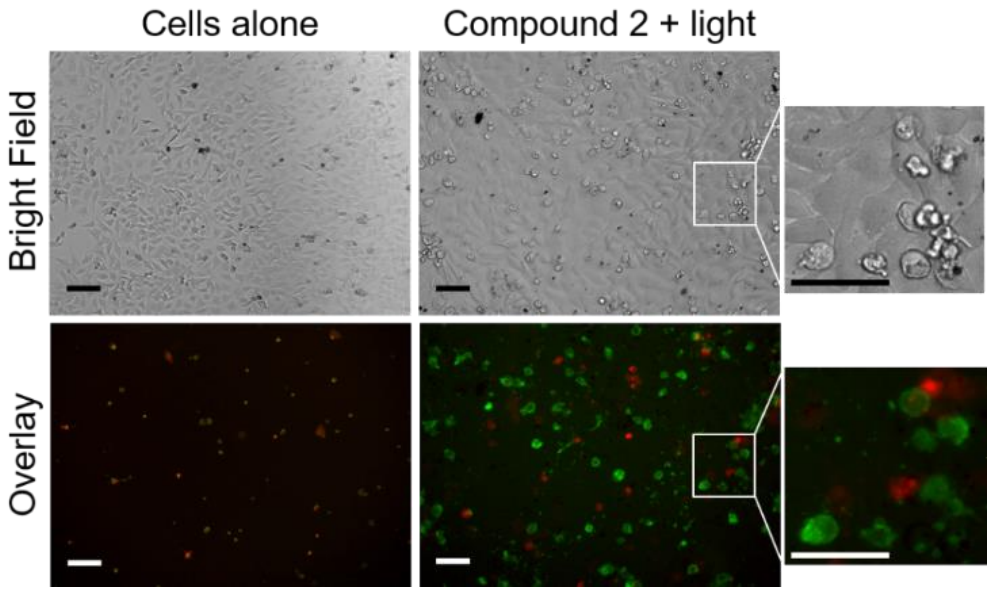


**Figure II.12** HeLa cells stained with FITC Annexin V and propidium iodide following incubation with **2** (24 hr) in the presence of visible light (1 hr). Images are pseudo-colored green for FITC Annexin V and red for propidium iodide (scale bars = x20: 200 μm).

**Conclusions**

In this chapter, a new mixed bridging ligand scaffold for the design of dirhodium photosensitizers was investigated as a precursor for potential PDT agents. Specifically, the starting material first reported by a previous Dunbar group member, $Rh_2$(F-Form)$(O_2CCH_3)_3$•$2O_2CCH_3$ was prepared and used to synthesize $[Rh_2(F_2Form)(O_2CCH_3)(dppn)_2](O_2CCH_3)_2$ which has a high $^1O_2$ quantum yield, is capable of DNA photocleavage, exhibits high photocytotoxicity against HeLa cells, and induces cell death through apoptotic as well as necrotic mechanisms as determined by confocal microscopy experiments. These findings demonstrate an exciting new platform upon which new metallodrugs and photosensitizers can be developed. In order to gain

deeper understanding of the promising mixed bridge ligand platform, the analogous $[Rh_2(F_2Form)_2(dppn)_2](PF_6)_2$ and $[Rh_2(O_2CCH_3)_2(dppn)_2](BF_4)_2$ complexes were synthesized. Preliminary cell viability studies indicate similar photocytotoxicity against HeLa cells in the case of the bis-formamidinate bridged complex. The photophysical differences are currently being studied, and preliminary data reveal that this new platform may be effective against resistant cell lines, which is an exciting avenue of investigation.

# CHAPTER III

# PHOTOSTABILITY AND STRUCTURAL EFFECTS OF HALOGEN SUBSTITUTED FORMAMIDINATE BRIDGING LIGANDS ON DIRHODIUM PARTIAL PADDLEWHEEL COMPLEXES

## Introduction

The first metal-metal multiple bond was first described in 1964, and, since that time, metal-metal bonding has been a popular topic that has been studied experimentally, spectroscopically and computationally.[3] Some of the most highly studied metal-metal bonded complexes are those of dirhodium(II,II) compounds with a single Rh-Rh bond. The interest in these complexes is due to the large variety of potential applications they exhibit, such as in the areas of catalysis, biomedical therapeutics, and photosensitizers.[4-7] The axial and equatorial coordination sites of these paddlewheel or partial paddlewheel structures allows these complexes to be easily functionalized and tuned for specific purposes, and harnessing this synthetic and structural control over the chemical and photochemical properties of the complexes is important for the design of new dirhodium scaffolds.[3]

The tunability of dirhodium complexes through ligand design has been established in many instances throughout the literature. For example, dirhodium(II,II) tetracarboxylate compounds of the type $Rh_2(\mu\text{-}O_2CR)_4$ (where R = Me, Et, Pr and Bu) were investigated for their anticancer properties and were shown to exhibit antitumor activity against Erlich ascites in mice.[34-36, 107] Across this series, the butyrate complex was shown to be the most

effective DNA inhibitor and exhibits the most potent antitumor activity. Dirhodium carboxylate compounds have also been extensively studied for catalytic applications. Bond insertion reactions were first studied by Teyssie and coworkers in 1973[12], and since then, the library of reactions catalyzed by rhodium acetate and derivative complexes has been intensively investigated. In the case of C-H functionalization catalysis, an example of the tunability of the dirhodium tetraacetate core includes designing the acetate bridging ligands with chiral moieties which results in much greater selectivity.[3, 108] Rational design of dirhodium complexes with more electron donating bridging ligands has also been an area of exploration. Step-wise replacement of acetate groups with the electron rich acetamide ligand raises the energy of the HOMO due to increased electron density around the rhodium core.[109, 110] Dirhodium formamidinate complexes have been studied in the Dunbar group for applications that take advantage of their strong electron donating properties. For example the ligands bis-p-tolyl formamidinate(DTolF) and p-fluorobenzylformamidinate (F-form) were used to bridge the rhodium atoms, and a red shift was observed in the absorbance of the complexes beyond what was achieved when acetates were used as bridging ligands, due to the more electron-donating character of the formamidinate ligands.[111] Furthermore, photophysical measurements revealed a metal centered long- lived $^3$ES with observed lifetimes of 2.4μs and 3.0μs for *cis*-[Rh2(μ-DTolF)$_2$(dppn)$_2$]$^{2+}$ and *cis*-[Rh$_2$(μ -F-Form)$_2$(dppn)$_2$]$^{2+}$, respectively.[111]

Starting material of the type "[Rh$_2$(L)$_2$(S)$_6$]$^{2+}$ (where L=bridging ligand, and S = a monodenate coordinating solvent ligand), referred to as "partially solvated" complexes, are used to prepare a variety of heteroleptic dirhodium complexes and are also interesting

in their own right.[3] These dirhodium complexes with equatorial solvent ligands are able to undergo light-induced ligand dissociation which makes them a target of interest for light activated applications such as photoactivated therapeutics or photocages for drugs. For example, the dirhodium bis-acetate partially solvated complex $[Rh_2(\mu\text{-}O_2CCH_3)_2(CH_3CN)_6]^{2+}$ covalently binds to biologically relevant molecules upon irradiation with loss of some of the acetonitrile ligands.[112] It was also found that the nitrogen donor bridged complex, *cis*-$[Rh_2(HNOCCH_3)_2(CH_3CN)_6]^{2+}$ undergoes photoinduced DNA binding following acetonitrile photodissociation.[88]

The aforementioned examples clearly indicate that structural modification of ligand environments in dirhodium complexes can have a profound effect on their electronic properties and reactivity. In this vein, when designing new complexes for their various applications, it is imperative to establish structure-function correlations. In the present study, the series $[Rh_2(X\text{-}Form)_2(MeCN)_6]^{2+}$ (where X = F, Cl, Br, I and X-Form = N,N'-bis(*p*-X-phenyl)formamidinate)) was synthesized and characterized. (Figure III.1). The aim was to extend the library of rhodium partially solvated complexes through functionalization of the formamidinate ligand with the halogen atoms. In previous work, halogen substitution resulted in an extended lifetime of the excited states beyond what is achieved with the DTolF ligand. We decided to attempt to optimize the design of dirhodium photosensitizers by systematically investigating the effect of the halogen on the structural and electronic properties of the compounds. X-ray crystallography, electronic absorption measurements, computational studies and time resolved NMR experiments

were all performed to elucidate understand trends in structure and ligand dissociation properties.

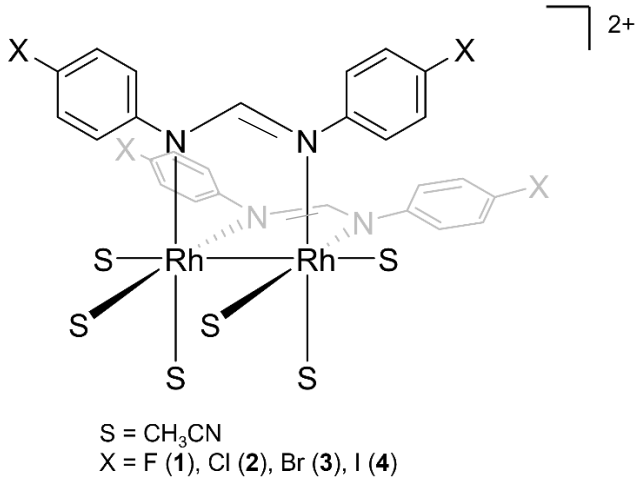


**Figure III.1** Structural representation of compounds **1-4.**

**Experimental Procedures**

*Materials*

The compound $[RhCl(COD)]_2$ (COD = 1,5-cyclooctadiene) was purchased from Pressure Chemicals and used without further purification as a starting material for the partially solvated compounds. The protonated forms of the formamidinate ligands N,N'-bis(*p*-fluorophenyl)formamidine (HF-Form), N,N'-bis(*p*-chlorophenyl) formamidine (HCl-Form), N,N'-bis(*p*-bromophenyl)formamidine (HBr-Form) and N,N'-bis(*p*-iodophenyl)formamidine (HI-Form) were synthesized according to literature methods[90] using 4-fluoroaniline, 4-chloroaniline, 4-bromoaniline and 4-iodoaniline, respectively, obtained from Oakwood Chemical and triethyl orthoformate from TCI which were used

without further purification. The synthesis of the precursors $[Rh(X\text{-}Form)(COD)]_2$ where X= F, Cl, Br, I, were adapted from a literature procedure,[113] and the compounds were used without further characterization or purification. The compound *cis*-$[Rh_2(\mu\text{-}F\text{-}Form)_2(CH_3CN)_6][BF_4]_2$ was synthesized following a literature procedure,[111] which was adapted and applied to the synthesis of the compounds *cis*-$[Rh_2(\mu\text{-}Cl\text{-}Form)_2(CH_3CN)_6][BF_4]_2$, *cis*-$[Rh_2(\mu\text{-}Br\text{-}Form)_2(CH_3CN)_6][BF_4]_2$ and *cis*-$[Rh_2(\mu\text{-}I\text{-}Form)_2(CH_3CN)_6][BF_4]_2$. Acetonitrile was dried over dried over 3Å molecular sieves and distilled under a $N_2$ atmosphere, dichloromethane was dried over $P_2O_5$ and distilled under a $N_2$ atmosphere, and diethyl ether was used as received. Standard Schlenk-line and glove box techniques under a $N_2$ atmosphere were used during synthesis, while work-up and isolation of products was performed in air unless otherwise stated.

***cis*-$[Rh_2(\mu\text{-}Cl\text{-}Form)_2(CH_3CN)_6][BF_4]_2$ (2):** Quantities of $[Rh(Cl\text{-}Form)(COD)]_2$ (163.8 mg, 0.1667 mmol) and $AgBF_4$ (172.9 mg, 0.8884 mmol) were added to a dark red flask and stirred at room temperature in 30 mL of $CH_2Cl_2$:$CH_3CN$ (1:1 v/v) for 24 hours. The resultant dark suspension was filtered over Celite® and the orange filtrate was evaporated to dryness. After redissolving in 5 ml of acetonitrile, diethyl ether was added to precipitate the red-brown crystalline product, which was collected by vacuum filtration on a fine frit. 75% (112.0 mg, 0.125 mmol). $^1$H-NMR ($CD_3CN$-*d3*), δ (ppm): 2.53 (s, eq $CH_3CN$), 7.05 (m, p-difchlorophenyl), 7.40 (m, p-dichlorophenyl), 7.49 (t, NCHN, 3JRh-H = 4 Hz).

***cis*-$[Rh_2(\mu\text{-}Br\text{-}Form)_2(CH_3CN)_6][BF_4]_2$ (3):** Following the used method to synthesize **2,** to a dark Schlenk flask was added $[Rh(Br\text{-}Form)(COD)]_2$ (500.8 mg, 0.4315 mmol) and $AgBF_4$ (986.5 mg, 5.085 mmol) along with 30 mL of $CH_2Cl_2$:$CH_3CN$ (1:1 v/v), and the

mixture was stirred at room temperature for 24 hours. A red-orange filtrate was obtained after filtering over Celite® and upon removing the solvent under vacuum, the resulting red-orange solid was redissolved in acetonitrile. The final product was obtained upon addition of diethyl ether and vacuum filtration. %Yield: 84% (482.7 mg, 0.362 mmol). $^1$H NMR (CD3CN-*d3*), δ (ppm): 2.51 (s, eq $CH_3CN$), 7.02 (m, p-dibromophenyl), 7.40 (m, p-dibromophenyl), 7.49 (t, NCHN, 3JRh-H = 4 Hz).

***cis*-[Rh$_2$(μ-I-Form)$_2$(CH$_3$CN)$_6$][BF$_4$]$_2$ (4):** Analogous to the preparation of **2** and **3,** [Rh(I-Form)(COD)]$_2$ (630.0 mg, 0.467 mmol) and $AgBF_4$ (760.5 mg, 3.91 mmol) were added to a flask with 30 mL of $CH_2Cl_2$:$CH_3CN$ (1:1 v/v) and stirred at room temperature for 24 hours. Upon filtration over Celite®, a dark red filtrate was obtained and solvent was removed under vacuum. The red solid was was redissolved in acetonitrile and treated with diethyl ether to precipiate the product. %Yield: 72% (511.1 mg, 0.336 mmol). $^1$H-NMR (CD3CN-*d3*), δ (ppm): 2.53 (s, eq $CH_3CN$), 7.05 (m, p-diiodophenyl), 7.40 (m, p-diiodophenyl),

*Instrumentation and Methods*

$^1$H-NMR spectra were collected on an Inova 500 MHz spectrometer with the chemical shifts being reported in ppm. The residual peak of the residual $CD_3CN$-$d_3$ deuterated solvent signal at 1.94 ppm[92] was used as the reference for the chemical shifts. The rate and activation energy of equatorial acetonitrile dissociation and exchange was determined by preparing solutions of **1**, **2**, **3** and **4** in $CD_3CN$-$d_3$ and monitoring the samples by $^1$H-NMR spectroscopy. The resonance corresponding to the protons of the equatorially bound acetonitrile molecules (approx. 2.5ppm) was integrated with respect to

the resonances corresponding to the protons of the formamidinate ligand (approx. 7.3 ppm). Plotted over time, a mono-exponential decay fitting was used to determine the rate at various temperatures. To compare light versus dark dissociation, samples were irradiated in a UV/vis photoreactor LZC-14 (LuzChem Research, Inc.) equipped with 14 lamps ($\lambda_{irr}$>400 nm). Elemental analyses were performed at Atlantic Microlabs Inc. Electronic spectroscopy was performed on a Shimadzu UV-1601PC spectrophotometer using 1 x 1 cm quartz cuvettes, and absorption spectra were obtained in triplicate.

Single crystals of **2**, **3** and **4** were selected under ambient conditions from oil using a MiTeGen microloop. The X-ray data sets were collected on a Bruker CCD APEX diffractometer with graphite monochromated Mo Kα radiation (λ = 0.71073 Å). The initial unit cells were determined using SAINT from a set of three ω-scans consisting of 0.5° frames and a sweep width of 15°. APEX2 was used to determine the data collection to collect all independent reflections to a resolution of at least 0.82 Å. Full details of the data collection and refinement parameters are presented in Table III.1. The data were corrected for absorption using SADABS,[93] and the space groups were determined from analysis of the systematic absences and E-statistics using XPREP. The structures were solved using the intrinsic phasing routine in SHELXT or by direct methods implemented in SHELXS. The non-hydrogen atoms were located from Fourier difference maps by least-squares refinement of the structure using SHELXL-2014.[94] All non-hydrogen atoms were refined anisotropically and hydrogen atoms were placed in calculated positions and refined with thermal parameters constrained to their parent atom. DIAMOND was used to

generate the molecular graphics. Specific details of the refinements are presented in Table III.1.

Density Functional Theory (DFT) calculations for molecular and electronic structures were performed using the Gaussian (16) program package.[95] The MPW1PW91 correlation and exchange functional was used with the with the Stuttgart RSC 1997 Electron Core Potential (ECP) basis set for the Rh and I atoms and the 6-31G(d') basis set for the C, N, F, Cl, Br and H atom. The starting geometries for the gas-phase optimizations were taken from the crystal structure of the complexes, excluding the counterions and solvent molecules. Time-Dependent Density Functional Theory (TD-DFT) calculations were performed using the polarized continuum model (PCM)[114] with acetonitrile as the solvent. From the optimized singlet ground state geometry, the first sixty lowest singlet-to-singlet excited states were calculated. The graphic software 'Gaussview' was used to plot the molecular orbitals with iso-values of 0.03. the Chemissian Visualization Computer Program was used to analyze molecular orbital contributions.[102]

**Results and Discussion**

*Synthesis***.**

Compounds **1-4** were prepared by reacting $[RhCl(COD)]_2$ with deprotonated formamidine in toluene to produce $[Rh(Form)(COD]_2$ salt, which were oxidized with silver tetrafluoroborate (Figure III.2). Upon removal of residual silver by filtration, the resulting dark orange-red solutions concentrated under vacuum. Addition of diethyl ether precipitated the desired compounds as dark red or brown microcrystalline solids.

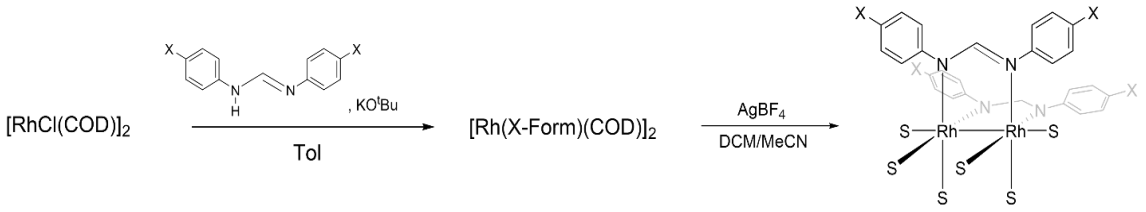


**Figure III.2** Generalized synthetic scheme for the synthesis of formamidinate bridged dirhodium partially solvated complexes.

*Crystallography*

Single crystals of **2**, **3** and **4** were obtained via slow diffusion of diethyl ether into concentrated acetonitrile solutions of the respective compounds at room temperature. All compounds crystallized readily into dark orange or red blocks. The molecular structures of these compounds are shown in III.3 and the refinement parameters are compiled in Table III.1 Analogous to the previously published compound **1,** compounds **2-4** also consist of a Rh-Rh unit with bond lengths of 2.572, 2.575, and 2.574 Å for **2**, **3** and **4**, respectively, data that are comparable to **1** with a corresponding distance of 2.571 Å. The dicationic dirhodium center is supported by two anionic formamidinate bridging ligands in a *cis* configuration, and the remaining equatorial and axial coordination sites are occupied by six acetonitrile ligands. In addition, there are two $[BF_4]^-$ counterions.

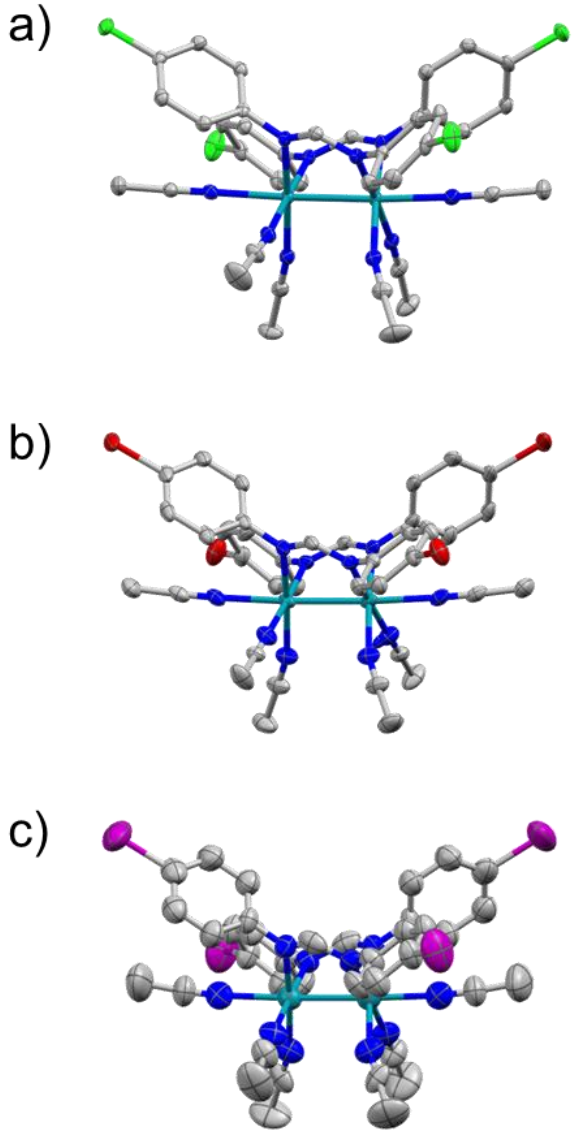


**Figure III.3** Thermal ellipsoid plots for the dication in (a) **2**, (b) **3** and (c) **4** drawn at the 50% probability level. Interstitial solvent molecules and hydrogen atoms have been omitted for the sake of clarity.

**Table III.1** Refinement parameters and crystal structure data for **2-4.**

| Compound | **2** | **3** | **4** |
|---|---|---|---|
| Empirical Formula | $C_{40}H_{39}B_2F_8Cl_4N_{11}Rh_2$ | $C_{80}H_{78}B_4F_{16}Br_8N_{22}Rh_4$ | $C_{40}H_{36}B_2F_8I_4N_{11}Rh_2$ |
| Formula weight | 1195.06 | 2745.80 | 1557.84 |
| Temperature/K | 110.0 | 110.0 | 110.0 |
| Crystal system | monoclinic | monoclinic | monoclinic |
| Space group | $P2_1/n$ | P2/n | P2/n |
| a/Å | 12.5252(3) | 12.6812(4) | 13.080(4) |
| b/Å | 32.5965(8) | 16.2232(5) | 16.866(6) |
| c/Å | 13.2716(3) | 13.5309(4) | 13.971(55) |
| α/° | 90 | 90 | 90 |
| β/° | 115.520(1) | 116.229(2) | 117.296(19) |
| γ/° | 90 | 90 | 90 |
| Volume/Å$^3$ | 4889.8(2) | 2497.08(13) | 2749.0(11) |
| Z | 4 | 1 | 2 |
| $\rho_{calc}$g/cm$^3$ | 1.623 | 1.826 | 1.889 |
| μ/mm$^{-1}$ | 0.967 | 9.723 | 2.922 |
| F(000) | 2384.0 | 1336.0 | 1474.0 |
| Crystal size/mm$^3$ | 0.2 x 0.1 x 0.1 | 0.3 × 0.2 × 0.1 | 0.3 x 0.1 x 0.1 |
| Radiation | MoKα (λ = 0.71073) | MoKα (λ = 0.71073) | MoKα (λ = 0.71073) |
| 2Θ range for data collection/° | 52.91 | 149.3 | 47.0 |
| Index ranges | -15 ≤ h ≤ 15<br>-40 ≤ k ≤ 40<br>-16 ≤ l ≤ 16 | -15 ≤ h ≤ 15<br>-20 ≤ k ≤ 20<br>-16 ≤ l ≤ 16 | -14 ≤ h ≤ 14<br>-18 ≤ k ≤ 18<br>-15 ≤ l ≤ 15 |
| Reflections collected | 10053 | 5097 | 3994 |
| Goodness-of-fit on F$^2$ | 1.126 | 1.110 | 1.032 |
| Final R indexes [all data] | $R_1$ = 0.0290<br>$wR_2$ = 0.0685 | $R_1$ = 0.0425<br>$wR_2$ = 0.1080 | $R_1$ = 0.0843<br>$wR_2$ = 0.2653 |

[a] $R_1 = \Sigma(||F_o| - |F_c||)/\Sigma|F_o|$.

[b] $wR_2 = [\Sigma[w(F_o^2 - F_c^2)^2]/\Sigma[w(F_o^2)^2]]^{1/2}$

$w = 1/[\sigma^2(F_o^2) + (ap)^2 + bp]$, where $p = [\max(F_o^2, 0) + 2F_c^2]/3$.

Across this series of halogenated formamidinate complexes, there is a general trend of a shortening of the average Rh-N bond distance with increasing halogen size from fluorine to chlorine to bromine to iodine. The average Rh-$N_{Form}$ distances are 2.038, 2.023, 2.024, 1.986 Å for **1**, **2**, **3,** and **4,** respectively. This trend is also observed for the axial acetonitrile ligands, for which the Rh-N distances are 2.251, 2.216, 2.205 and 2.175 Å, as well as the average distance between the rhodium atom and the equatorial acetonitrile ligands, with distances of 2.032, 2.021, 2.015, and 1.980 Å for **1, 2, 3** and **4,** respectively. These trends are consistent with the electronegativity of the halogen constituents as well as the *trans* influence and pi accepting properties of the formamidinate ligands. The overall longer average bond distances in **1** may be due to the increased electronegativity of the fluorine atom, which decreases electron density from the metal centers. As the electronegativity of the subsequent halogen moieties decreases, this increase in donor strength of the formamidinate in complexes **2**, **3**, and **4** is evidenced by the decrease in Rh-N (form) bond length across the series. However, the decrease in electronegativity may also have an effect on the π-accepting abilities of the formamidinate ligand, as the the fluorinated formamidinate ligand is the most pi-accepting in the group. The *trans* influence of the pi-accepting properties of the more electronegatively substituted bridging ligands is reflected the increased Rh-$NCCH_3$ bond distances.

A deviation from an eclipsed confirmation for equatorial acetonitrile ligands and the bridging formamidinate ligands is observed crystallographically. The torsion angle between $N_{eq}$-Rh-Rh-$N_{eq}$, for the four complexes are between 17.901º and 22.953º, which is consistent with other complexes in the literature but does not appear to follow an

apparent trend. This may be attributed to disorder and crystal packing effects in the crystal structure. The $N_{form}$-Rh-Rh-$N_{form}$ torsion angles increase through the series, with measurements of 17.967º, 18.365º, 19.782º and 19.491º for **1, 2, 3** and **4,** respectively. The twist of the formamdinate ligand is easily observed in the crystal structure.

*Electronic Absorption:*

The electronic absorption maxima for **1-4** are listed in Table III.3 and the spectra shown in Figure III.4.

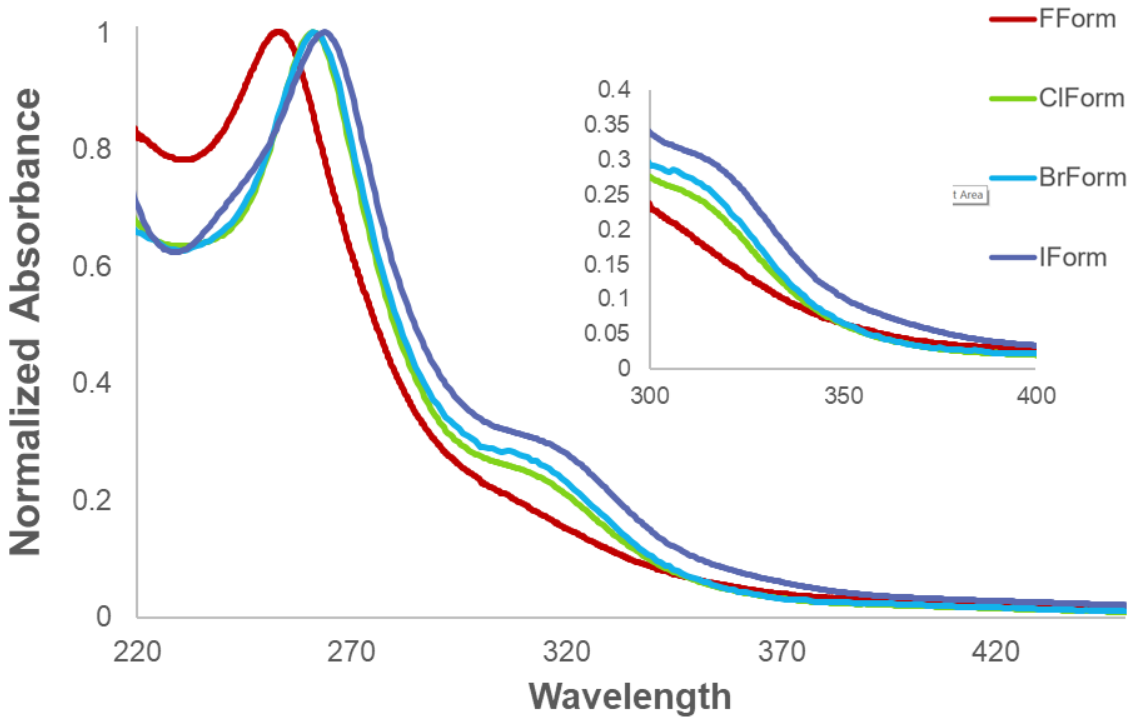


**Figure III.4** Normalized absorption spectra of **1-4** in acetonitrile, comparing the red-shift of absorbance in the UV region; with the inset showing the shoulder.

The absorption features of **2-4** are similar to that previously described **1,** due the analogous structure and electronic similarities across this series.[111] The intense absorption centered around 260 nm is attributed to a metal-centered transition with contributions from the ligands, based on assignments for other partially solvated complexes. This feature appears at 253 nm in the case of **1,** and there is a small red shift of the absorption wavelength in the case of **2**, **3** and **4** for which the feature can be observed at 261 nm, 263 nm and 264 nm, respectively. In addition to the intense peak at ~260 nm, a number of shoulders were observed for **2-4,** consistent with those previously reported for **1**. These shoulders attributed to Rh2($\pi^*$) → Rh2($\sigma^*$) transitions. A small red-shift of the absorbance is observed with the less electronegative substituent resulting in a more red-shifted spectrum.

**Table III.2** Electronic absorption maxima with molar absorptivities in acetonitrile.

| Complex | $\lambda_{abs}$ / nm ($\varepsilon$ / $\times 10^3$ $M^{-1}$ $cm^{-1}$) |
|---|---|
| **2** | 261 (153), 314 (51), 528 (2.3) |
| **3** | 263 (179), 315 (63), 536 (1.9) |
| **4** | 264 (177), 318 (62), 539 (2.5) |

*NMR Spectroscopy*

The $^{1}$H-NMR spectra of **2, 3** and **4** (Figure III.5, III.6, III.7) are consistent with the data previously reported for **1**. The singlet resonance at 2.51ppm is attributed to the protons of the equatorial acetonitrile molecules, whereas the axial solvent ligands are too labile to be observed. Similar to the case of **1**, the characteristic triplet corresponding to the bridge-head H atoms on the [X-form]$^{-}$ (X= Cl, Br, I) ligand is observed at 7.48ppm for **2**, **3** and **4**, respectively. Unlike the case of **1** for which the protons of the formamidinate phenyl ring appear as a multiplet at 7.05 ppm, the resonances for the phenyl ring protons of the formamdinate ligand of **2**, **3** and **4** are clearly observed as two doublets. The absence of the spin active $^{19}$F nucleus results in a lack of fine structure and these two doublets can be easily assigned to the protons closest to the halogen substituted position and the protons closer to the coordination site to the dirhodium core. The more downfield resonance can be assigned as the proton closer to the halogen, and the more upfield resonance is attributed to the proton closer to the rhodium core.

To determine the rate of ligand dissociation and photolability of the equatorially coordinated acetonitrile ligands, a series of time-dependent $^{1}$H-NMR experiments under ambient conditions were performed. Samples were prepared in deuterated acetonitrile and kept in the dark or in a visible light ($\lambda > 400$nm) irradiation chamber. The exchange of the equatorial ligands with solvent was observed by integrating the signal attributed to the equatorial acetonitrile molecules with respect to the signals corresponding to the phenyl ring of the formamidinate ligands. Over time, due to exchange with deuterated solvent, the area of this peak decreases, and the ligand exchange process was followed to

completion (Figure III.8). The rate of these processes for each complex was determined by a linear fit of the first-order reaction kinetics (Figure III.9). All four complexes were exhibit ligand dissociation and exchange over time in the dark, taking upwards of 6 hours to fully exchange in the case of **2**, **3** and **4.** Upon irradiation, this process proceeds much more rapidly with approximately a two-fold increase in rate. The identity of the substituted halogen has an effect on the overall stability of the complex in the dark. The average rate constant was determined to decrease in order of ,**1**, **2 3** and **4** with **1** showing the fastest ligand exchange ($k = 3.64 \times 10^{-4}$) and **4** the slowest ($1.50 \times 10^{-4}$). The rate constants for complexes **2** and **3** were determined to be $1.93 \times 10^{-4}$ and $1.83 \times 10^{-4}$, respectively (Table III.3). The trend observed is consistent with the *trans* effect and correlates with the shortening of Rh-N bond distances through the series. Compound **1** has the formamidinate ligand with the most electronegative constituent F, for which the strongest *trans* effect is observed, and is the compound with the longest Rh-N bonds. The ligand dissociation trends are consistent with these electronic and structural considerations.

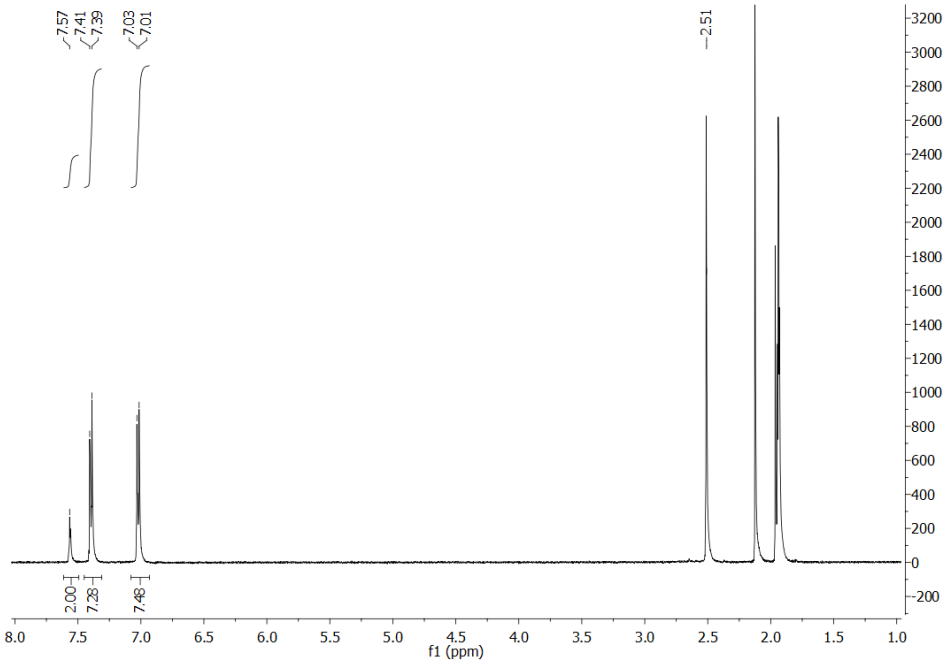


**Figure III.5** Full $^{1}$H-NMR spectrum of **2** in $CD_3CN$. Residual solvent peaks (ppm): 1.94 (acetonitrile); 2.13 (water).

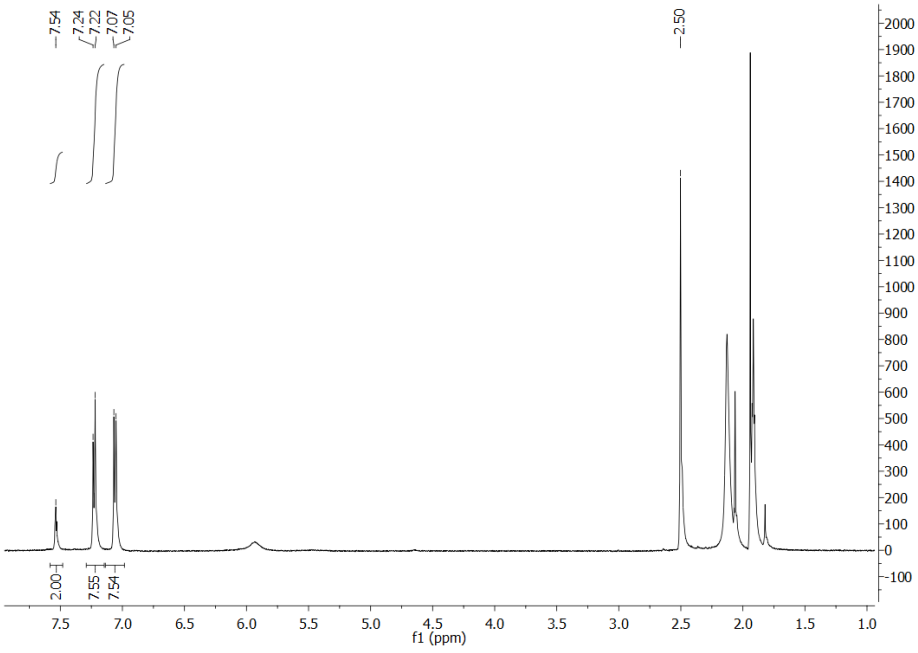


**Figure III.6** Full $^{1}$H-NMR spectrum of **3** in $CD_3CN$. Residual solvent peaks (ppm): 1.94 (acetonitrile); 2.13 (water).

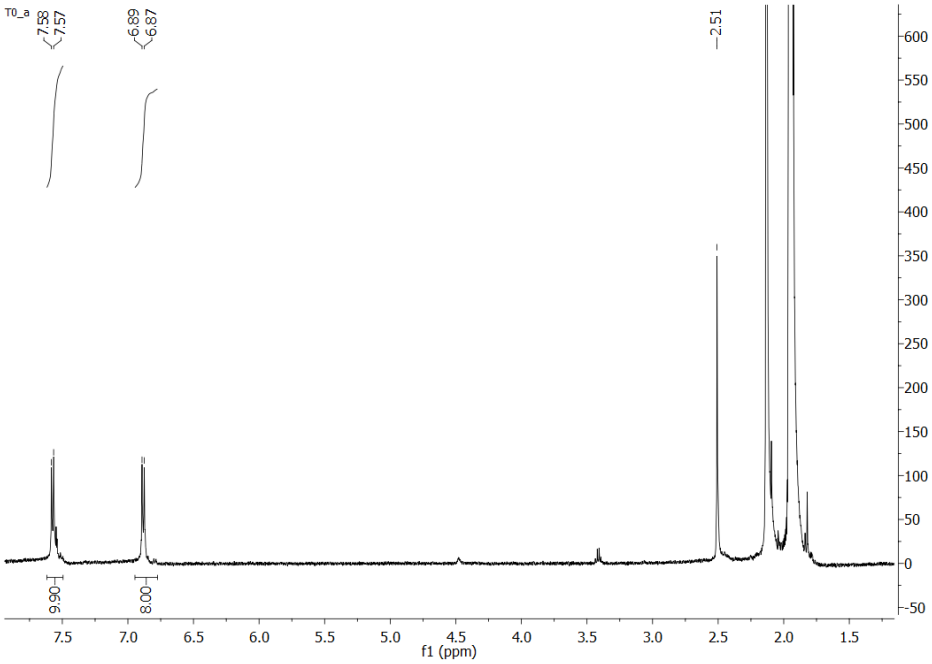


**Figure III.7** Full $^{1}$H-NMR spectrum of **3** in $CD_3CN$. Residual solvent peaks (ppm): 1.94 (acetonitrile); 2.13 (water); 3.42 (diethyl ether).

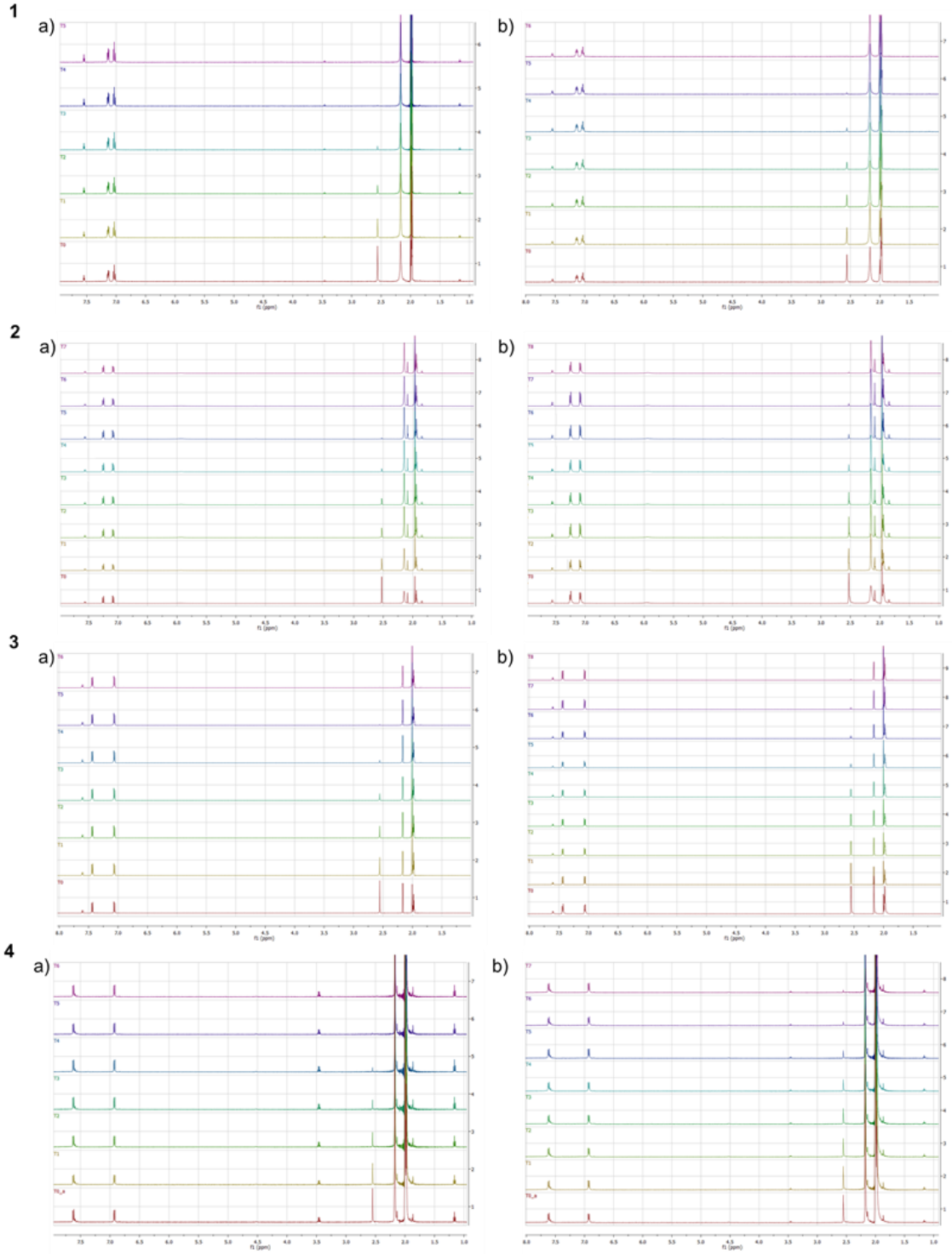


**Figure III.8** Time dependent NMR studies of **1-4** in $CD_3CN$ (a) irradiated ($\lambda > 400$nm) or (b) dark. T0 = 0 min, T1 = 20 min T2= 40 min T3= 60 min T4= 90 min T4 = 135 min T5= 180 min T6 = 240 min T7 = 300 min T8 = 360 min

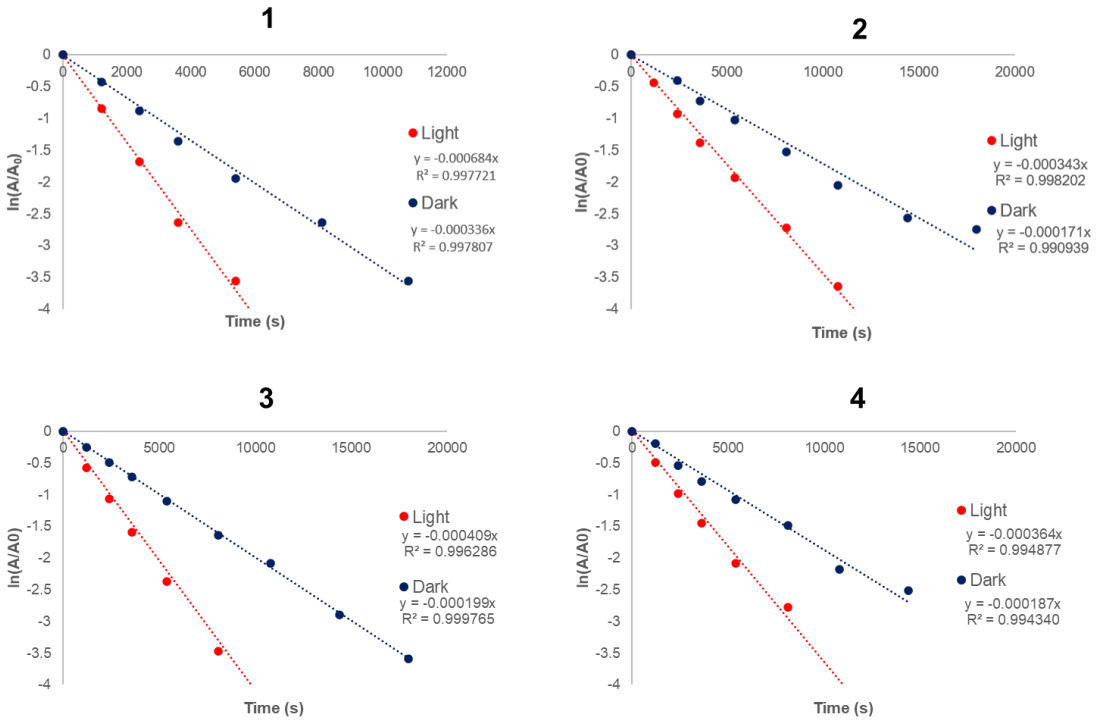


**Figure III.9** Determination of the rate constant of ligand exchange for complexes **1-4**.

**Table III.3.** Average rate constants for ligand exchange in the dark for complexes **1-4**.

| Complex | k (x $10^{-4}$) |
|---|---|
| **1** | 3.64 |
| **2** | 1.93 |
| **3** | 1.83 |
| **4** | 1.50 |

*Electronic Structure Calculations*

DFT calculations were performed to gain insight into the electronic and structural features of this series, and to help support and further elucidate the experimentally observed patterns. The geometric parameters from the crystal structures of **1-4** were used as starting points for the gas-phase geometry optimization calculations, and the computational results are in close agreement with the crystallographic parameters. Similar to the experimental results, a small decrease was noted in the average Rh-N bond distances as the electronegativity of the substituted halogen decreases. However, the difference was much less pronounced computationally, with a difference of approximately 0.02 Å in the Rh-N(eq) bond distance from **1** to **4**, compared to experimentally wherein the change in bond distance was approximately 0.75 Å. The calculated dihedral angles as defined by the formamidinate ligand and the dirhodium core are in good agreement with the X-ray diffraction data. The optimization results calculated for **2-4** are also consistent with those previously described for **1.** Molecular orbital contributions were determined for **1**-**4** and perturbations to the usual $\sigma^2\pi^4\delta^2\delta^{*2}\pi^{*4}\sigma^{*0}$ $Rh_2$(II,II) overlap scheme should be noted. Coordination of the two strongly donating formamidinate ligands stabilizes the $Rh_2(\delta^*)$ orbital below the $Rh_2(\delta)$ orbital. The $Rh_2(\delta^*)$ orbital is able to interact with the formamidinate p-orbitals, as well as the $\pi^*$ orbital of the equatorial acetonitrile ligands. The energy of the $Rh_2(\sigma)$ orbital is also substantially increased in the partially solvated complexes which can be attributed to interactions with the axial acetonitrile ligands. This situation is analogous to the DTolF partially solvated complex[115] and is consistent across the halogenated formamidinate series.

**Table III.4** Gas-phase optimized calculated bond distances and angles for **2-4**

| **2** | | **3** | | **4** | |
|---|---|---|---|---|---|
| **Bond** | **Length (Å)** | **Bond** | **Length (Å)** | **Bond** | **Length (Å)** |
| Rh1-Rh2 | 2.57803 | Rh1-Rh2 | 2.57743 | Rh1-Rh2 | 2.57722 |
| Rh1-N4 | 2.04776 | Rh1-N4 | 2.048760 | Rh1-N4 | 2.04731 |
| Rh1-N5 | 2.04019 | Rh1-N5 | 2.04022 | Rh1-N5 | 2.04035 |
| Rh1-N6 | 2.04287 | Rh1-N6 | 2.04271 | Rh1-N6 | 2.04260 |
| Rh1-N9 | 2.04634 | Rh1-N9 | 2.04641 | Rh1-N9 | 2.04647 |
| Rh1-N11 | 2.22379 | Rh1-N11 | 2.22409 | Rh1-N11 | 2.22361 |
| Rh2-N3 | 2.04634 | Rh2-N3 | 2.04641 | Rh2-N3 | 2.04647 |
| Rh2-N7 | 2.04019 | Rh2-N7 | 2.04022 | Rh2-N7 | 2.04035 |
| Rh2-N8 | 2.04287 | Rh2-N8 | 2.04271 | Rh2-N8 | 2.04260 |
| Rh2-N10 | 2.04776 | Rh2-N10 | 2.04760 | Rh2-N10 | 2.04731 |
| Rh2-N13 | 2.22379 | Rh2-N13 | 2.22409 | Rh2-N13 | 2.22361 |
| **Bond Angle** | **Angle (°)** | **Bond Angle** | **Angle (°)** | **Bond Angle** | **Angle (°)** |
| Rh1-Rh2-N13 | 178.49729 | Rh1-Rh2-N13 | 178.44937 | Rh1-Rh2-N11 | 178.43259 |
| Rh2-Rh1-N11 | 178.47920 | Rh2-Rh1-N11 | 178.44940 | Rh2-Rh1-N11 | 178.43291 |
| **Dihedral** | **Angle (°)** | **Dihedral** | **Angle (°)** | **Dihedral** | **Angle (°)** |
| N5-Rh1-Rh2-N3 | 17.94764 | N5-Rh1-Rh2-N3 | 18.06580 | N5-Rh1-Rh2-N3 | 18.18315 |
| N9-Rh1-Rh2-N7 | 17.94754 | N9-Rh1-Rh2-N7 | 18.06448 | N9-Rh1-Rh2-N7 | 18.18288 |
| N4-Rh1-Rh2-N8 | 26.40748 | N4-Rh1-Rh2-N8 | 26.52551 | N4-Rh1-Rh2-N8 | 26.69662 |
| N6-Rh1-Rh2-N10 | 26.40734 | N6-Rh1-Rh2-N10 | 26.52556 | N6-Rh1-Rh2-N10 | 26.69699 |

The energies of the HOMO and LUMO orbitals for **1-4** are comparable with those calculated for other dirhodium partially solvated complexes, though they are slightly lower in energy. There is a decrease in both the HOMO and LUMO energy from complexes **1-4**, ranging from -5.882 eV to -6.026 eV in the case of the HOMOs, and -2.201 eV to -2.308 eV for the LUMOs (Figure III.10). TD-DFT/PCM calculations were performed to determine the origin of the electronic transitions, most of which involve the HOMO or lower energy orbitals and LUMO or the LUMO+1. The calculated electronic absorption spectra are shown in Figure III.11.

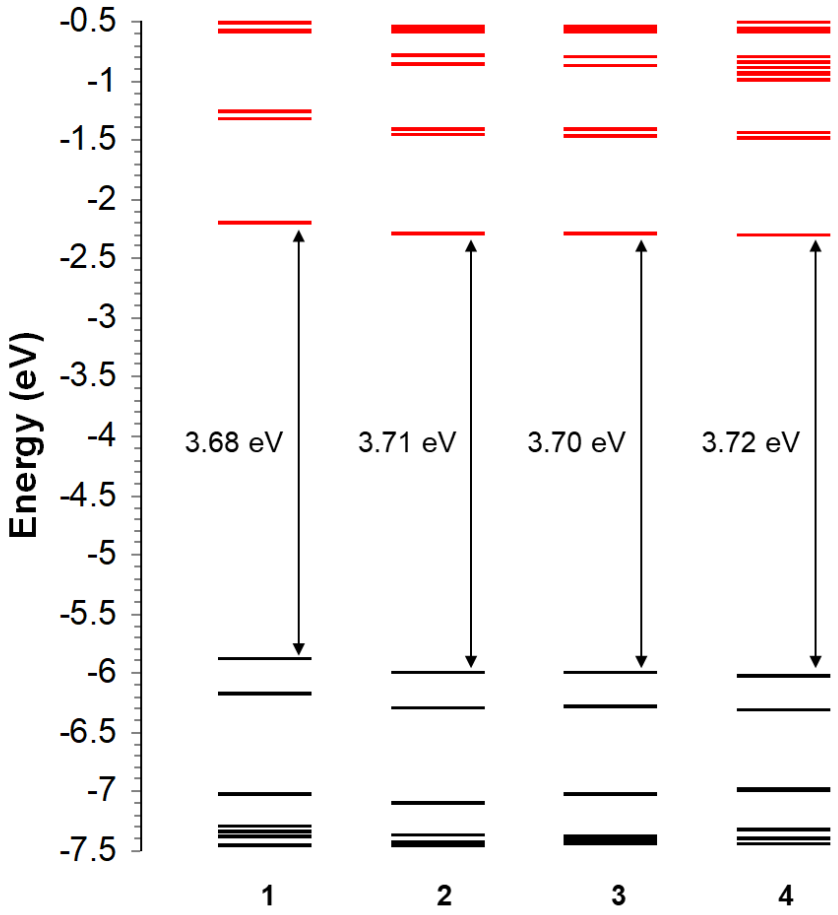


**Figure III.10.** Calculated molecular orbital diagrams for **1-4** and their HOMO-LUMO energy gaps (black = occupied, red = unoccupied).

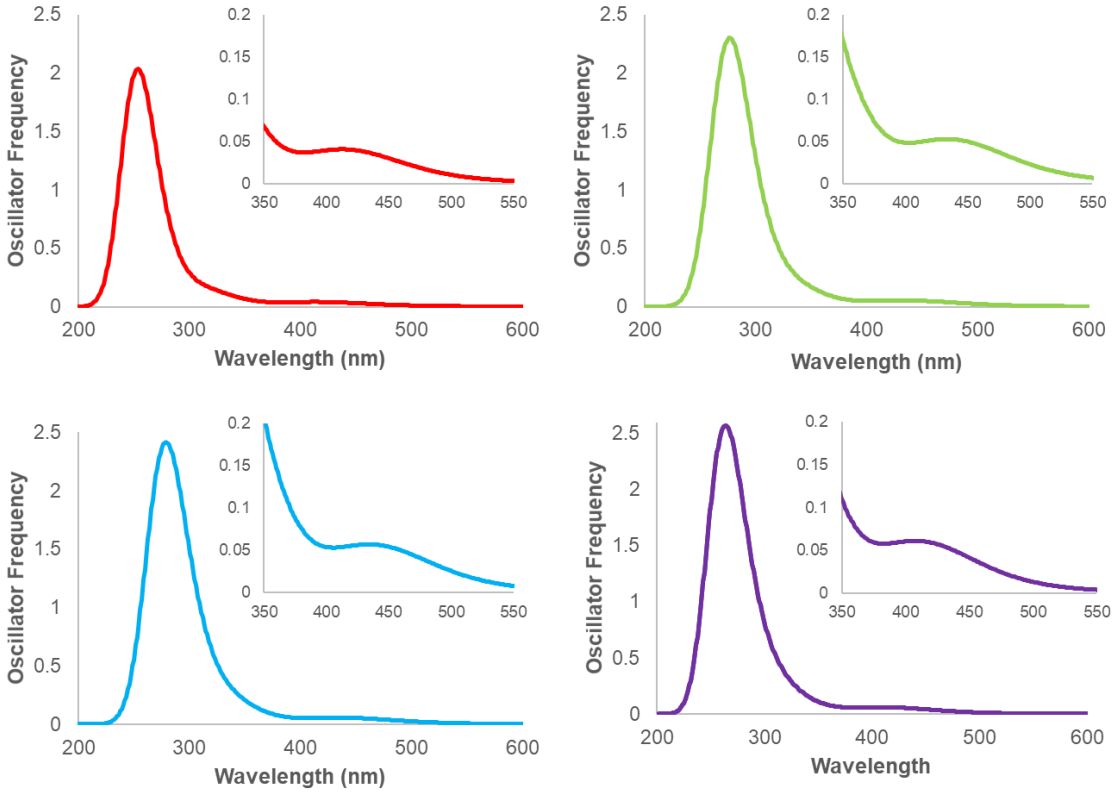


**Figure III.11.** Calculated electronic absorption spectra (PCM solvation model, solvent = $CH_3CN$) for **1-4.**

The orbital compositions for the HOMO-3 to the LUMO+3 are visualized in Figure III.12 and listed for complexes **2-4** in Table III.4. The HOMOs for **1-4** are all primarily formamidinate (~ 70%) in character with some rhodium contribution (~ 27%). The formamidinate contribution is higher for the lower energy orbitals and is also increased across the series from **1** to **4**. Conversely, the rhodium contribution decreases across the series from **1** to **4.** The LUMO is the $Rh_2(\sigma^*)$ orbital for all four complexes, and is primarily rhodium in character (~ 67%) with small contributions from the formamidinate ligands and the axial acetonitrile ligands (~ 15%). The next two lower lying orbitals, the LUMO+1 and the LUMO+2 have approximately 45%, 35% and 20% contributions from

the rhodium, formamidinate and equatorial acetonitrile ligands, respectively. The rhodium contribution slightly decreases in going from **1** to **4**, the formamidinate contribution slightly increases and the contribution from the equatorial ligands is consistent across the series.

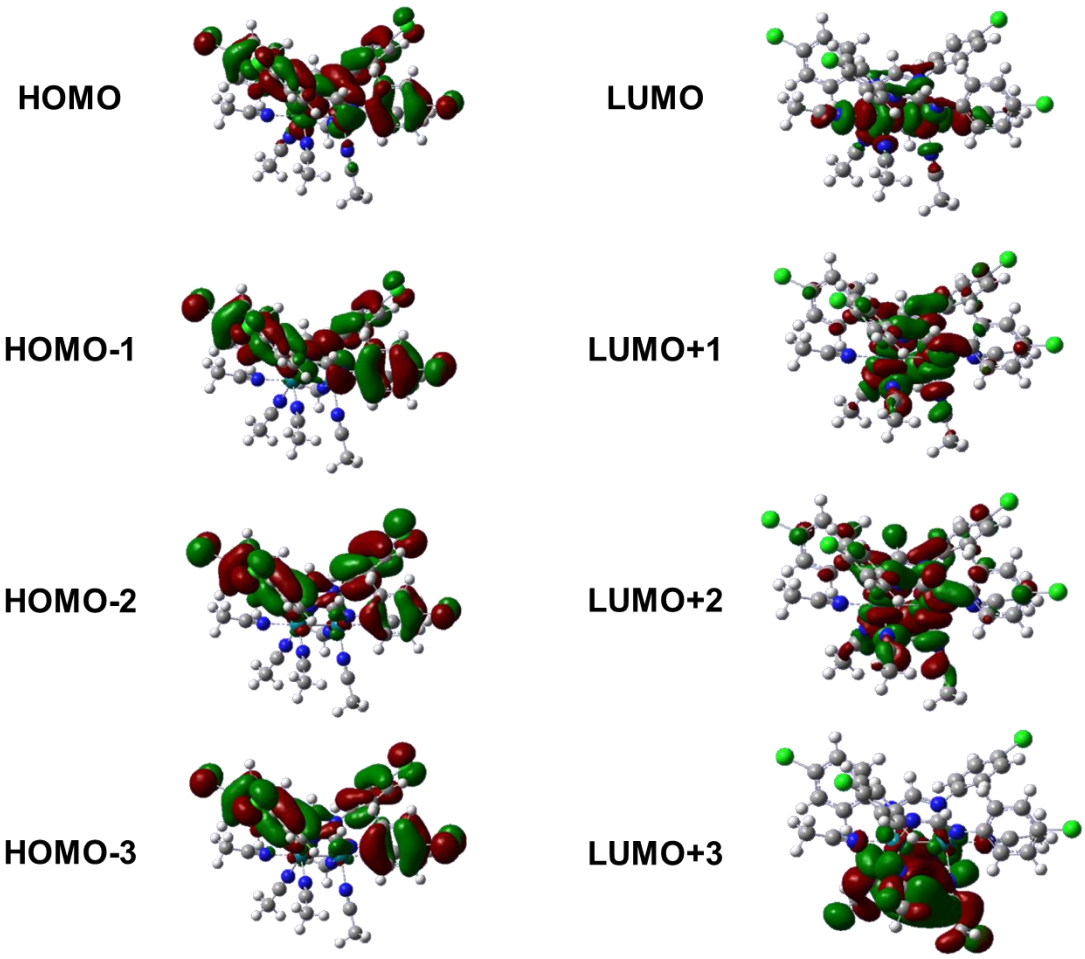


**Figure III.12.** Calculated representative frontier orbitals for complexes of the type $[Rh_2(X\text{-}Form)_2(MeCN)_2]^{2+}$, visualizing the orbitals of **2.** (isovalues = 0.02).

**Table III.5** Calculated fragment contributions to the frontier orbitals of **2-4.** Form refers to the bridging formamidinate ligand.

| Orbital | 2 | 3 | 4 |
|---|---|---|---|
| **HOMO–3** | 17% Rh, 81% Form | 14% Rh, 84% Form | 17% Rh, 82% Form |
| **HOMO–2** | 6% Rh, 92% Form | 5% Rh, 94% Form | 5% Rh, 94% Form |
| **HOMO–1** | 5% Rh, 93% Form | 4% Rh, 94% Form | 4% Rh, 94% Form |
| **HOMO** | 27% Rh, 70% Form | 27% Rh, 71% Form | 27% Rh, 71% Form |
| **LUMO** | 66% Rh, 12% Form, 7% $CH_3CN_{eq}$, 15% $CH_3CN_{ax}$ | 66% Rh, 12% Form, 7% $CH_3CN_{eq}$, 15% $CH_3CN_{ax}$ | 66% Rh, 12% Form, 7% $CH_3CN_{eq}$, 15% $CH_3CN_{ax}$ |
| **LUMO+1** | 42% Rh, 38% Form, 20% $CH_3CN_{eq}$ | 41% Rh, 38% Form, 20% $CH_3CN_{eq}$ | 41% Rh, 38% Form, 20% $CH_3CN_{eq}$ |
| **LUMO+2** | 43% Rh, 37% Form, 20% $CH_3CN_{eq}$ | 43% Rh, 37% Form, 19% $CH_3CN_{eq}$ | 44% Rh, 37% Form, 19% $CH_3CN_{eq}$ |
| **LUMO+3** | 18% Rh, 77% Form | 15% Rh, 80% Form | 30% Rh, 69% Form |

[a]Only contributions higher than 5% are listed.

From the TD-DFT calculations, it was determined that the electronic transitions for **1-4** are consistent with those typical for formamidinate bridged partially solvated complexes. The lowest energy transitions at approximately 500 nm were determined to be a ligand to metal HOMO → LUMO transition. The next higher energy transitions are primarily ligand to metal-ligand in character. The transitions near 250 nm are determined to have both metal and ligand character. It is of note that the lower energy transitions populate the antibonding orbital interaction of the $Rh_2$ core with the equatorial acetonitrile

ligands. Irradiation of the complex weakens the Rh-N(eq) bond and results in faster ligand dissociation, which is consistent with these calculated results.

Using computational methods, the bond dissociation energy of the equatorial acetonitrile ligands was calculated in both the gas phase and with acetonitrile as the solvent. The bond dissociation energies for **1**-**4** were determined to be 27.87, 28.43, 28.49 and 28.63 kcal/mol, respectively. These are within range of previously determined dissociation energies for other rhodium complexes. While there does appear to be a small increase in the BDE across the series which is consistent with the crystallographic bond length observations and ligand dissociation trends, this difference is within the error of the computational methods used.

**Conclusions**

The work in this chapter explores the functionalization of the bridging formamidinate ligands, and systematic investigation of the effect of halogen substation on the photophysical and cytotoxicity of dirhodium complexes are discussed. The bridging ligands F-Form, Cl-Form, Br-Form and I-Form were used in the synthesis of series of partial paddlewheel dirhodium cationic complexes of the type $[Rh_2(X\text{-Form})_2(MeCN)_2]^{2+}$ where X-Form = N,N'-bis(*p*-X-phenyl)formamidinate) and X= F, Cl, Br and I. Single crystal X-ray diffraction, DFT calculations and time-dependent NMR studies elucidated both similarities and differences in the lability of solvent ligands and trends in electronic structure. TD-NMR studies indicate faster ligand dissociation upon irradiation, and slower ligand dissociation as halogen electronegativity decreases. There is a small red shift with increasing halogen size, and visible transitions are consistently metal-to-metal-ligand

charge transfer in character; population of the orbitals antibonding in character with respect to the metal and equatorial acetonitrile upon irradiation is consistent with the observed NMR results. Structurally, a decrease in average Rh-N bond distances is observed as the halogen electronegativity decreases. These structural and kinetic trends are due to both the *trans* influence and *trans* effect of the bridging formamidinate ligands. The partially solvated complexes are commonly used as starting materials for other dirhodium complexes and, since they have not recently been systematically studied in the Dunbar group, it was of interest to investigate these complexes as a series.

# CHAPTER IV

# DIRHODIUM FORMAMIDINATE COMPLEXES WITH PANCHROMIC ABSORPTION: APPLICATIONS FOR SOLAR CELL SENSITIZATION

## Introduction

Rising energy demands in the United States and worldwide have necessitated the development of technologies to harness power from renewable sources. The use of sunlight to drive chemical processes and generate energy are highly promising and impactful areas of investigation.[60, 116-120] Currently, the highest experimentally measured solar energy conversion efficiencies are upwards of 45%, for example, the multijunction GaInP/GaAs; GaInAsP/GaInA cell in a concentrator photovoltaic system.[65] As these systems are extremely cost prohibitive, they are not suitable for residential scale uses, but the more traditional silicon p-n junction solar cells have lower conversion efficiencies between 15-20%.[65, 66]

Dye-sensitized solar cells (DSSCs) are a low cost, highly tunable, flexible and durable alternative to traditional solar cells.[69-73] Modern DSSCs are composed of two transparent conducting oxide (TCO) electrodes, with a dye-coated mesoporous semiconductor layer sandwiched between them, a platinum counter-electrode layer, and an organic redox electrolyte.[70] Upon photoexcitation of the dye, an electron or hole can be injected into the semiconductor material. Current DSSCs are reported to have power conversion efficiencies of 13.6% in the case of organic dyes, and lower for metal-based dyes; specifically 11.8% and 13.0% for ruthenium and zinc porphyrin sensitizers,

respectively. These values are lower than those of traditional solar cells, a situation that has prompted intensive efforts to develop more effective sensitizers to increase the PCE of these systems.

The design and selection of the photosensitizer is very important for the performance of a DSSC; it should possess properties such as chemical and thermal stability, strong absorption in the visible and near-IR region, and HOMO/LUMO energy levels that allow charge transfer from the excited state of the compound to the semiconductor. These compounds must also have peripheral anchoring groups, typically carboxylates or phosphates, so that they can adsorb strongly to the semiconductor surface.[70, 81, 121]

Many classes of compounds have been investigated for their use in DSSCs. Among organic dyes, porphyrin derivatives have shown promise due to their fast electron injection kinetics and typical strong absorption features in the visible region. A drawback, however, is that they are known to aggregate on the surface of $TiO_2$ and self-quench the electron injection process.[122] Other organic compounds of the D-π-A structural type are also of great interest in the field. Such a design allows for photoinduced charge separation, where the HOMO is localized primarily on the donor moiety (D) which, upon irradiation shifts electron density through the π-conjugated linker to the acceptor moiety (A).[79, 121]

Various inorganic coordination compounds have been investigated as light absorbers for DSSC applications as well. These include compounds containing metals such as rhenium, iron, copper, osmium and ruthenium, among others.[81, 123-126] In fact, octahedral ruthenium complexes with various bipyridine type ligands are the most

extensively studied of the metal based dyes.[101] The current benchmarks for DSSCs are the ruthenium coordination complexes [Ru(4,4',4''-$(COOH)_3$-terpy)$(NCS)_3$] and [Ru$(dcbpyH_2)_2(NCS)_2$], which are known as "black dye" and "red dye," or N3 and N749, respectively.[68, 82] However, these types of complexes are not capable of harnessing the full solar spectrum. For example, the N3 dye has an absorption maximum at 534 nm in ethanol ($\varepsilon = 1.42 \times 10^4$ M−1 cm−1). Furthermore, most of the reported dyes are designed only for n-type sensitization and adsorption onto $TiO_2$.

The design and synthesis of dyes that are suitable for hole injection is a relatively underexplored area in the development of DSSCs.[127] In theory, tandem p-type and n-type DSSCs have a predicted efficiency increase from 33% to 44% as compared to tradition n-type systems. Currently, organic dyes based on Boron-dipyrromethene (BODIPY), phthalocyanines or porphyrins, among other moieties, are the most widely investigated.[128-130] Similar to the drawbacks presented by these classes of compounds in n-type sensitization, poor light absorption in the near IR region, narrow absorption profiles, and charge recombination are all issues that must be overcome.

At the time of this study, rhodium-based photosensitizers had not been investigated as potential n-type or p-type sensitizers in the construction of DSSCs. Cationic dirhodium (II,II) complexes meet a number of the criteria required for a good DSSC light absorber and can potentially overcome some of the obstacles presented by current organic and inorganic dyes. Recent work from the Dunbar and Turro group highlights a new class of dirhodium complexes featuring tridendate, axially blocking electron accepting ligands.[83, 84] These complexes of the type *cis*-$[Rh_2(DTolF)_2(\mu\text{-}L)_2][BF_4]_2$ where L = 2-(pyridin-2-yl)-

1,8-naphthyridine (pynp), 2-(quinolin-2-yl)-1,8-naphthyridine (qnnp), and 2-(1,8-naphthyridin-2-yl)quinoxaline (qxnp) absorb strongly from the UV to the near IR region, and exhibit promising excited state redox properties for sensitizing DSSC semiconductors.[83] Specifically, the compound *cis*-$[Rh_2(DTolF)_2(\mu\text{-}L)_2][BF_4]_2$ is able to reduce methyl viologen, indicating sufficient driving force for electron injection into $TiO_2$ n-type semiconductors, and is also able to generate the *p*-phenylenediamine radical cation, an indication of potential for hole transfer to p-type NiO.[83]

The present study involves the design and synthesis of new cationic dirhodium complexes with anchoring groups for the use of dyes in DSSC fabrication. These compounds are $[Rh_2(DTolF)_2(\mu\text{-}L)_2][BF_4]_2$, where L= ethyl 2-(pyridin-2-yl)-1,8-naphthyridine-4-carboxylate (2COOEt-pynp), **1**), ethyl 2-(1,8-naphthyridin-2-yl)isonicotinate (4COOEt-pynp, **2**), and $[Rh_2(COOEt\text{-}Form)_2(\mu\text{-}L)_2][BF_4]_2$ where COOEt-Form = N,N'-bis(4-ethoxycarbonylphenyl)-N'(benzylformamidinate) and (μ-L) = pynp (**7)**, qnnp (**8)** and qxnp (**9)**. These new molecules are inspired by the DTolF bridged $Rh_2$ complexes with axially blocking naphthyridine based ligand and featureL panchromic absorption reaching the near-IR, long lived excited states, are air and water stable and highly soluble in aqueous and organic solvents.[83, 131] Computational studies indicate appropriate HOMO/LUMO energy gaps and as well as directional charge transfer. Compounds **1** and **2** bear functionalization on the electron accepting moiety of the molecule, and are designed for n-type sensitization whereas **7**, **8** and **9** bear functionalization on the electron donating formamidinate bridging ligand and are intended for hole transfer and p-type sensitization (Figure IV.1, Figure IV.2) . **1**, **2**, **7**, **8** and **9** are

reported in this study with ester functionalized ligands which are poised to be hydrolyzed *in situ* to the carboxylate analogue for DSSC fabrication. The potential of these complexes for use as DSSC sensitizers is discussed herein.

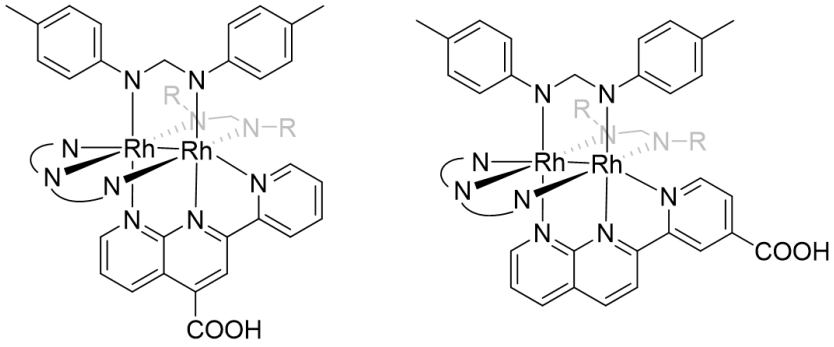


1 2

**Figure IV.1** Schematic representations of the molecular structures of the proposed complexes for n-type sensitization.

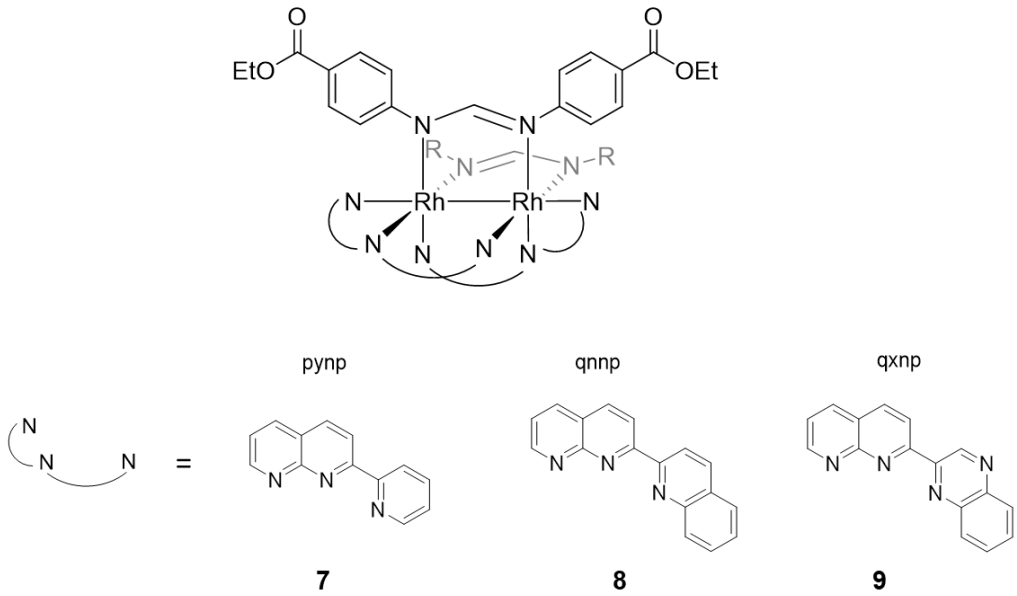


7 8 9

**Figure IV.2** Schematic representations of the molecular structures of the proposed complexes for p-type sensitization.

## Experimental Procedures

*Materials***.**

The naphthyridine ligands qxnp, qnnp, pynp, 4COOEt-pynp and 2COOEt-pynp were synthesized according to literature procedures.[83, 132, 133] Starting materials were purchased from Ark Pharm and used without further purification. The protonated form of the bridging ligand N,N'-di(*p*-tolyl)formamidine (HDTolF) was synthesized from triethyl orthoformate and p-toluidine following reported procedure,[90] and the bridging ligand N,N'-bis(4-ethoxycarbonylphenyl)-N'(benzylformamidine) (COOEt-FormH) was prepared from triethyl orthoformate and benzocaine following modified literature literature procedure. Triethyl orthoformate was used as purchased from TCI, and the anilines were purchased from Alfa Aesar. To synthesize the dirhodium partially solvated complex starting materials, $[RhCl(COD)]_2$ (COD = 1,5-cyclooctadiene) from Pressure Chemicals was used without further purification. The synthesis of *cis*-$[Rh_2(DTolF)_2(CH_3CN)_6][BF_4]_2$ was done following a reported procedure,[115] and the synthesis of *cis*-$[Rh_2(COOEt\text{-}Form)_2(CH_3CN)_6][BF_4]_2$ was adapted from literature procedure.[83] Acetonitrile was dried over dried over 3Å molecular sieves and distilled under a $N_2$ atmosphere, dichloromethane was dried over $P_2O_5$ and distilled under a $N_2$ atmosphere, and diethyl ether was used as received. All reactions were performed under a $N_2$ atmosphere using standard Schlenk line and glove box techniques, while work-up and isolation of products was performed in air unless otherwise noted.

***cis*-$[Rh_2(DTolF)_2(2COOEtpynp)_2][BF_4]_2$ (1):** Quantities of *cis*-$[Rh_2(DTolF)_2(CH_3CN)_6][BF_4]_2$ (99.3 mg, 0.0951 mmol) and the ligand 2COOEtpynp

were suspended in 25 mL of dry $CH_3CN$. The reaction mixture was heated to reflux for 24 h, resulting in a dark green solution. After cooling to room temperature, the solvent was evaporated to approximately 5 mL under reduced pressure, and diethyl ether was added to precipitate the product. The dark green powder was collected by vacuum filtration on a fine frit and washed with copious amounts of diethyl ether. %Yield: 93.2 % (122.5 mg, 0.0886 mmol). $^1$H-NMR (500 MHz, $CD_3CN$) δ 9.19 (dd, J = 8.6, 1.7 Hz, 2H), 8.89 (s, 2H), 8.72 (dd, J = 5.3, 1.6 Hz, 2H), 8.53 (d, J = 8.3 Hz, 2H), 8.11 (ddd, J = 8.0, 7.4, 2.0 Hz, 2H), 7.57 (dd, J = 8.6, 5.4 Hz, 2H), 7.49 (t, J = 3.5 Hz, 2H), 7.37 – 7.31 (m, 4H), 7.22 (d, J = 7.9 Hz, 4H), 6.81 (d, J = 8.3 Hz, 4H), 6.55 (d, J = 7.8 Hz, 4H), 6.25 (d, J = 7.8 Hz, 4H), 4.55 (q, J = 7.0 Hz, 4H), 2.40 (s, 6H), 2.09 (s, 6H), 1.47 (t, J = 7.1 Hz, 6H).

***cis*-[Rh$_2$(DTolF)$_2$(4COOEtpynp)$_2$][BF$_4$]$_2$ (2):** A sample of *cis*-[Rh$_2$(DTolF)$_2$(CH$_3$CN)$_6$][BF$_4$]$_2$ (99.2 mg, 0.0954 mmol) was dissolved in 20 ml dry $CH_3CN$ with the ligand 4COOEtpynp and refluxed for 24 h. The dark green solution was cooled to room temperature and concentrated to ~ 5 mL under vacuum. The dark green product was precipitated by the addition of 30 mL of diethyl ether to the concentrated solution. The product was collected on a fine frit and washed with diethyl ether. %Yield: 89.2 % (117.7 mg, 0.0851 mmol). $^1$H-NMR (500 MHz, $CD_3CN$) δ 8.80 (d, J = 1.1 Hz, 1H), 8.73 – 8.69 (m, 2H), 8.65 (d, J = 8.8 Hz, 1H), 8.55 (dd, J = 8.2, 1.6 Hz, 1H), 7.77 (dd, J = 5.4, 1.6 Hz, 1H), 7.53 (dd, J = 8.1, 5.4 Hz, 1H), 7.50 (dd, J = 6.3, 3.3 Hz, 2H), 7.26 (d, J = 7.9 Hz, 2H), 6.85 (d, J = 8.2 Hz, 2H), 6.52 (d, J = 7.8 Hz, 2H), 6.23 (d, J = 7.4 Hz, 2H), 4.53 (qd, J = 7.1, 1.6 Hz, 2H), 2.44 (s, 3H), 2.06 (s, 3H), 1.50 (t, J = 7.1 Hz, 3H).

***cis*-[Rh$_2$(DTolF)$_2$(2COOHpynp)$_2$][BF$_4$]$_2$ (3):** To a large vial, a quantitiy of **1** (21.0 mg mmol) was dissolved in a small amount of THF and TBAOH (0.25 mL, 40% v/v in MeOH) was added, resulting in an immediate color change from green to brown. The mixture was stirred for 30 minutes under ambient conditions at room temperature before being quenched with water. The resulting dark green solution was concentrated under vacuum and glacial acetic acid was added to dissolve any precipitate. The product was extracted with DCM and dried over $MgSO_4$. Following the removal of solvent, the green product was attempted to be purified by redissolving in DCM and precipitation with the addition of diethyl ether.

***cis*-[Rh$_2$(DTolF)$_2$(4COOHpynp)$_2$][BF$_4$]$_2$ (4):** A sample of **2** (22.0 mg mmol) was suspended in a small amount of THF. TBAOH (0.25 mL, 40% v/v in MeOH) was added, resulting in the immediate formation of a brown solution. The mixture was stirred for 30 minutes under ambient conditions at room temperature before being quenched with water. The resulting dark green solution was concentrated under vacuum and acidified with glacial acetic acid. The product was extracted with DCM and dried over $MgSO_4$. Following the removal of solvent, the green product was redissolved in 50:50 DCM:MeCN and precipitated with diethyl ether.

**[Rh(COOEt-Form)(COD)]$_2$ (5):** Quantities of COOEt-FormH were added to a flask with KO$^t$Bu and suspended in 50 mL of dry toluene. In a separate flask, [RhCl(COD)]$_2$ was dissolved in 25 mL of dry toluene and added dropwise to the suspension, resulting in a slow color from pale yellow to orange. The mixture was stirred at room temperature for 4 days, after which time the solvent was removed under reduced pressure. The solid was

redissolved in 5 mL of toluene and 50 mL of hexanes were added to precipitate a bright orange powder which was collected on a fine frit, dried under vacuum, and used without further purification or characterization.

***cis*-[Rh$_2$(COOEt-Form)$_2$(MeCN)$_6$][PF$_6$]$_2$ (6):** An amount of [Fe($C_5H_5$)$_2$]$PF_6$] (414.7mg, 1.25 mmol) was dissolved in 15 mL of dry DCM and added dropwise to a solution of **5** (658.3 mg, 0.598 mmol) suspended in 30 mL of dry acetonitrile. The mixture was stirred at room temperature for 3 days, and the resulting brown-green solution was concentrated under reduced pressure. Addition of 30 mL of diethyl ether resulted in the precipitation of a light brown powder, which was obtained by vacuum filtration over a fine frit. The product was washed with diethyl ether and dried under vacuum before purifying by vapour diffusion of diethy ether into a concentrated acetonitrile solution. Large red x-ray diffraction quality crystals were obtained. % Yield 48.9% (413 mg, 0.029 mmol). ESI-MS: m/z 524.092. [Rh2(FormCOOEt)$_2$(MeCN)]$^{2+}$). 1H-NMR ($CD_3CN$) (ppm): 8.03 (m, 8H), 7.36 (m, 8H), 4.42 (m, 8H), 1.44 (m, 12H)

***cis*-[Rh$_2$(COOEt-Form)$_2$(pynp)$_2$][PF$_6$]$_2$ (7):** A quantity of **6** (46.4 mg, 0.033 mmol) was dissolved in 20 mL of dry acetonitrile with pynp (14.3 mg, 0.069 mmol). The reaction mixture was refluxed with stirring for 24 h to give a dark blue solution, before cooling to room temperature. The solution was evaporated to dryness under vacuum, and a minimal amount of acetonitrile was added to redissolve the blue residue. The product was precipitated with the addition of 30 mL of diethyl ether, and the dark blue solid was collected on a fine frit. %Yield: 90.4% (48.1 mg, 0.029 mmol). ESI-MS: m/z 622.078 (99%).[Rh2(FormCOOEt)$_2$(MeCN)]$^{2+}$). 1H-NMR ($CD_3CN$) (ppm): 8.78 (m, 2H), 8.68 (s,

4H), 8.56 (dd , 4H), 7.67 (d, 2H), 7.56 (t, 2H) 7.42 (d, 4H), 7.25 (m, 2H) 7.01 (d, 2H) 6.56 (d, 2H), 4.28 (m, 8H), 1.40 (t, 12H).

***cis*-[Rh$_2$(COOEt-Form)$_2$(qnnp)$_2$][PF$_6$]$_2$ (8):** In a Schlenk flask, amounts of **6** (36.6 mg, 0.026 mmol), qnnp (13.7 mg, 0.053 mmol) and 20 mL of dry acetonitrile were stirred and refluxed for 24 h. The dark blue-green solution was cooled to room temperature before removing solvent under reduced pressure. A small amount of acetonitrile was added to redissolve the residue and addition of 30 mL of diethyl ether precipitated the dark blue-green product. The suspension was filtered through a fine frit and the product was washed with diethyl ether. 79.2% (35.5 mg, 0.021 mmol). $^1$H NMR (CD3CN) (ppm): 9.16 (m, 2H), 8.89 (d, 2H), 8.78 (d, 4H), 8.49 (s, 4H), 7.96 (d, 4H), 7.72 (dd, 4H), 7.66 (dd, 2H), 7.50 (t, 2H), 7.22 (d, 2H), 6.96 (d, 4H), 6.84 (t, 2H), 6.53 (d, 4H), 6.21 (d, 4H) 4.40 (q, 8H), 1.41 (t, 12H).

***cis*-[Rh$_2$(COOEt-Form)$_2$(qxnp)$_2$][PF$_6$]$_2$ (9):** A sample of **6** (65.2 mg, 0.047 mmol) was added to 20 mL of dry acetonitrile along with qxnp ligand (24.4 mg, 0.094 mmol). The reaction was stirred at reflux for 24 h and then cooled to room temperature. The dark blue-green solution was dried under vacuum before being redissolved in a small amount of acetonitrile. 30 mL of diethyl ether was added and a dark blue-green solid was precipitated. The product was collected by vacuum filtration with a fine frit and washed with diethyl ether. 88.9% (70.7 mg, mmol). 1H NMR (CD3CN) (ppm): 9.89 (s, 2H), 8.95 (m, 6H), 8.78 (d, 2H), 7.97 (d, 4H), 7.88 (d, 2H), 7.69 (m, 6H), 6.94 (m, 8H), 6.59 (d, 4H), 6.27 (d, 4H), 4.38 (q, 8H), 1.36 (m, 12H)

*Instrumentation and Methods.*

$^{1}$H-NMR spectra were collected on an Inova 500 MHz spectrometer. The chemical shifts were referenced to the peak of the residual $CD_3CN$-$d_3$ deuterated solvent signal at 1.94 ppm[92], and are reported in ppm. Electronic spectroscopy was performed on a Shimadzu UV-1601PC spectrophotometer using 1 x 1 cm quartz cuvettes, and absorption spectra were obtained in triplicate. Electrospray ionization mass spectra (ESI-MS) were collected at the Laboratory for Biological Mass Spectrometry at Texas A&M University using a PE Sciex (Concord, Ontario, Canada) API Qstar Pulsar with an Ionwerks time-to-digital converter, TDCx4, for data recording. Electrochemical measurements for **1**, **2**, **6**, **7** and **8** ($1 \times 10^{-3}$ M) were recorded under nitrogen in dry acetonitrile with 0.1 M [n-$Bu_4N$][$PF_6$] as the supporting electrolyte using a CH Instruments electrochemical analyzer model CH1620A. A three-electrode cell was used with a glassy carbon disc working electrode, a Pt wire counter electrode, and a Ag/AgCl reference electrode standardized to ferrocene ($E_{1/2}$ = +0.55 V vs Ag/ AgCl).

Single crystals of **1**, **2**, **5**, **6**, **7** and **8** were selected under ambient conditions from oil using a MiTeGen microloop. The X-ray data set was collected on a Bruker CCD APEX diffractometer with graphite monochromated Mo Kα radiation (λ = 0.71073 Å). For the compounds**,** the initial unit cell was determined using SAINT from a set of three ω-scans consisting of 0.5° frames and a sweep width of 15°. APEX3 was used to determine the data collection to collect all independent reflections to a resolution of at least 0.82 Å. The data were corrected for absorption using SADABS,[93] and the space group was determined from analysis of the systematic absences and E-statistics using XPREP. The structures

were solved using the intrinsic phasing routine in SHELXT or by direct methods implemented in SHELXS. The non-hydrogen atoms were located from Fourier difference maps by least-squares refinement of the structure using SHELXL-2014.[94] All non-hydrogen atoms were refined anisotropically and hydrogen atoms were placed in calculated positions and refined with thermal parameters constrained to their parent atom. DIAMOND was used to generate the molecular graphics.

Density Functional Theory (DFT) calculations for molecular and electronic structures were performed using the Gaussian (16) program package.[95] The B3LYP correlation and exchange functional was used with the with the Stuttgart RSC 1997 Electron Core Potential (ECP) basis set for the Rh and I atoms and the 6-31G(d') basis set for the C, N, F, Cl, Br and H atoms. The starting geometries for the gas-phase optimizations were taken from the crystal structure of the complexes, excluding the counter ions and solvent molecules. Time-Dependent Density Functional Theory (TD-DFT) calculations were performed using the polarized continuum model (PCM)[101] with acetonitrile as the solvent. From the optimized singlet ground state geometry, the first sixty lowest singlet-to-singlet excited states were calculated. The graphic software 'Gaussview' (ref) was used to plot the molecular orbitals with iso-value of 0.03. the Chemissian Visualization Computer Program was used to analyze molecular orbital contributions.

## Results and Discussion

*Synthesis.*

The naphthyridine type ligands were synthesized via Friedlander condensation reactions. The ligands 2-(2-pyridinyl)-1,8-naphthyridine (pynp), 2-(Quinoline-2-yl)-1,8-naphthyridine (qnnp), and 2-(1,8-naphthyridine- 2-yl)quinoxaline (qxnp) were synthesized from reported procedures.[134] The ligands 2-(pyridin-2-yl)-1,8-naphthyridine-4-carboxylic acid (pynp-4COOH), ethyl 2-(pyridin-2-yl)-1,8-naphthyridine-4-carboxylate (pynp-4COOEt), 2-(1,8-naphthyridin-2-yl)isonicotinic acid (pynp-2COOEt) ethyl 2-(1,8-naphthyridin-2-yl)isonicotinate (pynp-2COOEt) were synthesized from the respective methyl analogue, which was made following the Friedlander condensation literature procedure. Oxidation with potassium dichromate yielded the carboxylic acid functionalized ligands which were converted to the ester analogue by a transesterification reaction in ethanol (Figure IV.3).

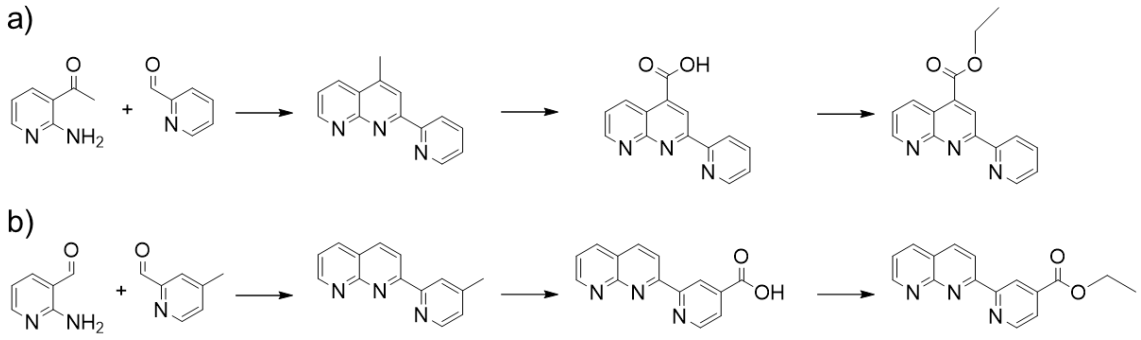


**Figure IV.3** Synthetic scheme for π-accepting and axially blocking ligands with anchoring groups (a) 2COOEtpynp and (b) 4COOEtpynp.

Compounds **1** and **2** were prepared by reacting stoichiometric quantities of the ester functionalized ligand with *cis*-$[Rh_2(DTolF)_2(CH_3CN)_6][BF_4]_2$ in refluxing

acetonitrile. The syntheses of compounds **3** and **4** were originally attempted by following the procedure used for **1** and **2,** which was adapted from literature and similar to the synthesis of other *cis*-$[Rh_2(DTolF)_2(N\text{-}N)_2][BF_4]_2$ complexes in which the coordinating solvent ligands are replaced by nitrogen containing multi-dentate acceptor ligands. X-ray diffraction experiments indicated the successful synthesis of the desired products, but, due to ease of purification and characterization, **3** and **4** were more easily obtained and in higher yields by the hydrolysis of **1** and **2,** respectively, in the presence of tetrabutylammonium hydroxide and purified by liquid-liquid extraction (Figure IV.4)

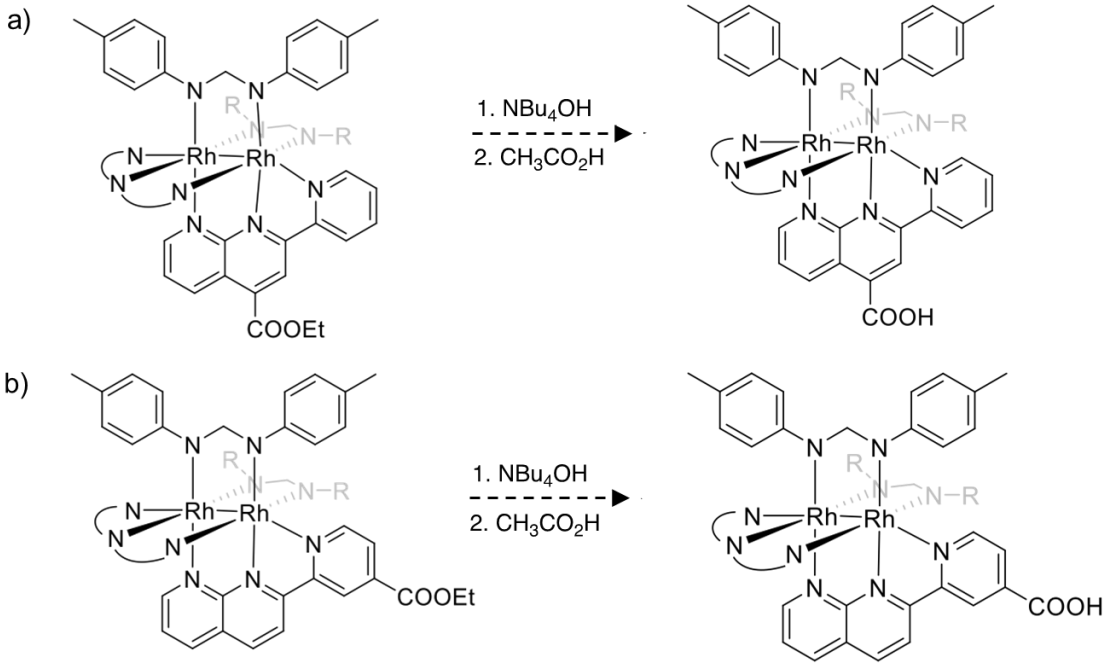


**Figure IV.4** Synthetic scheme for the hydrolysis of (a) from **1** to **3** and (b) from **2** to **4**.

Compound **6** was synthesized by adapting the procedure for the synthesis of other dirhodium partially solvated complexes. The ligand, N,N'-bis(4-ethoxycarbonylphenyl)-

N'(benzylformamidine) was deprotonated with potassium tert-butoxide and reacted with $[RhCl(COD)]_2$ to yield the dinuclear compound $[Rh(COOEt\text{-}Form)(COD)]_2$ **(5)**. It should be noted that the typical reaction with excess silver tetrafluoroborate resulted in a number of Rh(III) side products, therefore the milder oxidizing agent ferrocenium hexafluorophosphate was used in this preparation. Compounds **7-9** were synthesized by adaptation of a literature procedure[83] which involved reacting a small excess of the respective naphthyridine ligand with **6** in refluxing acetonitrile for 24 hours. Concentration of the solvent under vacuum and subsequent addition of diethyl ether precipitated the desired compounds as dark green solids. The purity of complexes **1**, **2**, and **6-9** are supported by NMR (Figure IV.5 – IV. 9). and ESI experiments.

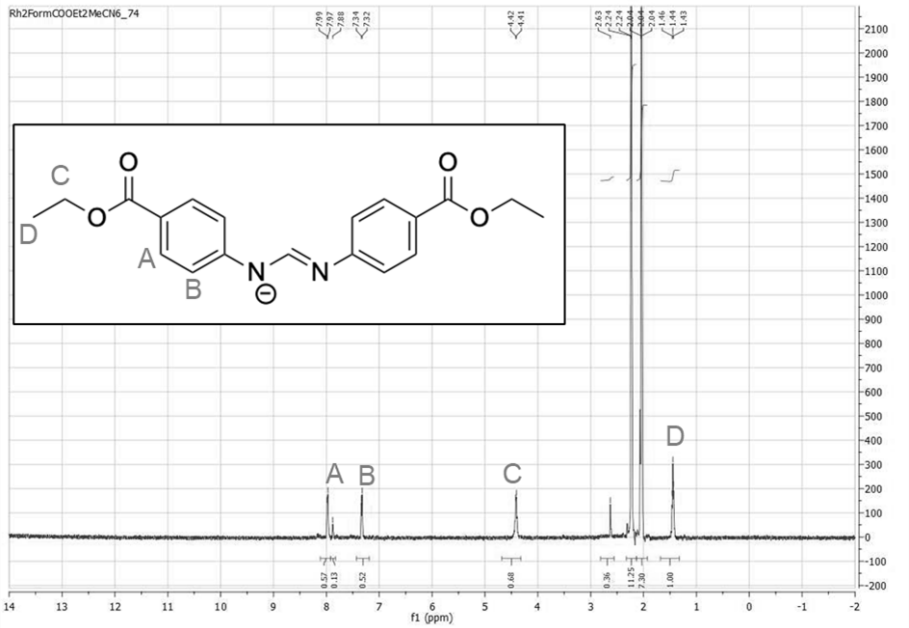


**Figure IV.5** Full $^1$H-NMR spectrum of **6** in $CD_3CN$ with ligand peak assignments.

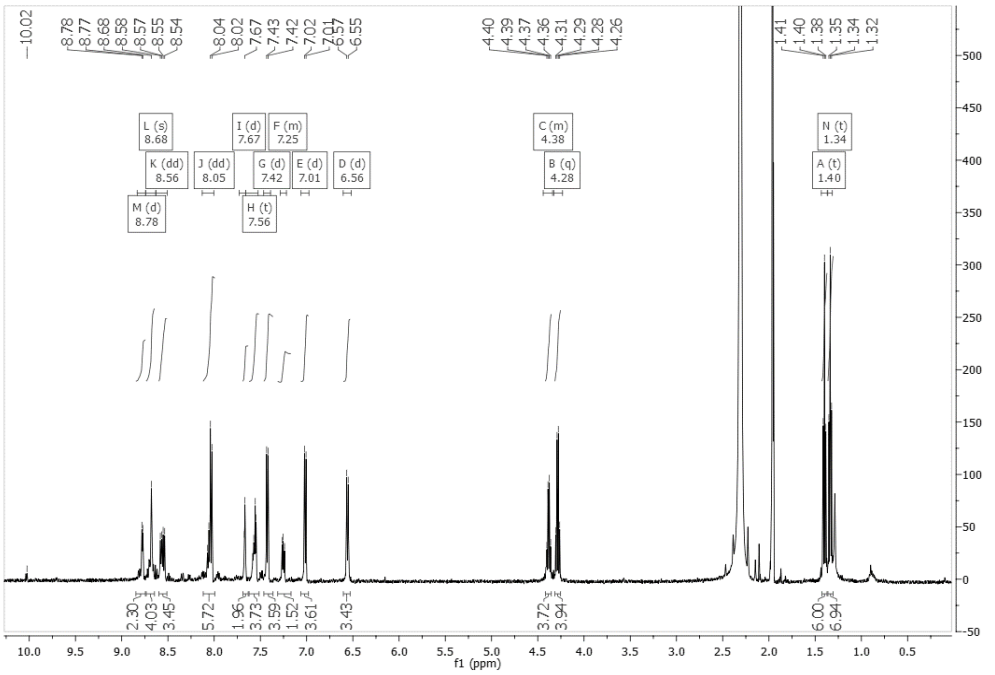


**Figure IV.6** Full $^{1}$H-NMR spectrum of **7** in $CD_3CN$. Residual solvent peaks (ppm): 1.94 (acetonitrile); 2.13 (water).

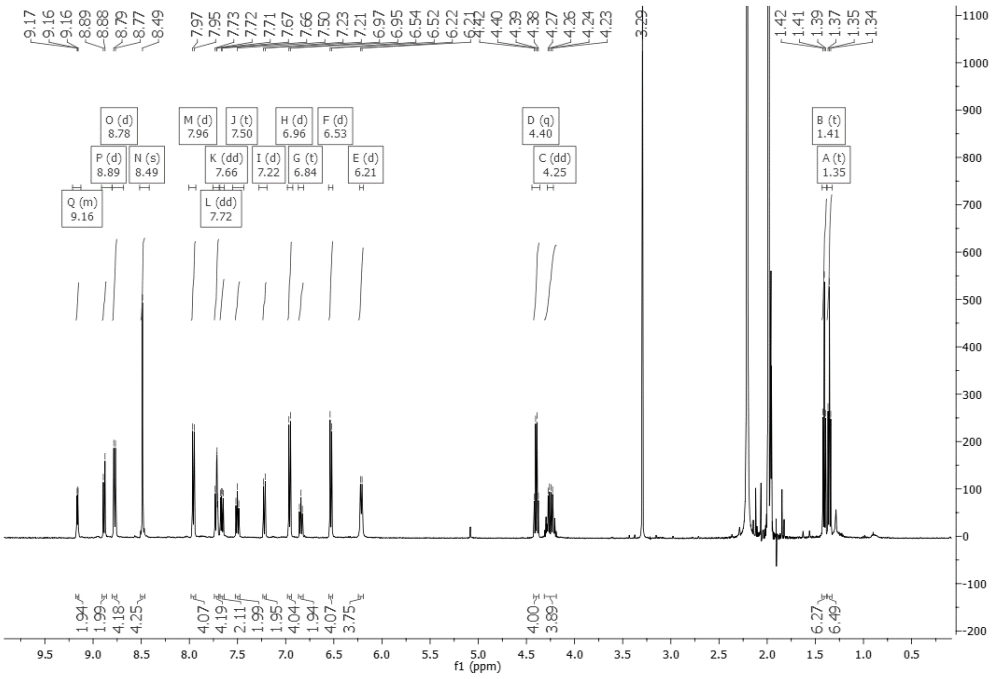


**Figure IV.7** Full $^{1}$H-NMR spectrum of **8** in $CD_3CN$. Residual solvent peaks (ppm): 1.94 (acetonitrile); 2.13 (water).

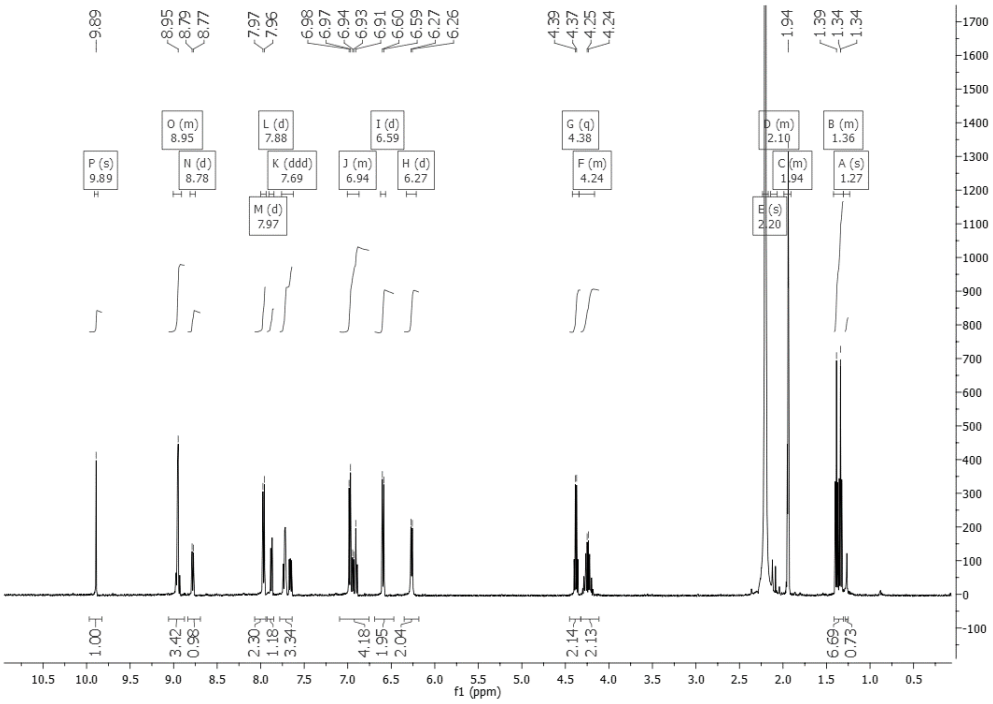


**Figure IV.8** Full $^{1}$H-NMR spectrum of **9** in $CD_3CN$. Residual solvent peaks (ppm): 1.94 (acetonitrile); 2.13 (water).

*Crystallography.*

The structures of compounds **1, 2, 7** and **8** were determined by single crystal X-ray diffraction experiments and are shown below in Figures IV.9, IV.10, IV.11 and IV.12. Slow diffusion of diethyl ether into concentrated solutions of the respective complex in $CH_3CN$ or 50:50 v/v $CH_3CN$:DCM yielded dark green needles. While crystals of **7** were obtained through vapor diffusion, X-ray quality crystals were grown by layering a concentrated $CH_3CN$ solution of the compound on toluene. Compound **9** was also recrystallized by vapor diffusion methods, but the crystals obtained were of insufficient quality to obtain diffraction data.

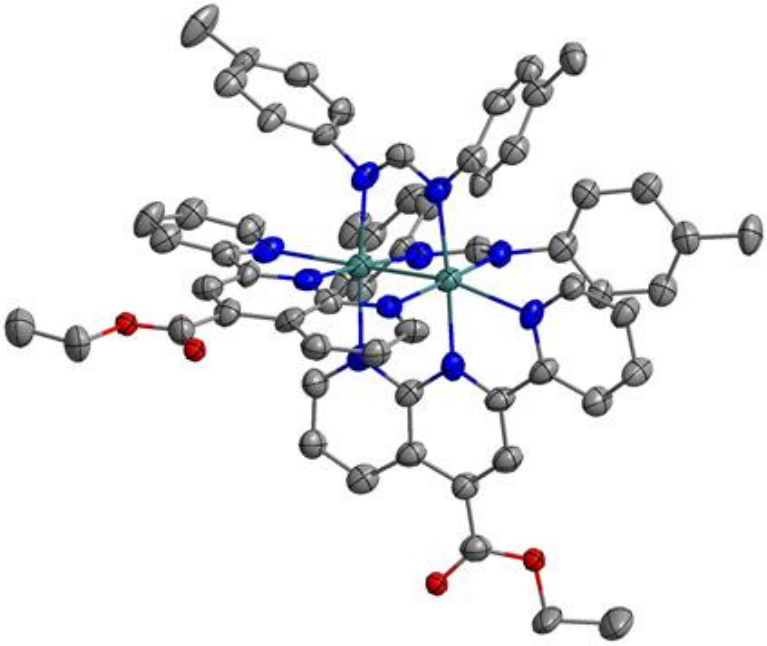

**Figure IV.9** Thermal ellipsoid plot for **1** shown at the 50% probability level. Interstitial solvent molecules, counterions, and hydrogen atoms have been omitted for the sake of clarity.

***cis*-[Rh$_2$(DTolF)$_2$(2COOEtpynp)$_2$][BF$_4$]$_2$:** Compound **1** crystallizes in the space group $P\bar{1}$. The molecule consists of a cationic dirhodium core that is bridged by two anionic formamidinate ligands, [DTolF]$^-$ along with two tridentate naphthyridine-based ligands. The tridentate ligand is functionalized on the naphthyridyl moiety with the ester group, such that it is trans to the formamidinate bridging ligands and across from the Rh-Rh bond. Two [BF$_4$]$^-$ anions per [Rh$_2$]$^{4+}$ are also present in the crystal structure. The Rh-Rh bond distance is 2.473(2) Å, which is within the range of literature values for Rh-Rh bonds and slightly longer than the values reported for other axially blocked dirhodium complexes.[83, 135] The Rh-N$_{form}$ bond length ranges from 2.032 Å to 2.106 Å. The average Rh-N bond distance between the dirhodium unit and the pynp ligand is 2.058 Å in the equatorial

positions and longer at the axial sites, averaging 2.250 Å. As is the case for other axially blocked complexes, the tridendate naphthyridine-based ligand has a bite angle that causes the Rh-Rh-N bond to deviate from linearity. The Rh-Rh-$N_{ax}$ angle for **1** is 165.95°. The geometry of the coordinating ligands impart a small degree of strain on the molecule, as evidenced by the $N_{form}$-Rh-Rh-$N_{form}$ torsion angle of 9.41° and there the $N_{eq}$-Rh-Rh-$N_{eq}$ torsion angle of 8.51°.

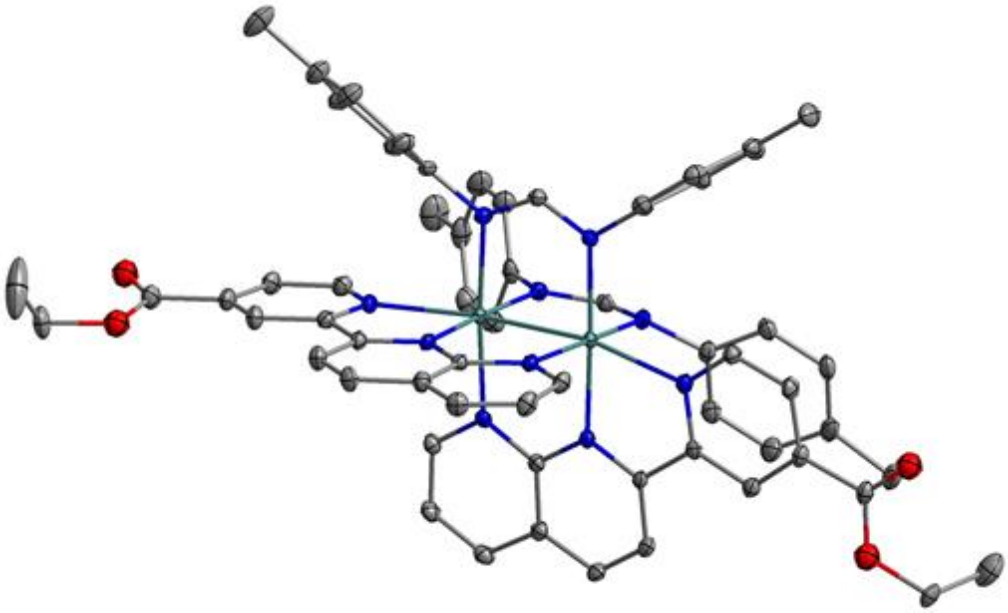

**Figure IV.10** Thermal ellipsoid plot for **2** shown at the 50% probability level. Interstitial solvent molecules, counterions, and hydrogen atoms have been omitted for the sake of clarity.

***cis*-[$Rh_2$(DTolF)$_2$(4COOEtpynp)$_2$][$BF_4$]$_2$:** Compound **2** crystallizes in the $P2_1/c$ space group. As is in the case of **1,** this molecule consists of a cationic dirhodium core and the charge is balanced by two outer-sphere $[BF_4]^-$ anions as well as two anionic formamidinate ligands, $[DTolF]^-$, which bridge the dirhodium unit. The dirhodium core is also supported

by two tridentate naphthyridine-based ligands that each coordinate in two equatorial positions through the naphthyridyl moiety and block the axial position of the dirhodium core through the pyridyl moiety. These ligands are functionalized by an ester group on the pyridyl moiety. An interstitial diethyl ether molecule is also present in the crystal structure. The Rh-Rh bond length is 2.4821(5) Å, which is slightly longer than that in **1.** The Rh-$N_{form}$ bond distances fall in a larger range than what was observed in **2,** and are from 2.038(3) Å to 2.059(3) Å. The Rh-N bond distance between the dirhodium unit and the pynp ligand averages 2.055(3) Å in the equatorial positions, which is very similar to **1,** but is shorter at the axial sites, averaging 2.240 Å. The presence of the electron withdrawing ester moiety is expected to be the source of this relative Rh-N bond shortening and Rh-Rh bond lengthening as compared to **1.** The bite angle of the tridentate naphthyridine-based ligand results in a deviation from linearity along the Rh-Rh-$N_{ax}$ bond, which has an angle of 168.30°. Looking down the Rh-Rh bond, the N-C-N portion of the formamidinate ligand is nearly perfectly aligned, as is the naphthyridine ligand, with only a small $N_{form}$-Rh-Rh-$N_{form}$ torsion angle of 2.88° and $N_{eq}$-Rh-Rh-$N_{eq}$ torsion angle of 1.48°.

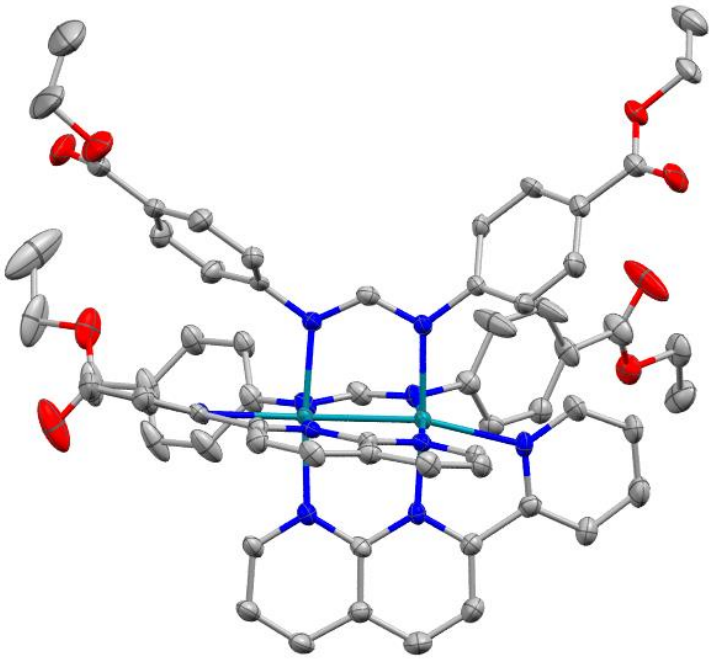

**Figure IV.11** Thermal ellipsoid plot for **7** shown at the 50% probability level. Interstitial solvent molecules, counterions, and hydrogen atoms have been omitted for the sake of clarity.

***cis*-[Rh$_2$(COOEt-Form)$_2$(pynp)$_2$][PF$_6$]$_2$:** Compound **7** crystallizes in the space group $P\bar{1}$. The structure features a cationic dirhodium core supported by two anionic formamidinate ligands, [DTolF]$^-$, and two tridentate naphthyridine-based ligands. Two anionic [PF$_6$]$^-$ molecules crystallize along with the dirhodium complex as counterions, and the unit cell consists of one acetonitrile and two toluene solvent molecules as well. The Rh-Rh bond distance is 2.4897(5) Å, which is comparable to literature values of the metal-metal bond in dirhodium (II,II) complexes. This is longer than 2.4771(5) Å, the distance reported for *cis*-[Rh$_2$(DTolF)$_2$(pynp)$_2$][PF$_6$]$_2$ which is due to the electron withdrawing ester substituents on the formamidinate ligands of **7**, in contrast to the electron donating methyl

moieties of the DTolF ligand. The average Rh-$N_{form}$ bond distance is 2.055(4) Å, which is shorter than the corresponding distances observed for **1** and **2.** The Rh-N bond distance between the dirhodium unit and the pynp ligand averages 2.051(4) Å in the equatorial positions, and is longer at the axial sites, averaging 2.255(4) Å. Similar to other $Rh_2(pynp)_2$ complexes, the Rh-Rh-N bond is not perfectly linear due to the bite angle of the ligand, resulting in a bond angle of 166.40°. Due to the slight steric bulk afforded by the ester substituted phenyl rings, the N-C-N moiety of the bridging ligands are not perfectly eclipsed. The $N_{form}$-Rh-Rh-$N_{form}$ torsion angle is 7.17° and $N_{eq}$-Rh-Rh-$N_{eq}$ torsion angle is 5.40°.

***cis*-[$Rh_2$(COOEt-Form)$_2$(qnnp)$_2$][$PF_6$]$_2$:** Compound **8** crystallizes in the space group $P\bar{1}$. As is the case of **7,** the structure features a cationic dirhodium core supported by two anionic formamidinate ligands, $[DTolF]^-$, and two tridentate naphthyridine-based ligands. Two anionic $[PF_6]^-$ molecules crystallize along with the dirhodium complex as counterions. However, due to the different recrystallization procedures used, there are five interstitial acetonitrile molecules in the crystal structure. The Rh-Rh bond distance of **8** is shorter than **7,** and was determined to be 2.4539(5) Å. The average Rh-$N_{form}$ bond distance is 2.072(2) Å, while the average Rh-$N_{ax}$ bond between the metal and the qnnp ligand is 2.049(7) Å. This relative lengthening of the Rh-$N_{form}$ bond and shortening of the bonds *trans* to it with respect to **7** could be attributed to the more electron dense qnnp ligand interacting more strongly with the dirhodium core compared to the pynp ligand and withdrawing electron density from the Rh-$N_{form}$ bonds. This bulkier ligand also results in a more acute Rh-Rh-N bond angle of 161.36° and imparts greater strain in the molecule

as well. The $N_{form}$-Rh-Rh- and $N_{eq}$-Rh-Rh-$N_{eq}$ torsion angles were determined to be 20.53°, and 17.20°, respectively, reflecting the increased steric strain.

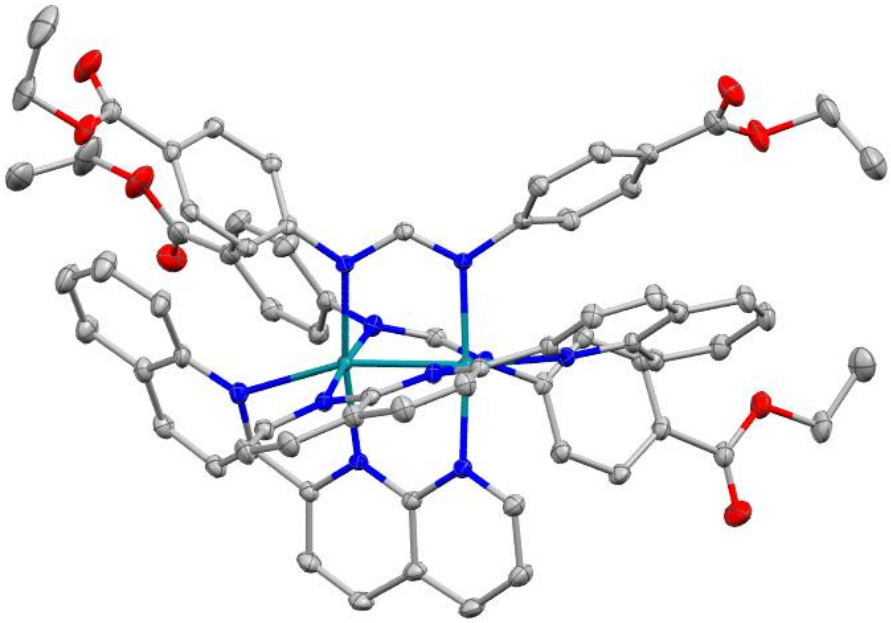

**Figure IV.12** Thermal ellipsoid plot for **8** shown at the 50% probability level. Interstitial solvent molecules, counterions, and hydrogen atoms have been omitted for the sake of clarity.

*Electronic Absorption Spectroscopy*

The absorption spectra of **1** and **2**, and **7**-**9** measured in acetonitrile are shown in Figures IV.13 and IV.14, respectively. The corresponding molar absorptivity values are presented in Table VI.1

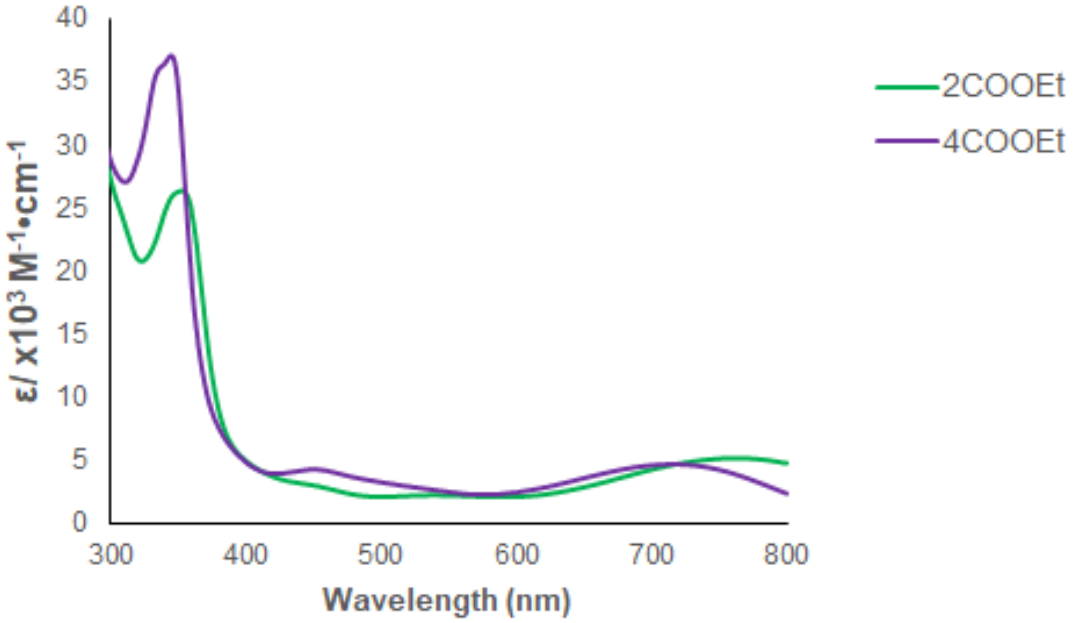


**Figure IV.13** Electronic absorption spectra in $CH_3CN$ for **1** (green) and **2** (purple).

Compounds **1** and **2** display electronic spectral features similar to the pynp cations $[Rh_2(CH_3CO_2)_2(pynp)]^{2+}$ and $[Rh_2(DTolF)_2(pynp)]^{2+}$.[83] The intense absorption in the UV at approximately 350 nm is attributed to ligand centered ππ* transitions. Both complexes exhibit intense charge transfer bands spanning the visible to near IR region, which can be assigned as having ML-LCT character and which, as previously discussed in the literature, result mainly from HOMO-LUMO transitions. The lowest energy maxima for these absorptions is bathochromically shifted for **2** with respect to **1**, at 770 nm as compared to

700 nm. This shift is attributed to the position of the electron withdrawing ester group on the electron accepting ligand where the ester has a greater electron withdrawing effect, thus increasing the relative HOMO-LUMO gap in the case of **2**.

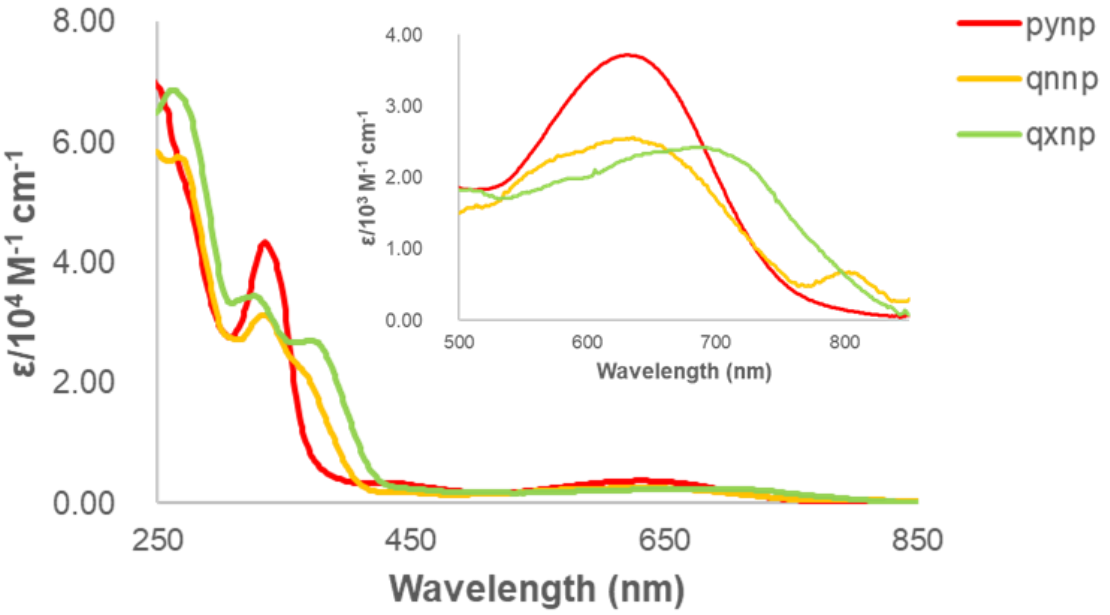


**Figure IV.14** Electronic absorption profiles in $CH_3CN$ for **7** (red), **8** (yellow) and **9** (green).

Complexes **7-9** also display spectral features similar to the axially-blocked complexes $[Rh_2(DTolF)_2(pynp)]^{2+}$, $[Rh_2(DTolF)_2(qnnp)]^{2+}$ and $[Rh_2(DTolF)_2(qxnp)]^{2+}$, respectively. As is the case for $[Rh_2(DTolF)_2(pynp)]^{2+}$, as well as **1** and **2,** the strong absorptions in the UV region for **7-9** can be attributed to $\pi\pi^*$ transitions arising from the axially-blocking ligands. These three complexes also exhibit intense low energy charge transfer bands which are attributed to primarily HOMO-LUMO type transitions which give rise to their ML-LCT character. Compounds **7**, **8** and **9** exhibit maxima at 634 nm (3710 $M^{-1}$ $cm^{-1}$), 627 nm (2540 $M^{-1}$ $cm^{-1}$), and 685 nm (2430 $M^{-1}$ $cm^{-1}$), respectively. The

absorption of **9** is bathochromically shifted with respect to **7**, due to the increased conjugation and electron accepting character afforded by the qxnp ligand as compared to the pynp ligand. Overall, it should be noted that the absorption features of **7, 8** and **9** are hypsochromically shifted with respect to **1** and **2,** due the electron withdrawing ester moieties on the bridging ligands, resulting in the formamidinate ligands being less electron donating in character. However, although the nature of the bridging ligands results in higher energy transitions, **7**, **8** and **9** still absorb strongly in the visible and, in the case of **9**, tail out into the near IR region.

**Table IV.1** Electronic absorption maxima for **1**, **2**, **7-9** in acetonitrile

| **Complex** | $\lambda_{abs}$ **/ nm (ε / ×10$^3$ M$^{-1}$ cm$^{-1}$)** |
|---|---|
| **1** | 351 (27.1), 456 (4.2), 770 (5.9) |
| **2** | 342 (25.2), 453 (3.6), 700 (5.7) |
| **7** | 337 (43.4), 432 (3.4) 634 (3.7) |
| **8** | 327 (30.3), 440 (1.9), 627 (2.5) |
| **9** | 326 (34.5), 373 (27.0), 685 (2.4) |

*Electrochemistry.*

Compounds **1**, **2**, **7**, **8** and **9** were studied by cyclic voltammetry, the results of which are presented in Table IV.2. The measurements were performed in $CH_3CN$ with 0.1 M $Bu_4NPF_6$ and the couples are referenced to Ag/AgCl.

**Table IV.2** Cyclic voltammetric data for **1, 2, 7-9** in acetonitrile

| Complex | $E_{1/2}$ / V[b] |
|---|---|
| **1** | +0.96, –0.42, -0.57, -1.135, -1.343 |
| **2** | +0.958, –0.61, -0.77, -1.386. -1.607 |
| **7** | +1.07, -0.69, -0.84, -1.51 |
| **8** | +1.10, -0.69, -0.85, -1.44 |
| **9** | +1.29, -0.35, -0.54, -1.03, 1.26 |

[b] *vs* Ag/AgCl in 0.1 M $Bu_4NPF_6/CH_3CN$

Compounds **1** and **2** both feature one reversible oxidation event upon anodic scanning and four reversible reduction events upon cathodic scanning (Figure IV.15). The $E_{1/2}$ values for the oxidation of **1** and **2** are +0.99 V and +0.96 V, respectively. Based on previous studies of dirhodium II,II complexes, the oxidation event is assigned as an oxidation of the metal center (Rh(II,II)/Rh(II,III), with some formamidinate ligand contribution.[83, 111] These values are more positive than the $E_{1/2}$ reported for $[Rh_2(DTolF)_2(pynp)_2]^{2+}$, which is +0.92 vs Ag/AgCl.[83] This difference is attributed to the presence of the electron-withdrawing ester groups on the napthyridine-based ligand which renders the dihodium core more difficult to oxidize. The four reversible reductions

observed for these two complexes are napthyridine ligand based reduction events as each one can be reduced by two electrons. The reduction potentials observed for **2** are consistently about 200mV greater than those of **1.** The first reduction is observed at -0.46 V and -0.61V for **1** and **2**, respectively. In accordance with the assignment of this couple in similar compounds, this event is a one-electron reduction of each of the two naphthyridine ligands. A second reduction is observed at -0.59 V for **1,** and -0.77 V for **2.** The third reduction occurs at -1.12 V and -1.39 V for **1** and **2,** respectively, while the fourth event is observed at -1.36 V and 1.61 V. The total number of reductions is four.

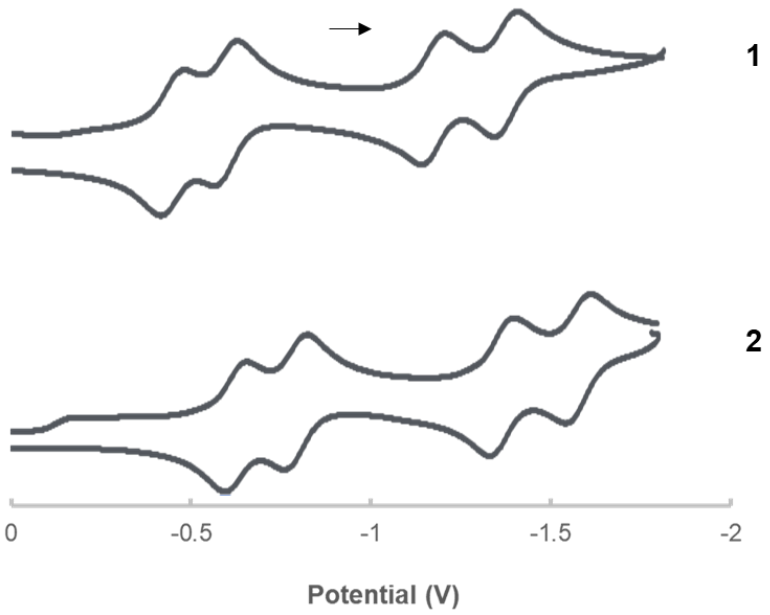


**Figure IV.15** Cyclic voltammograms highlighting the reduction events of **1** and **2** in acetonitrile (1 mM $[Rh_2]^{4+}$, 0.2 M $[NBu_4][PF_6]$, glassy carbon WE, Pt wire CE, $Ag/Ag(NO_3)$ RE, $\nu = 0.1$ mV/s)

Compounds **7**, **8** and **9** all feature many reversible or quasi-reversible reduction events upon cathodic scanning, and one reversible oxidation event upon anodic scanning (Figure IV.16). The oxidation event is assigned as an oxidation of the metal center (Rh(II,II)/Rh(II,III), with some formamidinate ligand contribution, and is observed for **7, 8** and **9** at +1.07 V, +1.11 V and + 1.29 V, respectively. These assignments are based upon previous studies of dirhodium (II,II) complexes[83]. By comparison, $[Rh_2(DTolF)_2(pynp)]^{2+}$, $[Rh_2(DTolF)_2(qnnp)]^{2+}$ and $[Rh_2(DTolF)_2(qxnp)]^{2+}$, were observed to have oxidations $E_{1/2}$ = +0.92 V, +0.99 V, and +1.08V, respectively. The positive increase in $E_{1/2}$ is attributed to the electron withdrawing formamidinate bridging ligand, which is consistent with previous studies in which the potential for each couple becomes more positive as the electron-withdrawing ability of aryl substituents increases.[136, 137] Furthermore, the more extended pi-system of the quinolinyl and quinoxalinyl moieties on **8** and **9,** respectively, results in a higher oxidation potential as opposed to the effects of the pyridyl moiety on complex **7.**

There are three reversible reductions events observed for **7** at $E_{1/2}$ values of -0.69 V, -0.84 V and -1.51 V and one reduction that is visible but not fully resolved because of the solvent cut-off. In the case of **8,** the reductions appear at potentials that lead to overlap which renders it difficult to assess the peak potential currents required for reversibility criteria. The approximate $E_{1/2}$ values are -0.69 V, -0.85 V and -1.44 V. In the case of **9**, four reversible reductions were observed at $E_{1/2}$ values of -0.35 V, -0.54 V, -1.03 V and -1.26 V.

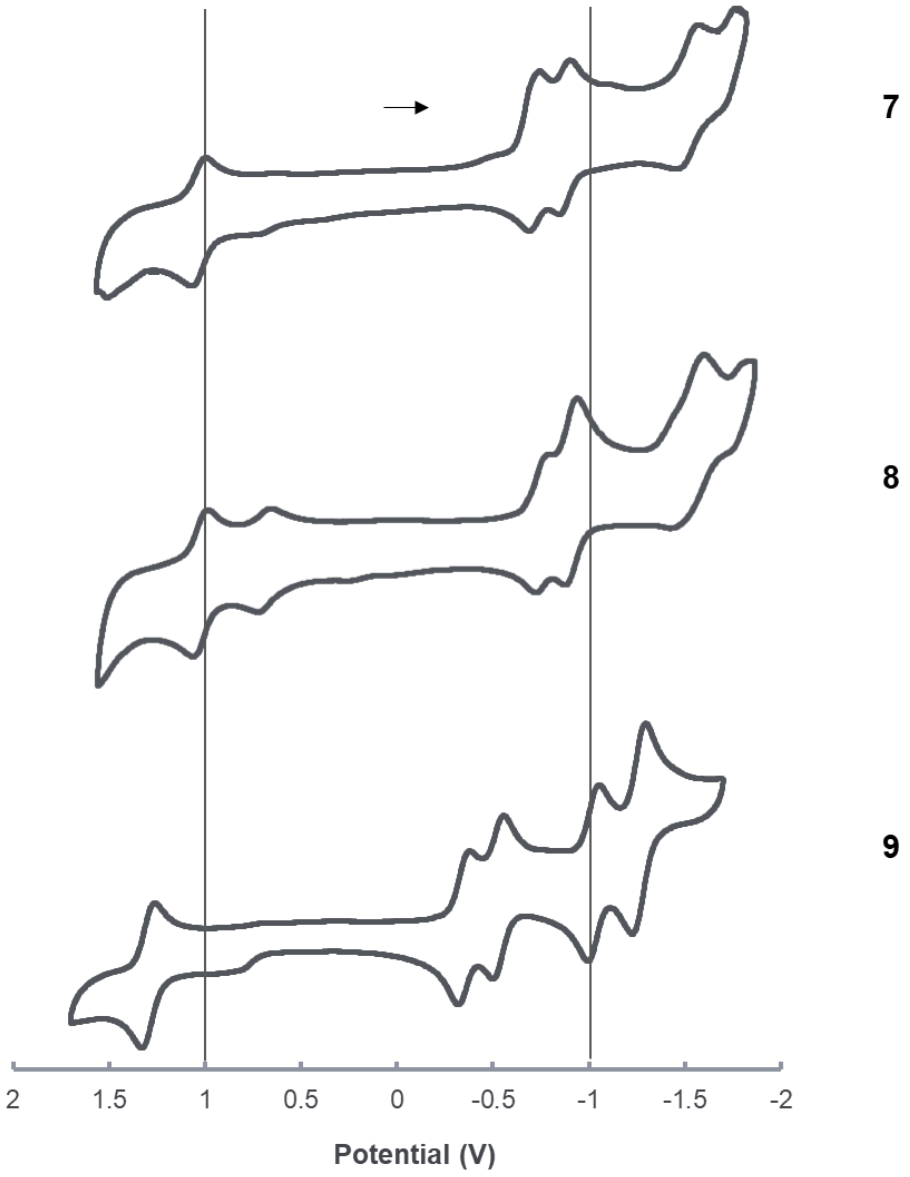


**Figure IV.16** Cyclic voltammograms of **7, 8** and **9** in acetonitrile (1 mM $[Rh_2]^{4+}$, 0.2 M $[NBu_4][PF_6]$, glassy carbon WE, Pt wire CE, $Ag/Ag(NO_3)$ RE, $\nu = 0.1$ mV/s). Vertical lines are guides to the eye for the comparison of redox potentials.

The observation of four well-resolved reductions instead of three is likely due to the presence of the more conjugated qxnp ligand, resulting in a lowering of the reduction

potentials such that an additional event falls within the acetonitrile solvent window limit. The four reduction events are assigned to the naphthyridine ligands, based on previous assignments for related similar compounds.[138] It is well known that the pi-accepting ligands can each be reduced by two electrons which leads to four total reductions.

*Electronic Structure Calculations:*

In order to gain insight into the electronic properties of these complexes, DFT and TD-DFT calculations were performed for **1**, **2**, **7**, **8** and **9.** The geometric parameters from the crystal structures of **1**, **2**, **7** and **8** were used as starting points for the calculations, the computational results are in close agreement with the crystallographic trends that were observed. Selected bond distances, bond angles and dihedral angles as determined by the gas-phase geometry optimization computations are shown and the respective contributions of the rhodium core, formamidinate ligands and naphthyridine based ligands to the molecular orbitals are compiled. The calculated molecular orbitals for these complexes are presented in Figure IV.17.

The HOMOs of **1** and **2** are at approximately the same energies, and the contributions to the HOMO are from the bimetallic rhodium core (δ*) and the formamidinate bridging ligand. The HOMO-1 is primarily formamidinate in character, while the HOMO-2 is predominantly the $Rh_2(\pi^*)$ level. The LUMO and LUMO+1 levels of **2** are destabilized with respect to **1** by approximately 0.132 eV. As the contributions to the LUMO can be identified as being mostly localized on the naphthyridine based ligand, and the contributions to the LUMO+1 is primarily naphthyridine based ligand with some rhodium character, these results are consistent with the impact of the position of the ester

substituent position the electronic and structural properties of the complexes, as determined experimentally. In considering the orbital energies and compositions of **7**, **8**, and **9**, there is a larger HOMO-LUMO gap for these three complexes. This finding is consistent with the electronic absorption experiments which revealed that these complexes do not absorb as well into the near IR region, and is further supported by TD-DFT experiments.

The HOMO of **7**, **8** and **9** are seen to be comprised of both formamidinate character and $Rh_2(\delta^*)$ character, which is similar to the cases of **1** and **2.** The relative energy of this orbital is fairly consistent for **7**, **8** and **9** but the electronic differences between the pyridyl, quinolinyl and quinoxilyl moieties on the naphthyridine based ligands are evidenced by the stabilization of the LUMO across the series. As is the case for **1** and **2,** the main contribution to the LUMO is from the naphthyridine based π-accepting ligand, and so the increasing conjugation serves to decrease the energy of the LUMO, with a difference of 0.282 eV from **7** to **9.** These computational results support the decrease in reduction potential which was measured experimentally by cyclic voltammetry.

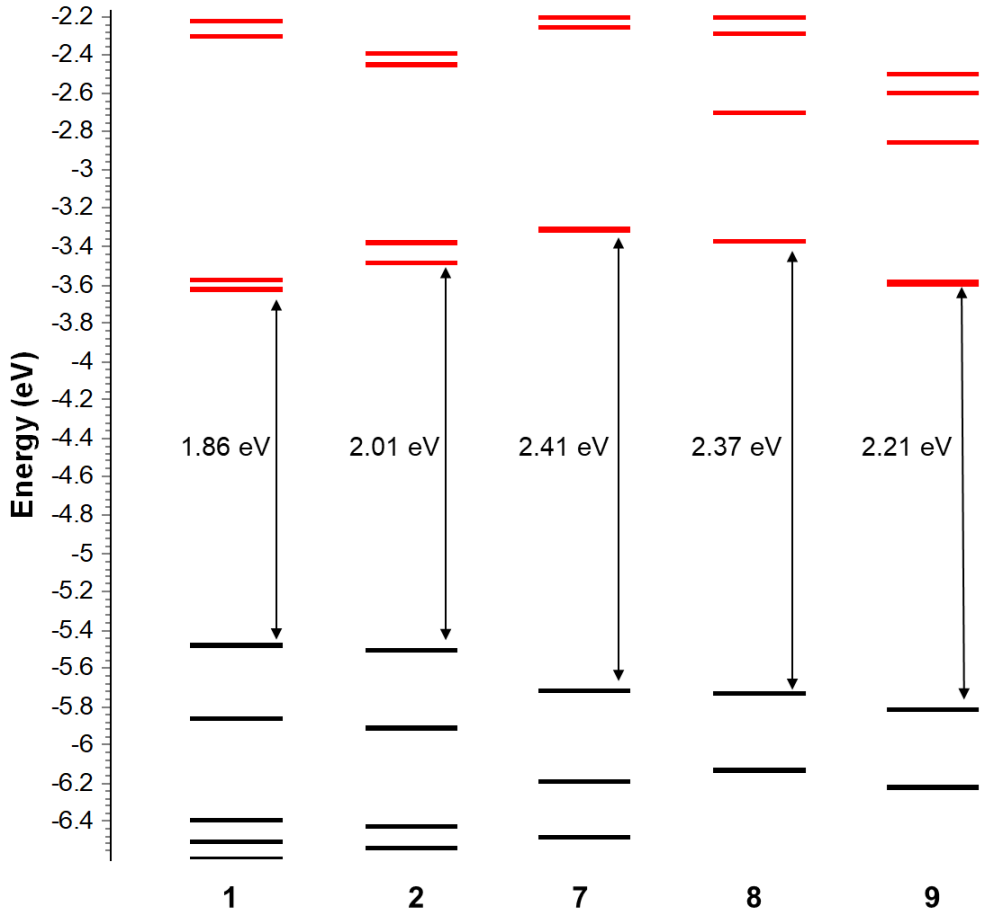


**Figure IV.17** Calculated molecular orbital diagrams for **1**, **2**, **7-9** and their HOMO-LUMO energy gaps (black = occupied, red = unoccupied).

TD-DFT/PCM calculations were performed to determine the origin of the electronic transitions, most of which involve the HOMO or lower energy orbitals and LUMO or the LUMO+1. The lowest energy absorption features of **1** and **2** at 938 nm and 851 nm are calculated to be HOMO → LUMO transitions which confirm the ML-LCT character of those states (Figure IV.18). The features at approximately 700 nm or 640 nm for **1** and **2** involve HOMO-1 → LUMO+1 transitions, and are assigned as LLCT transitions. The shoulder at approximately 450 nm is calculated to be a transition from the

HOMO-6 to the LUMO, and is an LLCT. The higher energy transitions are calculated to have more MLCT character. The lowest energy transitions for **7**, **8** and **9** appear at 682 nm, 710 nm and 775 nm, respectively. Computationally, the nature of these transitions is confirmed to be ML-LCT, as they result mainly from the HOMO → LUMO transition. The hysochromic shift of the absorbance of this series of complexes is consistent with the experimental electronic absorption measurements, and is attributed to the electron withdrawing substituents on the formamidinate bridging ligand. The higher energy transitions for **7**, **8** and **9** are consistent with those described for **1** and **2**.

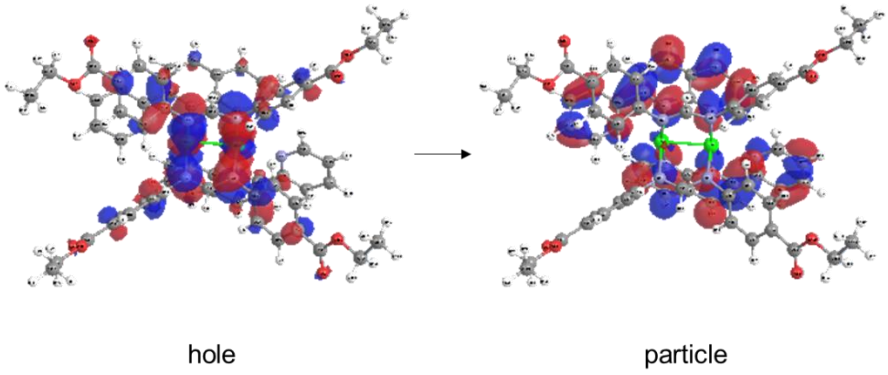


**Figure IV.18** Representative example of the calculated HOMO→LUMO transition.

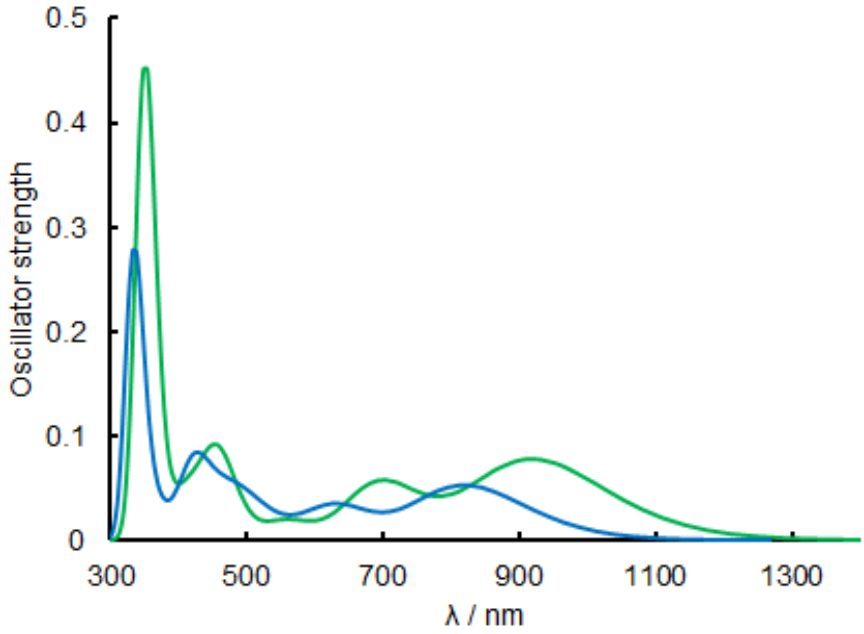


**Figure IV.19** TD-DFT calculated spectra for *cis*-[$Rh_2$(DTolF)$_2$(2COOHpynp)$_2$] (green) and *cis*-[$Rh_2$(DTolF)$_2$(4COOHpynp)$_2$] (blue).

## Conclusions

The structural and electronic properties of two series of dirhodium complexes with potential to be used as dyes for DSSC applications were presented in this chapter. The 2-(pyridin-2-yl)-1,8-naphthyridine-4-carboxylic acid and 2-(1,8-naphthyridin-2-yl)isonicotinic acid (4-COOHpynp and 2-COOHpynp) ligands were synthesized and reacted with [$Rh_2$(DTolF)$_2$(MeCN)$_6$]$^{2+}$ (DTolF = N,N'-Di-*p*-tolyl-formamidine). Functionalization of the axial blocking ligand with carboxylate anchoring groups affords these complexes the potential to be used as n-type sensitizers for $TiO_2$. In addition to introducing a carboxylate functionality to the axial blocking ligands, the use of both

functionalized positions allowed us to investigate the effects of the carboxylate group on the properties of the resulting complex with axial versus equatorial positioning with respect to the metal-metal core. X-ray crystallographic experiments confirmed the identity of these complexes, which were found to exhibit strong absorption in the visible and into the near-IR region and to undergo multiple accessible reversible redox events. Functionalization of the pynp type ligand on the naphthyridyl moiety versus the pyridyl moiety served to increase the electron withdrawing effects of the ester functional group. The excited state charge injection abilities of these sensitizers are currently under investigation by our collaborators at The Ohio State University.

In addition, a series of complexes designed for hole injection were also synthesized and characterized. In these molecules, the formamidinate bridging ligand was functionalized with the carbox ylate anchoring groups, allowing for potential anchoring and sensitization of NiO. These compounds of the type $[Rh_2(COOEt\text{-}Form)_2(NNN)_2]^{2+}$ ( NNN = pynp, qxnp, qnnp) also show promising panchromic absorption properties and exhibit multiple reversible redox events. Structural and electronic trends are similar to the DTolF analogues, although the presence of the electron withdrawing ester group leads to greater charge separation. The photophysical properties and excited state charge injection abilities of these complexes are also currently under investigation by our collaborators at The Ohio State University.

# CHAPTER V

# CONCLUDING REMARKS AND FUTURE DIRECTIONS

Dirhodium (II,II) complexes have long been studied for their many applications from catalysis to bioactivity, and, more recently, photoactivity. The metal-metal bonded scaffold afforded by dirhodium paddlewheel and partial paddlewheel complexes is a highly tunable and accessible platform for optimizing these properties. These complexes are typically water- and air-stable which makes them practical candidates for the aforementioned applications. Careful selection of the ligands combined with informed modifications allows for tuning of both the ground state and excited state properties of the complexes. In this dissertation research, new classes of dirhodium complexes bearing the strongly electron donating formamidinate ligand were designed for use as photosensitizers for both biological therapeutics and solar energy conversion applications. The formamidinate ligand was used to generate a mixed bridging ligand compound which was used in the context of photodynamic therapy (PDT) as a proof-of-concept investigation. The effects of substituted formamidinate bridging ligands were systematically investigated vis-à-vis electronic and structural trends in a series of partial paddlewheel dirhodium complexes featuring halogenated formamidinate bridging ligands. Access to the long-lived triplet excited state of these complexes affords the opportunity to use these complexes for excited state charge transfer processes. By harnessing the ability to tune and functionalize the ligands around the rhodium core, it was possible to design two series

of dirhodium complexes with functionalities such that allow them to be anchored to semiconductor materials.

In Chapter II, the unique starting material with a 1:3 mixed bridging ligand ratio, $Rh_2(F_2Form)(O_2CCH_3)_3$, was prepared and used to synthesize $[Rh_2(F_2Form)(O_2CCH_3)(dppn)_2](O_2CCH_3)_2$. The $Rh_2(F_2Form)(O_2CCH_3)_3$ molecule is a result of a single substitution of an acetate ligand with a formamidinate ligand from the well-known rhodium acetate precursor $Rh_2(O_2CCH_3)_4$. It is the first example of a partial paddlewheel of its kind with a 1:3 ratio of different bridging ligands. The $Rh_2(F_2Form)(O_2CCH_3)_3$ compound is similar to $Rh_2(O_2CCH_3)_4$ in its electronic absorption profile and transitions although the presence of one electron donating formamidinate ligand leads to a red-shifting of the absorption of the complex. A series of compounds was prepared with the diimine ligands bpy (2,2′-bipyridine), phen (1,10-phenanthroline), dpq (dipyrido[3,2-*f*:2′,3′-*h*]quinoxaline), dppz (dipyrido[3,2-*a*:2′,3′-*c*]phenazine), and dppn (benzo[*i*]dipyrido[3,2-*a*:2′,3′-*c*]phenazine). The dppn complex is discussed in detail in this dissertation as well as the $Rh_2(F_2Form)(O_2CCH_3)_3$ staring material, as those are the two complexes which highlight the mixed bridging ligand scaffold and demonstrate its promise for the development of sensitizers for PDT applications. The $[Rh_2(F_2Form)(O_2CCH_3)(dppn)_2]^{2+}$ cation (**2**) exhibits a relatively high singlet oxygen quantum yield of 0.58(8) and, upon irradiation with visible light, photocleaves plasmid DNA and induces cell death *via* apoptotic and necrotic mechanisms. The photocytotoxicity of this complex against HeLa cells was found to increase by a factor of 25.3 upon irradiation with visible light. The presence of the dppn ligands is crucial for

these properties, as the $^3\pi\pi$ afforded by the ligands allows for the sensitization of $^1O_2$. The electronic spectrum of this complex extends beyond 650 nm with the lower energy features being attributed to $Rh_2(\delta^*)/F_2Form(\pi^*)\rightarrow dppn(\pi^*)$ charge transfer in nature as observed in related complexes. The highly conjugated dppn ligand helps to red-shift the absorption of these types of complexes into the PDT window, a requisite condition for tissue penetration in photochemotherapy applications.

The mixed ligand platforms presented in this dissertation are ideal for selectively tuning the ligand field around the dirhodium core. The $[Rh_2(F_2Form)(O_2CCH_3)(dppn)_2]^{2+}$ cation exhibits photoactivity and is promising for PDT applications, but, in order for the results to be meaningful, it important to compare and contrast its activity to that of the bis-substituted complexes that do not have a mixed bridging motif. To this end, the photocytotoxicity of the compounds $[Rh_2(O_2CCH_3)_2(dppn)_2][BF_4]_2$ **(1)** and $[Rh_2(F_2Form)_2(dppn)_2][BF_4]_2$ **(3)** were assayed against HeLa cells as well (Figure V.1). While **1** is known to exhibit photocytotoxicity against the Hs-27 human fibroblast cell line, there are no extensive studies in the literature of their activity against cancer cell lines. Compound **3** was observed to have an extraordinarily high photocytotoxicity index as compared to the mixed bridge complex, while **1** was not as active against this cell line, though comparable to the order of magnitude of photocytotoxicity demonstrated by the mixed bridge complex **2.** A summary of the cell viability data and photocytotoxicity studies is presented in Table V.1.

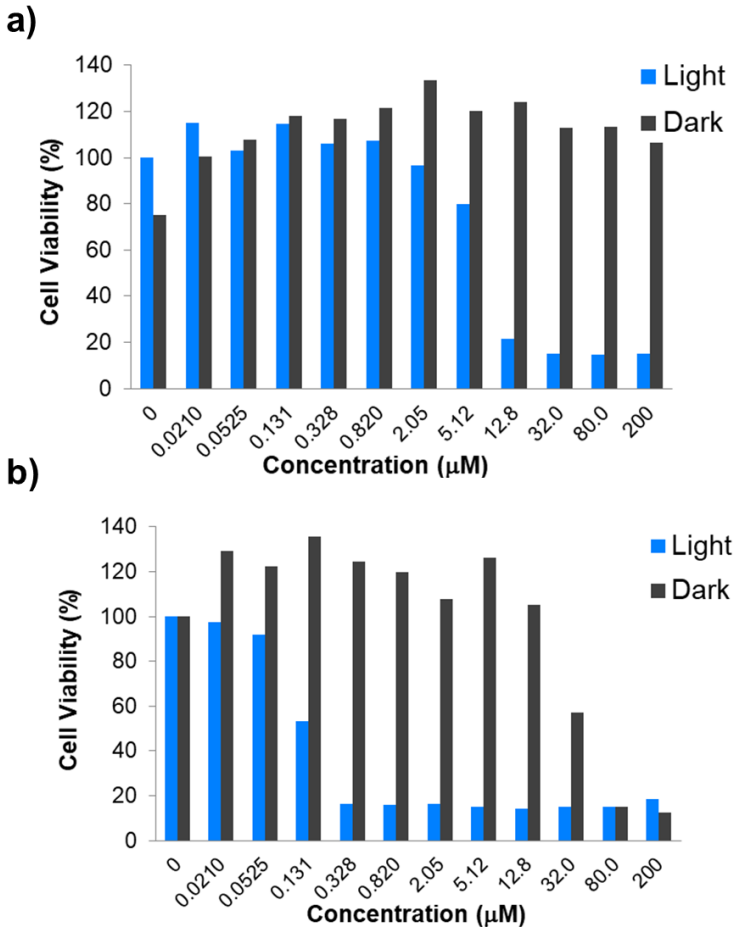


**Figure V.1** Photocytotoxicity of a) **1** and b) **3** against HeLa cells in the dark and upon irradiation ($\lambda_{irr} \geq 400$ nm $t_{irr} = 1$ h).

**Table V.1** Summary of cell viability data against HeLa cells.

| Complex | $LC_{50}$ (μM) | $LC_{50}^{*}$(μM) | PI |
|---|---|---|---|
| **1** | > 200 | 8.95 | > 22.3 |
| **2** | 159 | 6.29 | 25.3 |
| **3** | 37.7 | 0.142 | 266 |

It is likely that these differences are due to the cellular uptake of the three complexes. In general fluorination improves cellular uptake, which is observed for a number of pharmaceutically active compounds that are designed intentionally with fluorine substituents.[139, 140] It would be of interest to further explore the effects of fluorine substitution. Some work using poly-fluorinated formamidinate ligands is shown in Figure V.2 was performed and complexes featuring $F_3$-Form, $F_4$-Form and $F_5$-Form were synthesized. However, the addition of multiple electron withdrawing groups on the bridging formamidinate is not conducive to the application of these complexes for PDT applications, as those substituents do not optimize the complexes for lower energy absorption. Fluorine atoms, or other substituents, could be installed on the diimine electron accepting ligand instead. The new mixed bridging scaffold and the methodology by which it was synthesized is an exciting avenue of exploration for the design of a variety of new dirhodium complexes that have previously been inaccessible. The acetate ligands on $Rh_2(O_2CCH_3)_4$ could be singly substituted for various other bridging ligands which would open up a wealth of possibilities for the preparation of molecules with at least three different bridging ligands.

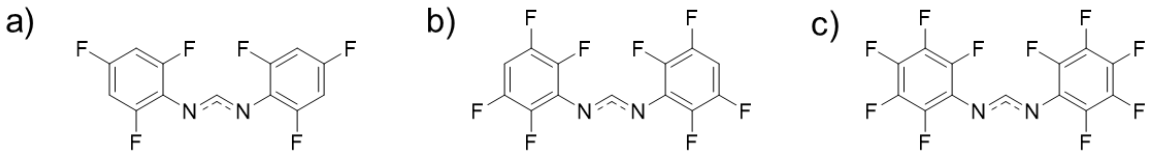


**Figure V.2** Chemical structures of fluorinated formamidinate ligands

The biological activity of these complexes was investigated using the HeLa cell line, which is a standard first-line screening method. In order to be relevant, however, it is

important to develop chemotherapeutic agents that are active against cancers that are resistant to traditional drugs such as *cis*-platin.[141, 142] Metallodrug resistant cell lines that these compounds could be investigated with include COLO-316, OVCAR-8 and NCI-ADR Res. Also, a number of cancers are more difficult to target with traditional chemotherapy methods as they lack receptors on the cell surface that are commonly found on other cancer cells, for examp le triple-negative breast cancer.[143] It is currently of great interest in the field to develop new therapeutics that can effectively target these cancers, and these new classes of dirhodium complexes should be tested for these applications.

As such, compounds **1**, **2** and **3** were tested against the MDA-MB-231 triple negative breast cancer cell line, and light induced cell death was observed for all three compounds, to varying degrees. The cell viability results are shown in Figure V.3 and summarized in Table V.2. Similar to the observations when these compounds were tested against the HeLa cell line, **3** was determined to have the highest phototoxicity index, ten-fold greater than **1** or **2.** However, **3** shows much greater dark toxicity than **1** or **2**, for which an exact $LC_{50}$ was unable to be determined, as the highest concentration tested was not enough to induce cell death. Compound **2**, which bears one fluorinated bridging ligand, has a higher irradiated cytotoxicity than **1** but less than **3**, which is consistent with the degree of fluorination of the compound and the subsequent effect on cell uptake and toxicity.

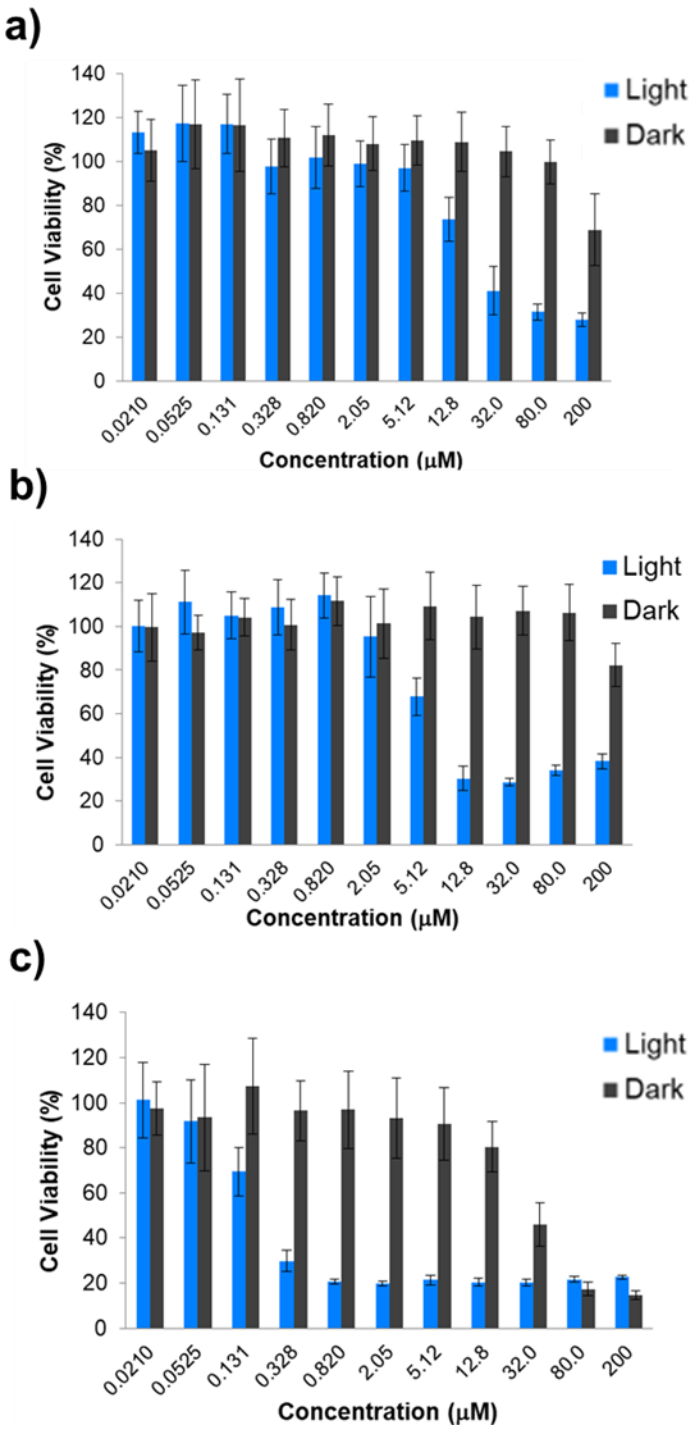


**Figure V.3** Photocytotoxicity of a) **1** b) **2** and c) 3 against MDA-MB-231 cells in the dark and upon irradiation ($\lambda_{irr} \geq 400$ nm $t_{irr} = 1$ h).

**Table V.2** Summary of cell viability data against MDA-MB-231 cells

| Complex | $LC_{50}$ (μM) | $LC_{50}^{*}$(μM) | PI |
|---|---|---|---|
| **1** | > 200 | 25.1 | > 8.00 |
| **2** | > 200 | 7.83 | > 25.6 |
| **3** | 27.5 | 0.218 | 126 |

Elucidating the mechanisms of cell death caused by dirhodium complexes is another challenge that is faced in this area of work. Using various confocal microscopy methods in conjunction with each other techniques can be used to identify where the compound is accumulating in the cancer cells. For example, the JC-1 assay serves to provide evidence that mitochondrial damage has occurred, which is usually a part of apoptotic pathways. It cannot be said, however, with any certainty that PDT agents cause direct damage to the mitochondria as opposed to depolarization occurring by a difference pathway induced by the PDT agent elsewhere. In this work, the Annexin-V FITC assay revealed evidence of apoptosis in the HeLa cells as evidenced by an increase in green fluorescence upon irradiation in the presence of $[Rh_2(F_2Form)(O_2CCH_3)(dppn)_2]^{2+}$ and also by the observed morphological changes. However, this assay itself, while suggesting that the complex ultimately results in apoptosis, does not indicate how the apoptosis was triggered and where the complex may be localizing and causing damage. A further avenue of investigation with respect to the use of dirhodium complexes for PDT applications is to use fluorescent tags as a method for tracking the localization of dirhodium compounds in the cell, as dirhodium complexes are not inherently fluorescent. Previous work in the Lippard group involved the coordination of fluorophores to the axial position of dirhodium tetra-carboxylate based compounds.[144] The results indicated that this is not a good

approach for designing a stable, tagged complex, however, as the axial positions of the dirhodium core are highly labile. The ability to functionalize the less labile equatorially coordinating ligands to the dirhodium core, though, opens up many possibilities for tuning the properties of the metal complex, as well as introducing other functionalities to the complex. Dr. Bruno Pena, a previous student in the Dunbar group, designed a ligand that featured a tethered fluorophore that was coordinated to the dirhodium (II,II) core. In this study, a phenanthroline-based linking ligand was designed and conjugated with a BODIPY tag which was reacted with $Rh_2(O_2CCH_3)_4$ to yield the fluorescent product.[145] The fluorescent quantum yield of 20% in aerated methanol indicated that the dirhodium core had not quenched all of the fluorescence. Human lung adenocarcinoma (A549) cells were then incubated with the complex and live cell imaging studies were performed. It was observed that the compound localizes in the mitochondria and lysosomes at concentrations of 1-100 μM used in the experiments. Based on confocal microscopy images, it was found that the free phenBODIPY ligand does not localize in the same manner as the dirhodium complex. These results, while informative, do not rule out whether the fluorophore plays a role in dictating the pattern of cellular localization, or how other bridging ligands and ligand functionalization may affect the cellular localization of the complex. Future work to test the hypothesis that the tethered fluorophore does not impact or completely alter the cellular localization of complexes with an $Rh_2^{4+}$ core should involve using different emissive tags conjugated to the previously reported linker and dirhodium scaffold, and then studying the resulting fluorescent dirhodium complexes *in vitro* by confocal microscopy. Furthermore, the BODIPY tagged ligand could be

incorporated into other dirhodium scaffolds with other bridging ligands and used to help visualize the localization patterns of those complexes (Figure V.4)

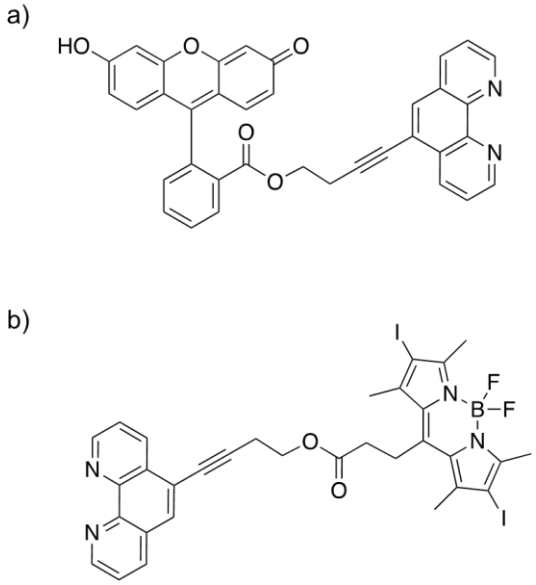


**Figure V.4** Chemical structure of proposed fluorophore tagged ligands.

A key question that arises from the work presented in Chapter II is *how formamidinate bridging ligands affect the properties of dirhodium photosensitizers?* The work in Chapter III addresses this question through the synthesis, characterization, as well as structural, electronic and kinetic studies of a series of complexes bridged by halogen substituted formamidinate ligands. The series $[Rh_2(X\text{-}Form)_2(MeCN)_6]^{2+}$ (X = F, Cl, Br, I and X-Form = N,N'-bis(*p*-X-phenyl)formamidinate) was selected for this study. X-ray crystallography showed that the four complexes all have very similar Rh-Rh bond distances, but that there is a measurable decrease in average Rh-N bond distance as the halogen electronegativity decreases. These trends are attributed to the electronegativity of the halogen constituents, and the results indicate a *trans* influence and π-accepting

properties of the formamidinate ligands. The electronegativity of the substituent affects and the electronic absorption of these complexes as well, as a small red-shift of the absorbance is observed across the series from F -> Cl -> Br -> I.

Differences in ligand lability across the series, and also investigations into the photostability of these complexes were performed using time-dependent $^{1}$H-NMR techniques under ambient conditions. In deuterated acetonitrile, the equatorial ligands exchange with the solvent, a process that was quantified by integrating the $MeCN_{eq}$ signal with respect to the formamidinate ligand signal. Upon irradiation, the process proceeds much more rapidly, but there is a slow ligand exchange process in the dark as well. The average rate constant was determined to decrease in the order F>Cl>Br>I with the F-form complex having the fastest rate of ligand exchange. The trend is consistent with the *trans* effect and correlates with the shortening of Rh-N bond distances through the series. DFT and TD-DFT calculations support the experimental observations described above.

As a stand-alone series, it was of interest to explore the various patterns and trends of the halogen substituted compounds but these molecules also be used as starting materials for other compounds for potential PDT applications. Therefore having a good understanding of the structural and electronic effects of the bridging ligand is helpful in the design of new compounds. A series of diimine complexes were synthesized and characterized (Figure V.5) The series $[Rh_2(X\text{-}Form)_2(NN)_2][BF_4]_2$ (X = F, Cl and Br and NN = phen, dppz, dppn) were synthesized and the $[Rh_2(X\text{-}Form)_2(dppn)_2]^{2+}$ complexes were assayed for their photocytotoxicities against HeLa cells.

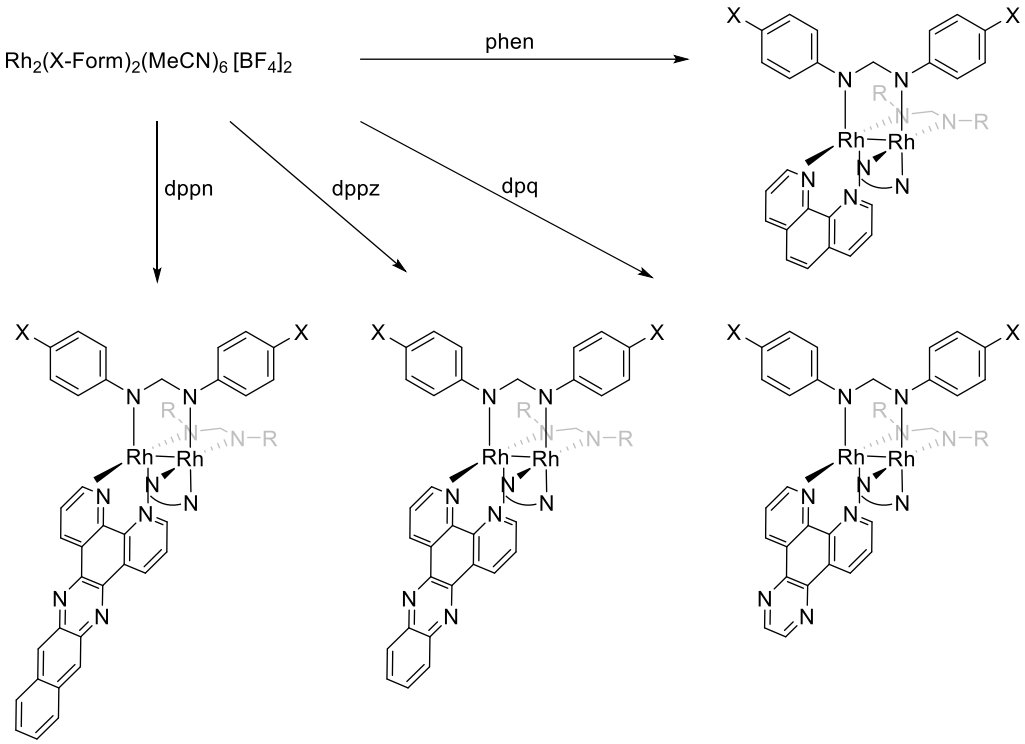


**Figure V.5** Schematic representation of the synthesis of complexes of the type $[Rh_2(X\text{-}Form)_2(NN)_2]^{2+}$ with axial solvent ligands omitted for clarity.

Both the $[Rh_2(F\text{-}Form)_2(dppn)_2]^{2+}$ and $[Rh_2(Cl\text{-}Form)_2(dppn)_2]^{2+}$ complexes exhibit very high photocytotoxicities in contract to the $[Rh_2(Br\text{-}Form)_2(dppn)_2]^{2+}$ complex which does not. It is hypothesized that this difference is due to the bromine substitution on the formamidinate ligands having a detrimental effect on cellular uptake. Similar to the work presented in Chapter II, a number of studies to compare and contrast these complexes, to investigate their mechanisms of cell death and to further understand their cellular uptake properties through octanol-water partition coefficient experiments and ICP-MS experiments are proposed.

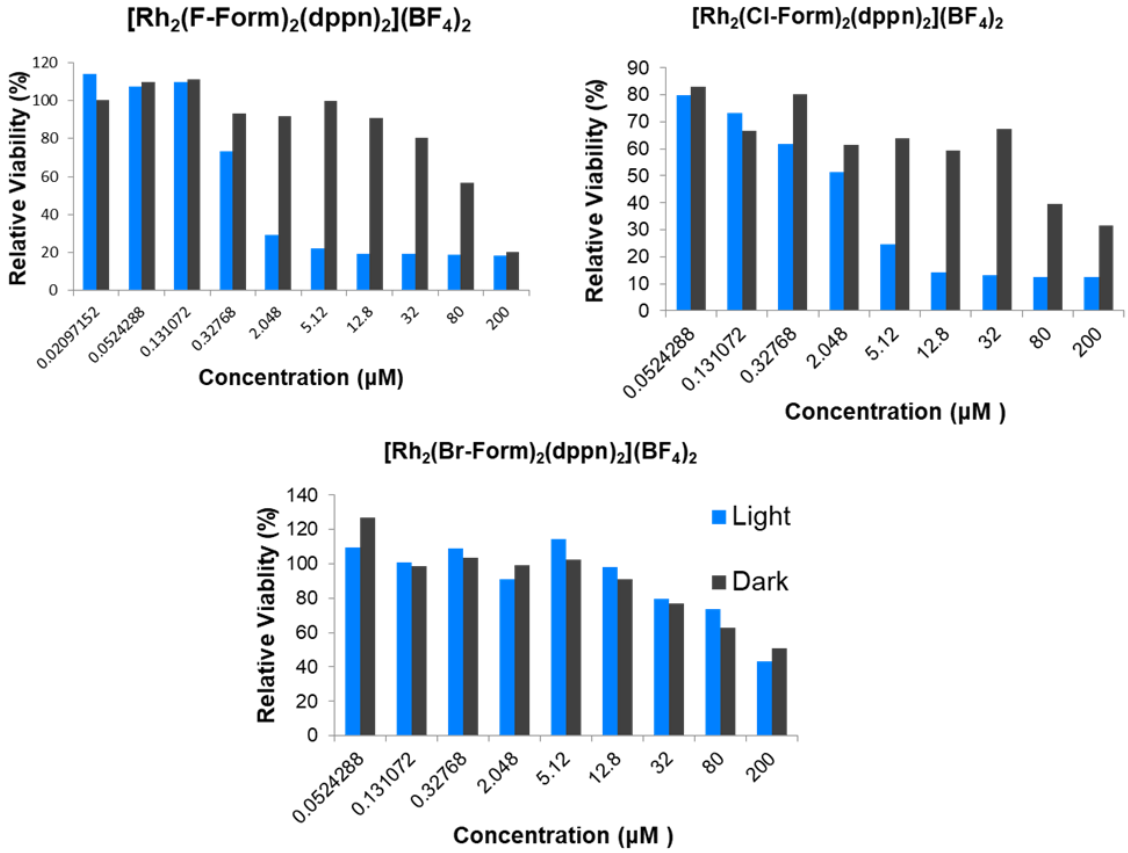


**Figure V.6** Resazurin cell viability results.

The work in Chapter IV focused on the exploration and expansion of the applications for dirhodium complexes by exploiting their tunable framework. Following the theme of altering the properties of dirhodium complexes through careful ligand selection and design, various carboxylate and ester functionalized ligands were synthesized for coordination with the dirhodium core. DSSC sensitizers need to exhibit chemical and thermal stability, strong absorption in the visible and near-IR region, and HOMO/LUMO energy levels that would allow charge transfer from the excited state of the compound to the semiconductor. They must also have peripheral anchoring groups to adsorb onto semiconductor surfaces. The new compounds described in this chapter were

inspired by complexes of general formula *cis*-$[Rh_2(DTolF)_2(L)_2][BF_4]_2$ (L = pynp, qnnp, and qxnp), which have red-shifted absorption profiles into the near-IR compared to the 1,8-naphthyridine analogue which does not absorb beyond 700 nm (ref). The excited states of these complexes are sufficiently oxidizing to transfer a hole to an electron donor such as *p*-phenylenediamine upon irradiation with low-energy light ($\lambda_{irr}$ = 600 nm). In the case of the pynp complex, the excited states are also capable of transferring an electron to the methyl viologen dication upon irradiation.[83] While promising, those complexes do not possess the functionality to be able to sensitize semiconductor materials. In this work, the compounds $[Rh_2(DTolF)_2(\mu\text{-}COOEt\text{-}L)_2][BF_4]_2$, (L= ethyl 2-(pyridin-2-yl)-1,8-naphthyridine-4-carboxylate (2COOEt-pynp), ethyl 2-(1,8-naphthyridin-2-yl)isonicotinate (4COOEt-pynp)), and $[Rh_2(COOEt\text{-}Form)_2(\mu\text{-}L)_2][BF_4]_2$ (COOEt-Form = N,N'-bis(4-ethoxycarbonylphenyl)-N'(benzylformamidinate) and (μ-L) = pynp, qnnp and qxnp) were synthesized and their absorption spectra, electrochemistry, and electronic structure and transitions were thoroughly investigated. Compounds of the type $[Rh_2(DTolF)_2(\mu\text{-}COOEt\text{-}L)_2][BF_4]_2$ were designed with electron injection and n-type sensitization in mind, while complexes of the type $[Rh_2(COOEt\text{-}Form)_2(\mu\text{-}L)_2][BF_4]_2$ are intended for p-type sensitization hole transfer. Ester functionalized ligands, which aprovide a more convenient platform for purification and characterization, can be hydrolyzed *in situ* to their respective carboxylate forms and be adsorbed onto $TiO_2$ or NiO. 1H-NMR, ESI-MS and X-ray crystallography confirmed the identity of the products. All five of these complexes have panchromic absorption and feature strong absorbance in the visible region. The compounds $[Rh_2(COOEt\text{-}Form)_2(pynp)_2][BF_4]_2$, $[Rh_2(COOEt$-

Form)$_2$(qnnp)$_2$][$BF_4$]$_2$ and [$Rh_2$(COOEt-Form)$_2$(qxnp)$_2$][$BF_4$]$_2$ do absorb far into the visible/near IR due to the electron withdrawing COOEt group on the formamidinate ligand. The structure-function correlations are also evidenced in the cyclic voltammetry experiments and supported by the DFT and TD-DFT calculations. Based on previous studies of dirhodium II,II complexes, the oxidation event for all of these complexes is assigned as an oxidation of the metal center. The multiple reversible or quasi-reversible reduction events are attributed to reductions of the coordinating ligands. In general, in the [$Rh_2$(COOEt-Form)$_2$(μ-L)$_2$][$BF_4$]$_2$, the more electron dense and conjugated qxnp ligands shifts the reduction potentials to less negative values. The lower energy transitions are computationally shown to involve primarily the HOMO or lower energy orbitals and LUMO or the LUMO+1. As such, the effect of the electron withdrawing substituents, or the conjugation of the axially blocking ligands has a pronounced effect on the molecular orbital energy levels. These calculations highlight the fact that these complexes have appropriate HOMO and LUMO energy levels for charge injection. Given that these complexes have been thoroughly investigated, it is of interest to adsorb them onto semiconductor materials and use them in the construction of DSSCs.

Owing to the added functionality of these dirhodium complexes due to the presence of the anchoring group, another area of interest and application for these complexes is as sensitizers for dye-sensitized photoelectrosynthesis cells (DSPEC).[146, 147] Similar to the principles of a DSSC, a DSPEC consists of a semiconducting layer onto which a chromophore catalyst assembly is anchored. Whereas the redox couple in a DSSC is typically iodide based, in a DSPEC it can be a substrate that undergoes a redox reaction

and yield a desirable product. While there are obstacles presented by the DSPEC approach, including synthetic challenges to make the chromophore catalyst assembly and careful selection of a robust catalyst with activity that can be accessed by chromophore oxidation, these cells are an exciting approach for the production of carbon-neutral fuels (ref). Ruthenium based assemblies are known for DSPECs, but as the criteria for the sensitizer are similar to that of DSSCs, dirhodium complexes constitute a promising potential alternative. To enhance the properties of these complexes for use as sensitizers in DSSCs and DSPECs, the theme of ligand field design and tuning can be applied to this area as well. Many types of anchoring groups other than carboxylates have been studied in sensitizers, such as phosphonic acid, tetrazole, sulfonic acid and nitro, among many others. Ligands that are capable of coordinating to dirhodium units can be designed to bear these functional groups which could lead to enhanced adsorption of the dye onto the semiconductor surface and also serve to tune the light absorption and redox activity of the complexes.

In summary, the dirhodium compounds reported herein demonstrate the importance of ligand design and the relevance of gaining insight into fundamental structural and electronic properties. The work presented in this dissertation serves to highlight methods by which new dirhodium complexes can be developed and how one can expand their applications into unexplored directions and new areas of research.

# REFERENCES


1. Cotton, F. A.; Curtis, N. F.; Harris, C. B.; Johnson, B. F. G.; Lippard, S. J.; Mague, J. T.; Robinson, W. R.; Wood, J. S., Mononuclear and Polynuclear Chemistry of Rhenium (III): Its Pronounced Homophilicity. *Science* **1964,** *145* (3638), 1305.

2. Cotton, F. A.; Harris, C. B., The Crystal and Molecular Structure of Dipotassium Octachlorodirhenate(III) Dihydrate, K2[Re2Cl8]2H2O. *Inorganic Chemistry* **1965,** *4* (3), 330-333.

3. Cotton, F. A.; Murillo, C. A.; Walton, R. A., *Multiple bonds between metal atoms. 3rd ed. edited by F. Albert Cotton, Carlos A. Murillo and Richard A. Walton*. New York : Springer Science and Business Media, Inc., 2005.
3rd ed.: 2005.

4. Berry, J. F.; Lu, C. C., Metal–Metal Bonds: From Fundamentals to Applications. *Inorganic Chemistry* **2017,** *56* (14), 7577-7581.

5. Katsaros, N.; Anagnostopoulou, A., Rhodium and its compounds as potential agents in cancer treatment. *Critical Reviews in Oncology/Hematology* **2002,** *42* (3), 297-308.

6. Doyle, M. P.; Forbes, D. C., Recent advances in asymmetric catalytic metal carbene transformations. *Chemical Reviews* **1998,** *98* (2), 911-935.

7. Davies, H. M. L.; Liao, K., Dirhodium tetracarboxylates as catalysts for selective intermolecular C–H functionalization. *Nature Reviews Chemistry* **2019,** *3* (6), 347-360.

8. Rizzi, G. A.; Casarin, M.; Tondello, E.; Piraino, P.; Granozzi, G., UV photoelectron spectra and DV-X.alpha. calculations on diatomic rhodium formamidinate complexes. *Inorganic Chemistry* **1987,** *26* (20), 3406-3409.

9. Boyar, E. B.; Robinson, S. D., Rhodium(II) carboxylates. *Coord. Chem. Rev.* **1983,** *50* (1), 109-208.

10. Warzecha, E.; Berto, T. C.; Wilkinson, C. C.; Berry, J. F., Rhodium Rainbow: A Colorful Laboratory Experiment Highlighting Ligand Field Effects of Dirhodium Tetraacetate. *J. Chem. Educ.* **2019,** *96* (3), 571-576.

11. Christoph, G. G.; Koh, Y. B., Metal-metal bonding in dirhodium tetracarboxylates. Trans influence and dependence of the rhodium-rhodium bond distance upon the nature of the axial ligands. *Journal of the American Chemical Society* **1979,** *101* (6), 1422-1434.

12. Paulissen, R.; Reimlinger, H.; Hayez, E.; Hubert, A. J.; Teyssié, P., Transition metal catalysed reactions of diazocompounds - II insertion in the hydroxylic bond. *Tetrahedron Lett.* **1973,** *14* (24), 2233-2236.

13. World Health Organization. Cancer. *https://www.who.int/news-room/fact-sheets/detail/cancer* (accessed November 1, 2021).

14. American Cancer Society. Cancer Facts and Statistics. *https://www.cancer.org/research/cancer-facts-statistics.html* (accessed October 29, 2021)

15. Miller, K. D.; Nogueira, L.; Mariotto, A. B.; Rowland, J. H.; Yabroff, K. R.; Alfano, C. M.; Jemal, A.; Kramer, J. L.; Siegel, R. L., Cancer treatment and

survivorship statistics, 2019. *CA: A Cancer Journal for Clinicians* **2019,** *69* (5), 363-385.

16. Lazebnik, Y., What are the hallmarks of cancer? *Nature Reviews Cancer* **2010,** *10* (4), 232-233.

17. Anand, P.; Kunnumakkara Ab Fau - Sundaram, C.; Sundaram C Fau - Harikumar, K. B.; Harikumar Kb Fau - Tharakan, S. T.; Tharakan St Fau - Lai, O. S.; Lai Os Fau - Sung, B.; Sung B Fau - Aggarwal, B. B.; Aggarwal, B. B., Cancer is a preventable disease that requires major lifestyle changes. (0724-8741 (Print)).

18. Mazumdar, M.; Glassman, J. R., Categorizing a prognostic variable: review of methods, code for easy implementation and applications to decision-making about cancer treatments. *Stat. Med.* **2000,** *19* (1), 113-132.

19. Franz, K. J.; Metzler-Nolte, N., Introduction: Metals in Medicine. *Chemical Reviews* **2019,** *119* (2), 727-729.

20. Desoize, B., Metals and Metal Compounds in Cancer Treatment. *Anticancer Res.* **2004,** *24* (3A), 1529.

21. Rosenberg, B.; Van Camp, L.; Krigas, T., Inhibition of Cell Division in Escherichia coli by Electrolysis Products from a Platinum Electrode. *Nature* **1965,** *205*, 698.

22. Rosenberg, B.; Vancamp, L.; Trosko, J. E.; Mansour, V. H., Platinum Compounds: a New Class of Potent Antitumour Agents. *Nature* **1969,** *222*, 385.

23. Johnstone, T. C.; Suntharalingam, K.; Lippard, S. J., The Next Generation of Platinum Drugs: Targeted Pt(II) Agents, Nanoparticle Delivery, and Pt(IV) Prodrugs. *Chemical reviews* **2016,** *116* (5), 3436-3486.

24. Todd, R. C.; Lippard, S. J., Structure of duplex DNA containing the cisplatin 1,2-{Pt(NH3)2}2+-d(GpG) cross-link at 1.77Å resolution. *Journal of Inorganic Biochemistry* **2010,** *104* (9), 902-908.

25. Takahara, P. M.; Rosenzweig, A. C.; Frederick, C. A.; Lippard, S. J., Crystal structure of double-stranded DNA containing the major adduct of the anticancer drug cisplatin. *Nature* **1995,** *377* (6550), 649-652.

26. Kelland, L., The resurgence of platinum-based cancer chemotherapy. *Nature Reviews Cancer* **2007,** *7* (8), 573-584.

27. Alberts, D. S.; Dorr, R. T., New Perspectives on an Old Friend: Optimizing Carboplatin for the Treatment of Solid Tumors. (1549-490X (Electronic)).

28. Shimada, M.; Itamochi H Fau - Kigawa, J.; Kigawa, J., Nedaplatin: a cisplatin derivative in cancer chemotherapy. **2013,** (1179-1322 (Print)).

29. Guo, Z.; Sadler, P. J., Metals in Medicine. *Angew. Chem. Int. Ed.* **1999,** *38* (11), 1512-1531.

30. Guo, M.; Sun, H.; McArdle, H. J.; Gambling, L.; Sadler, P. J., TiIV Uptake and Release by Human Serum Transferrin and Recognition of TiIV-Transferrin by Cancer Cells: Understanding the Mechanism of Action of the Anticancer Drug Titanocene Dichloride. *Biochemistry* **2000,** *39* (33), 10023-10033.

31. Levina, A.; Mitra, A.; Lay, P. A., Recent developments in ruthenium anticancer drugs. *Metallomics* **2009,** *1* (6), 458-470.

32. Onodera, T.; Momose, I.; Kawada, M., Potential Anticancer Activity of Auranofin. *Chemical and Pharmaceutical Bulletin* **2019,** *67* (3), 186-191.

33. Bear Jl Fau - Gray, H. B., Jr.; Gray Hb Jr Fau - Rainen, L.; Rainen L Fau - Chang, I. M.; Chang Im Fau - Howard, R.; Howard R Fau - Serio, G.; Serio G Fau - Kimball, A. P.; Kimball, A. P., Interaction of Rhodium(II) carboxylates with molecules of biologic importance. (0069-0112 (Print)).

34. Erck, A.; Rainen, L.; Whileyman, J.; Chang, I. M.; Kimball, A. P.; Bear, J., Studies of Rhodium(II) Carboxylates as Potential Antitumor Agents. *Proceedings of the Society for Experimental Biology and Medicine* **1974,** *145* (4), 1278-1283.

35. Howard, R. A.; Sherwood, E.; Erck, A.; Kimball, A. P.; Bear, J. L., Hydrophobicity of several rhodium(II) carboxylates correlated with their biologic activity. *Journal of Medicinal Chemistry* **1977,** *20* (7), 943-946.

36. Howard, R. A.; Spring, T. G.; Bear, J. L., The Interaction of Rhodium(II) Carboxylates with Enzymes. *Cancer Research* **1976,** *36* (12), 4402.

37. Chifotides, H. T.; Dunbar, K. R., Interactions of Metal−Metal-Bonded Antitumor Active Complexes with DNA Fragments and DNA. *Accounts of Chemical Research* **2005,** *38* (2), 146-156.

38. Chifotides, H. T.; Koshlap, K. M.; Pérez, L. M.; Dunbar, K. R., Unprecedented Head-to-Head Conformers of d(GpG) Bound to the Antitumor Active Compound

Tetrakis (μ-carboxylato)dirhodium(II,II). *Journal of the American Chemical Society* **2003,** *125* (35), 10703-10713.

39. Chifotides, H. T.; Koshlap, K. M.; Pérez, L. M.; Dunbar, K. R., Novel Binding Interactions of the DNA Fragment d(pGpG) Cross-Linked by the Antitumor Active Compound Tetrakis(μ-carboxylato)dirhodium(II,II). *Journal of the American Chemical Society* **2003,** *125* (35), 10714-10724.

40. Kang, M.; Chifotides, H. T.; Dunbar, K. R., 2D NMR Study of the DNA Duplex d(CTCTC*A*ACTTCC)·d(GGAAGTTGAGAG) Cross-Linked by the Antitumor-Active Dirhodium(II,II) Unit at the Cytosine−Adenine Step. *Biochemistry* **2008,** *47* (8), 2265-2276.

41. Chifotides, H. T.; Dunbar, K. R., Unprecedented Head-to-Head Right-Handed Cross-Links between the Antitumor Bis(μ-N,N‘-di-p-tolylformamidinate) Dirhodium(II,II) Core and the Dinucleotide d(ApA) with the Adenine Bases in the Rare Imino Form. *Journal of the American Chemical Society* **2007,** *129* (41), 12480-12490.

42. Chifotides, H. T.; Dunbar, K. R., Head-to-Head Right-Handed Cross-Links of the Antitumor-Active Bis( μ -N,N′ -di-p-tolylformamidinato)dirhodium(II,II) Unit with the Dinucleotides d(GpA) and d(ApG). *Chemistry – A European Journal* **2008,** *14* (32), 9902-9913.

43. Fimiani, V.; Ainis, T.; Cavallaro, A.; Piraino, P., Antitumor Effect of the New Rhodium(II) Complex: Rh2 (Form)2 (02 CCF3)2 (H20)2 (Form = N,N’-di-p-tolylformamidinate). *Journal of Chemotherapy* **1990,** *2* (5), 319-326.

44. Angeles-Boza, A. M.; Bradley, P. M.; Fu, P. K. L.; Wicke, S. E.; Bacsa, J.; Dunbar, K. R.; Turro, C., DNA Binding and Photocleavage in Vitro by New Dirhodium(II) dppz Complexes: Correlation to Cytotoxicity and Photocytotoxicity. *Inorganic Chemistry* **2004,** *43* (26), 8510-8519.

45. Angeles-Boza, A. M.; Chifotides, H. T.; Aguirre, J. D.; Chouai, A.; Fu, P. K. L.; Dunbar, K. R.; Turro, C., Dirhodium(II,II) Complexes: Molecular Characteristics that Affect in Vitro Activity. *Journal of Medicinal Chemistry* **2006,** *49* (23), 6841-6847.

46. Dolmans, D. E. J. G. J.; Fukumura, D.; Jain, R. K., Photodynamic therapy for cancer. *Nature Reviews Cancer* **2003,** *3*, 380.

47. Moan, J.; Peng, Q., An outline of the history of PDT. In *Photodynamic Therapy*, Patrice, T., Ed. The Royal Society of Chemistry: 2003; Vol. 2, pp 1-18.

48. Juarranz, Á.; Jaén, P.; Sanz-Rodríguez, F.; Cuevas, J.; González, S., Photodynamic therapy of cancer. Basic principles and applications. *Clinical and Translational Oncology* **2008,** *10* (3), 148-154.

49. Kwiatkowski, S.; Knap, B.; Przystupski, D.; Saczko, J.; Kędzierska, E.; Knap-Czop, K.; Kotlińska, J.; Michel, O.; Kotowski, K.; Kulbacka, J., Photodynamic therapy – mechanisms, photosensitizers and combinations. *Biomed. Pharmacother.* **2018,** *106*, 1098-1107.

50. Tampa, M.; Sarbu, M.-I.; Matei, C.; Mitran, C.-I.; Mitran, M.-I.; Caruntu, C.; Constantin, C.; Neagu, M.; Georgescu, S.-R., Photodynamic therapy: A hot topic in dermato-oncology (Review). *Oncol. Lett.* **2019,** *17* (5), 4085-4093.

51. Zhu, T. C.; Finlay, J. C., The role of photodynamic therapy (PDT) physics. *Med. Phys.* **2008,** *35* (7), 3127-3136.

52. Knoll, J. D.; Turro, C., Control and utilization of ruthenium and rhodium metal complex excited states for photoactivated cancer therapy. *Coord Chem Rev* **2015,** *282-283*, 110-126.

53. Farrer, N. J.; Salassa, L.; Sadler, P. J., Photoactivated chemotherapy (PACT): the potential of excited-state d-block metals in medicine. *Dalton transactions (Cambridge, England : 2003)* **2009,** (48), 10690-10701.

54. Schweitzer, V. G., PHOTOFRIN-mediated photodynamic therapy for treatment of early stage oral cavity and laryngeal malignancies*. *Lasers Surg. Med.* **2001,** *29* (4), 305-313.

55. Lang, K.; Schulte, K. W.; Ruzicka, T.; Fritsch, C., Aminolevulinic acid (Levulan) in photodynamic therapy of actinic keratoses. *Skin Therapy Lett.* **2001,** *6* (10), 1-2, 5.

56. Bradley, P. M.; Bursten, B. E.; Turro, C., Excited-State Properties of Rh2(O2CCH3)4(L)2 (L = CH3OH, THF, PPh3, py). *Inorganic Chemistry* **2001,** *40* (6), 1376-1379.

57. Fu, P. K. L.; Bradley, P. M.; Turro, C., DNA Cleavage by Photogenerated Rh2(O2CCH3)4(H2O)2+. *Inorganic Chemistry* **2001,** *40* (11), 2476-2477.

58. Li, Z.; David, A.; Albani, B. A.; Pellois, J.-P.; Turro, C.; Dunbar, K. R., Optimizing the Electronic Properties of Photoactive Anticancer Oxypyridine-Bridged

Dirhodium(II,II) Complexes. *Journal of the American Chemical Society* **2014,** *136* (49), 17058-17070.

59. Aguirre, J. D.; Angeles-Boza, A. M.; Chouai, A.; Pellois, J.-P.; Turro, C.; Dunbar, K. R., Live Cell Cytotoxicity Studies: Documentation of the Interactions of Antitumor Active Dirhodium Compounds with Nuclear DNA. *Journal of the American Chemical Society* **2009,** *131* (32), 11353-11360.

60. Gielen, D.; Boshell, F.; Saygin, D.; Bazilian, M. D.; Wagner, N.; Gorini, R., The role of renewable energy in the global energy transformation. *Energy Strategy Reviews* **2019,** *24*, 38-50.

61. U.S. Energy Information Administration. U.S. Energy facts explained. *https://www.eia.gov/energyexplained/us-energy-facts/* (accessed November 3, 2021)

62. Morton, O., A new day dawning?: Silicon Valley sunrise. *Nature* **2006,** *443* (7107), 19-22.

63. Sampaio, P. G. V.; González, M. O. A., Photovoltaic solar energy: Conceptual framework. *Renewable and Sustainable Energy Reviews* **2017,** *74*, 590-601.

64. Todorov, T. K.; Singh, S.; Bishop, D. M.; Gunawan, O.; Lee, Y. S.; Gershon, T. S.; Brew, K. W.; Antunez, P. D.; Haight, R., Ultrathin high band gap solar cells with improved efficiencies from the world's oldest photovoltaic material. *Nature Communications* **2017,** *8* (1), 682.

65. Green Martin, A.; Hishikawa, Y.; Warta, W.; Dunlop Ewan, D.; Levi Dean, H.; Hohl‐Ebinger, J.; Ho‐Baillie Anita, W. H., Solar cell efficiency tables (version 50). *Progress in Photovoltaics: Research and Applications* **2017,** *25* (7), 668-676.

66. Andreani, L. C.; Bozzola, A.; Kowalczewski, P.; Liscidini, M.; Redorici, L., Silicon solar cells: toward the efficiency limits. *Advances in Physics: X* **2019,** *4* (1), 1548305.

67. Grätzel, M., Dye-sensitized solar cells. *Journal of Photochemistry and Photobiology C: Photochemistry Reviews* **2003,** *4* (2), 145-153.

68. Nazeeruddin, M. K.; Péchy, P.; Renouard, T.; Zakeeruddin, S. M.; Humphry-Baker, R.; Comte, P.; Liska, P.; Cevey, L.; Costa, E.; Shklover, V.; Spiccia, L.; Deacon, G. B.; Bignozzi, C. A.; Grätzel, M., Engineering of Efficient Panchromatic Sensitizers for Nanocrystalline TiO2-Based Solar Cells. *Journal of the American Chemical Society* **2001,** *123* (8), 1613-1624.

69. O'Regan, B.; Grätzel, M., A low-cost, high-efficiency solar cell based on dye-sensitized colloidal TiO2 films. *Nature* **1991,** *353* (6346), 737-740.

70. Kalyanasundaram, K., *Dye-sensitized solar cells. edited by K. Kalyanasundaram*. Boca Raton, Fla. : CRC Press, [2010]: 2010.

71. Kushwaha, R.; Srivastava, P.; Bahadur, L., *Natural Pigments from Plants Used as Sensitizers for TiO2 Based Dye-Sensitized Solar Cells*. 2013; Vol. 2013, p 1-8.

72. Carella, A.; Borbone, F.; Centore, R., Research Progress on Photosensitizers for DSSC. *Frontiers in Chemistry* **2018,** *6* (481).

73. Sharma, K.; Sharma, V.; Sharma, S. S., Dye-Sensitized Solar Cells: Fundamentals and Current Status. *Nanoscale Research Letters* **2018,** *13* (1), 381.

74. Wood, C. J.; Summers, G. H.; Clark, C. A.; Kaeffer, N.; Braeutigam, M.; Carbone, L. R.; D'Amario, L.; Fan, K.; Farré, Y.; Narbey, S.; Oswald, F.; Stevens, L.

A.; Parmenter, C. D. J.; Fay, M. W.; La Torre, A.; Snape, C. E.; Dietzek, B.; Dini, D.; Hammarström, L.; Pellegrin, Y.; Odobel, F.; Sun, L.; Artero, V.; Gibson, E. A., A comprehensive comparison of dye-sensitized NiO photocathodes for solar energy conversion. *Physical Chemistry Chemical Physics* **2016,** *18* (16), 10727-10738.

75. Bai, Y.; Mora-Seró, I.; De Angelis, F.; Bisquert, J.; Wang, P., Titanium Dioxide Nanomaterials for Photovoltaic Applications. *Chemical Reviews* **2014,** *114* (19), 10095-10130.

76. Roy, P.; Kim, D.; Lee, K.; Spiecker, E.; Schmuki, P., TiO2 nanotubes and their application in dye-sensitized solar cells. *Nanoscale* **2010,** *2* (1), 45-59.

77. Song, H.; Tang, W.; Zhao, S.; Liu, Q.; Xie, Y., Porphyrin sensitizers containing an auxiliary benzotriazole acceptor for dye-sensitized solar cells: Effects of steric hindrance and cosensitization. *Dyes and Pigments* **2018,** *155*, 323-331.

78. Wang, G.; Liu, Z.; Deng, Y.; Xie, L.; Tan, S., Comparative study on N,N-di-p-tolylaniline-based D-π-A1-π-A2 sensitizers by tuning the auxiliary acceptor for dye-sensitized solar cells. *Dyes and Pigments* **2017,** *145*, 427-435.

79. Meier, H., Conjugated Oligomers with Terminal Donor–Acceptor Substitution. *Angew. Chem. Int. Ed.* **2005,** *44* (17), 2482-2506.

80. Ferrere, S.; Zaban, A.; Gregg, B. A., Dye Sensitization of Nanocrystalline Tin Oxide by Perylene Derivatives. *The Journal of Physical Chemistry B* **1997,** *101* (23), 4490-4493.

81. Tomar, N.; Agrawal, A.; Dhaka, V. S.; Surolia, P. K., Ruthenium complexes based dye sensitized solar cells: Fundamentals and research trends. *Solar Energy* **2020,** *207*, 59-76.

82. Nazeeruddin, M. K.; Kay, A.; Rodicio, I.; Humphry-Baker, R.; Mueller, E.; Liska, P.; Vlachopoulos, N.; Graetzel, M., Conversion of light to electricity by cis-X2bis(2,2'-bipyridyl-4,4'-dicarboxylate)ruthenium(II) charge-transfer sensitizers (X = Cl-, Br-, I-, CN-, and SCN-) on nanocrystalline titanium dioxide electrodes. *Journal of the American Chemical Society* **1993,** *115* (14), 6382-6390.

83. Whittemore, T. J.; Millet, A.; Sayre, H. J.; Xue, C.; Dolinar, B. S.; White, E. G.; Dunbar, K. R.; Turro, C., Tunable Rh2(II,II) Light Absorbers as Excited-State Electron Donors and Acceptors Accessible with Red/Near-Infrared Irradiation. *Journal of the American Chemical Society* **2018,** *140* (15), 5161-5170.

84. Millet, A.; Xue, C.; Song, E.; Turro, C.; Dunbar, K. R., Synthetic Strategies for Trapping the Elusive trans-Dirhodium(II,II) Formamidinate Isomer: Effects of Cis versus Trans Geometry on the Photophysical Properties. *Inorganic Chemistry* **2020,** *59* (4), 2255-2265.

85. Aoki, K.; Salam, M. A., Interligand interactions affecting specific metal bonding to nucleic acid bases. A case of [Rh2(OAc)4], [Rh2(HNOCCF3)4], and [Rh2(OAc)2(HNOCCF3)2] toward purine nucleobases and nucleosides. *Inorganica Chimica Acta* **2002,** *339*, 427-437.

86. Joyce, L. E.; Aguirre, J. D.; Angeles-Boza, A. M.; Chouai, A.; Fu, P. K.; Dunbar, K. R.; Turro, C., Photophysical properties, DNA photocleavage, and

photocytotoxicity of a series of dppn dirhodium(II,II) complexes. *Inorg Chem* **2010,** *49* (12), 5371-6.

87. Albani, B. A.; Peña, B.; Leed, N. A.; de Paula, N. A. B. G.; Pavani, C.; Baptista, M. S.; Dunbar, K. R.; Turro, C., Marked Improvement in Photoinduced Cell Death by a New Tris-heteroleptic Complex with Dual Action: Singlet Oxygen Sensitization and Ligand Dissociation. *Journal of the American Chemical Society* **2014,** *136* (49), 17095-17101.

88. Burya, S. J.; Palmer, A. M.; Gallucci, J. C.; Turro, C., Photoinduced Ligand Exchange and Covalent DNA Binding by Two New Dirhodium Bis-Amidato Complexes. *Inorganic Chemistry* **2012,** *51* (21), 11882-11890.

89. Akhimie, R. N.; White, J. K.; Turro, C., Dual photoreactivity of a new Rh2(II,II) complex for biological applications. *Inorganica Chimica Acta* **2017,** *454*, 149-154.

90. Bradley, W.; Wright, I., 129. Metal derivatives of NN[prime or minute]-diarylamidines. *Journal of the Chemical Society (Resumed)* **1956,** (0), 640-648.

91. Che, G.; Li, W.; Kong, Z.; Su, Z.; Chu, B.; Li, B.; Zhang, Z.; Hu, Z.; Chi, H., Hydrothermal Syntheses of Some Derivatives of Tetraazatriphenylene. *Synth. Commun.* **2006,** *36* (17), 2519-2524.

92. Fulmer, G. R.; Miller, A. J. M.; Sherden, N. H.; Gottlieb, H. E.; Nudelman, A.; Stoltz, B. M.; Bercaw, J. E.; Goldberg, K. I., NMR Chemical Shifts of Trace Impurities: Common Laboratory Solvents, Organics, and Gases in Deuterated Solvents Relevant to the Organometallic Chemist. *Organometallics* **2010,** *29* (9), 2176-2179.

93. Sheldrick, G. M., SADABS. University of Gottingen: Germany, 1996.

94. Sheldrick, G., Crystal structure refinement with SHELXL. *Acta Cryst. C* **2015,** *71* (1), 3-8.

95. M. J. Frisch, G. T., W.; Schlegel, H. B.; Scuseria, G. E.; Robb, M. A.; Cheeseman, J. R.; Scalmani, G.; Barone, V.; Mennucci, B.; Petersson, G. A.; Nakatsuji, H.; Caricato, M.; Li, X.; Hratchian, H. P.; Izmaylov, A. F.; Bloino, J.; Zheng, G.; Sonnenberg, J.L. , *Gaussian16* **2016,** *Gaussian, Inc* (Wallingford, CT).

96. Adamo, C.; Barone, V., Exchange functionals with improved long-range behavior and adiabatic connection methods without adjustable parameters: The mPW and mPW1PW models. *The Journal of Chemical Physics* **1998,** *108* (2), 664-675.

97. Perdew, J. P.; Burke, K.; Wang, Y., Generalized gradient approximation for the exchange-correlation hole of a many-electron system. *Physical Review B* **1996,** *54* (23), 16533-16539.

98. Perdew, J. P.; Chevary, J. A.; Vosko, S. H.; Jackson, K. A.; Pederson, M. R.; Singh, D. J.; Fiolhais, C., Atoms, molecules, solids, and surfaces: Applications of the generalized gradient approximation for exchange and correlation. *Physical Review B* **1992,** *46* (11), 6671-6687.

99. Dolg, M.; Stoll, H.; Preuss, H.; Pitzer, R. M., Relativistic and correlation effects for element 105 (hahnium, Ha): a comparative study of M and MO (M = Nb, Ta, Ha) using energy-adjusted ab initio pseudopotentials. *The Journal of Physical Chemistry* **1993,** *97* (22), 5852-5859.

100. Petersson, G. A.; Al‐Laham, M. A., A complete basis set model chemistry. II. Open‐shell systems and the total energies of the first‐row atoms. *The Journal of Chemical Physics* **1991,** *94* (9), 6081-6090.

101. Tomasi, J.; Mennucci, B.; Cammi, R., Quantum Mechanical Continuum Solvation Models. *Chemical Reviews* **2005,** *105* (8), 2999-3094.

102. Leonid, S., *Chemissian 1.7* **2005-2010**.

103. Rohrabaugh, T. N.; Collins, K. A.; Xue, C.; White, J. K.; Kodanko, J. J.; Turro, C., New Ru(ii) complex for dual photochemotherapy: release of cathepsin K inhibitor and 1O2 production. *Dalton Transactions* **2018,** *47* (34), 11851-11858.

104. Warren, J. T.; Chen, W.; Johnston, D. H.; Turro, C., Ground-State Properties and Excited-State Reactivity of 8-Quinolate Complexes of Ruthenium(II). *Inorganic Chemistry* **1999,** *38* (26), 6187-6192.

105. Knoll, J. D.; Albani, B. A.; Turro, C., Excited state investigation of a new Ru(ii) complex for dual reactivity with low energy light. *Chemical Communications* **2015,** *51* (42), 8777-8780.

106. Knoll, J. D.; Albani, B. A.; Turro, C., New Ru(II) Complexes for Dual Photoreactivity: Ligand Exchange and 1O2 Generation. *Accounts of Chemical Research* **2015,** *48* (8), 2280-2287.

107. Howard, R. A.; Kimball, A. P.; Bear, J. L., Mechanism of Action of Tetra-μ-carboxylatodirhodium(II) in L1210 Tumor Suspension Culture. *Cancer Research* **1979,** *39* (7 Part 1), 2568.

108. Etayo, P.; Vidal-Ferran, A., Rhodium-catalysed asymmetric hydrogenation as a valuable synthetic tool for the preparation of chiral drugs. *Chemical Society Reviews* **2013,** *42* (2), 728-754.

109. Chavan, M. Y.; Ahsan, M. Q.; Lifsey, R. S.; Bear, J. L.; Kadish, K. M., Reversible carbon monoxide binding by Rh2(O2CCH3)n(HNOCCH3)4-n. A spectroscopic and electrochemical investigation. *Inorganic Chemistry* **1986,** *25* (18), 3218-3223.

110. Chavan, M. Y.; Zhu, T. P.; Lin, X. Q.; Ahsan, M. Q.; Bear, J. L.; Kadish, K. M., Axial-ligand-dependent electrochemical and spectral properties of a series of acetate- and acetamidate-bridged dirhodium complexes. *Inorganic Chemistry* **1984,** *23* (26), 4538-4545.

111. Li, Z.; Leed, N. A.; Dickson-Karn, N. M.; Dunbar, K. R.; Turro, C., Directional charge transfer and highly reducing and oxidizing excited states of new dirhodium(ii,ii) complexes: potential applications in solar energy conversion. *Chem. Sci.* **2014,** *5* (2), 727-737.

112. Lutterman, D. A.; Fu, P. K. L.; Turro, C., cis-[Rh2(μ-O2CCH3)2(CH3CN)6]2+ as a Photoactivated Cisplatin Analog. *Journal of the American Chemical Society* **2006,** *128* (3), 738-739.

113. Catalan, K. V.; Mindiola, D. J.; Ward, D. L.; Dunbar, K. R., A Novel Dirhodium Compound with Neutral, Bridging 9-Ethyladenine Ligands. *Inorganic Chemistry* **1997,** *36* (11), 2458-2460.

114. Martin, D. S.; Webb, T. R.; Robbins, G. A.; Fanwick, P. E., Polarized electronic absorption spectra for dirhodium(II) tetraacetate dihydrate. *Inorganic Chemistry* **1979,** *18* (2), 475-478.

115. Li, Z.; Chifotides, H. T.; Dunbar, K. R., Unprecedented partial paddlewheel dirhodium methyl isocyanide compounds with unusual structural and electronic properties: a comprehensive experimental and theoretical study. *Chemical Science* **2013,** *4* (12), 4470-4485.

116. Kudo, A.; Miseki, Y., Heterogeneous photocatalyst materials for water splitting. *Chemical Society Reviews* **2009,** *38* (1), 253-278.

117. van de Krol, R.; Liang, Y.; Schoonman, J., Solar hydrogen production with nanostructured metal oxides. *J. Mater. Chem.* **2008,** *18* (20), 2311-2320.

118. Bolton, J. R., Photochemical conversion and storage of solar energy. *J. Solid State Chem.* **1977,** *22* (1), 3-8.

119. McKone, J. R.; Lewis, N. S.; Gray, H. B., Will Solar-Driven Water-Splitting Devices See the Light of Day? *Chem. Mater.* **2014,** *26* (1), 407-414.

120. Ma, Y.; Wang, X.; Jia, Y.; Chen, X.; Han, H.; Li, C., Titanium Dioxide-Based Nanomaterials for Photocatalytic Fuel Generations. *Chemical Reviews* **2014,** *114* (19), 9987-10043.

121. Ladomenou, K.; Kitsopoulos, T. N.; Sharma, G. D.; Coutsolelos, A. G., The importance of various anchoring groups attached on porphyrins as potential dyes for DSSC applications. *RSC Advances* **2014,** *4* (41), 21379-21404.

122. Lee, C.-P.; Li, C.-T.; Ho, K.-C., Use of organic materials in dye-sensitized solar cells. *Mater. Today* **2017,** *20* (5), 267-283.

123. Schmidt‐Mende, L.; Campbell Wayne, M.; Wang, Q.; Jolley Kenneth, W.; Officer David, L.; Nazeeruddin Md, K.; Grätzel, M., Zn‐Porphyrin‐Sensitized Nanocrystalline TiO2 Heterojunction Photovoltaic Cells. *Chemphyschem* **2005,** *6* (7), 1253-1258.

124. Swetha, T.; Reddy, K. R.; Singh Surya, P., Osmium Polypyridyl Complexes and Their Applications to Dye‐Sensitized Solar Cells. *The Chemical Record* **2015,** *15* (2), 457-474.

125. Wang, J.; Li, C.; Wong, W.-L.; Chow, C.-F., Novel Iron-Based Polynuclear Metal Complexes [FeII(L)(CN)4]2–[FeIII(H2O)3Cl]2: Synthesis and Study of Photovoltaic Properties for Dye-Sensitized Solar Cell. *Russ. J. Electrochem.* **2018,** *54* (12), 1164-1175.

126. Colombo, A.; Dragonetti, C.; Fagnani, F.; Roberto, D.; Melchiorre, F.; Biagini, P., Improving the efficiency of copper-dye-sensitized solar cells by manipulating the electrolyte solution. *Dalton Transactions* **2019,** *48* (26), 9818-9823.

127. Chiang, T. L.; Chou, C. S.; Wu, D. H.; Hsiung, C. M., Applications of P-Type NiO in Dye-Sensitized Solar Cells. *Advanced Materials Research* **2011,** *239-242*, 1747-1750.

128. Brisse, R.; Praveen, C.; Maffeis, V.; Bourgeteau, T.; Tondelier, D.; Berthelot, T.; Geffroy, B.; Gustavsson, T.; Raimundo, J. M.; Jousselme, B., A red to blue series

of push–pull dyes for NiO based p-DSSCs. *Sustainable Energy & Fuels* **2018,** *2* (3), 648-654.

129. Klfout, H.; Stewart, A.; Elkhalifa, M.; He, H., BODIPYs for Dye-Sensitized Solar Cells. *ACS Applied Materials & Interfaces* **2017,** *9* (46), 39873-39889.

130. Saravanan, V.; Ganesan, S.; Rajakumar, P., Synthesis and DSSC application of BODIPY decorated triazole bridged and benzene nucleus cored conjugated dendrimers. *RSC Advances* **2020,** *10* (31), 18390-18399.

131. Whittemore, T. J.; Sayre, H. J.; Xue, C.; White, T. A.; Gallucci, J. C.; Turro, C., New Rh2(II,II) Complexes for Solar Energy Applications: Panchromatic Absorption and Excited-State Reactivity. *Journal of the American Chemical Society* **2017,** *139* (41), 14724-14732.

132. Kukrek, A.; Wang, D.; Hou, Y.; Zong, R.; Thummel, R., Photosensitizers Containing the 1,8-Naphthyridyl Moiety and Their Use in Dye-Sensitized Solar Cells. *Inorganic Chemistry* **2006,** *45* (25), 10131-10137.

133. Ashford, D. L.; Gish, M. K.; Vannucci, A. K.; Brennaman, M. K.; Templeton, J. L.; Papanikolas, J. M.; Meyer, T. J., Molecular Chromophore–Catalyst Assemblies for Solar Fuel Applications. *Chemical Reviews* **2015,** *115* (23), 13006-13049.

134. Ashford, D. L.; Glasson, C. R. K.; Norris, M. R.; Concepcion, J. J.; Keinan, S.; Brennaman, M. K.; Templeton, J. L.; Meyer, T. J., Controlling Ground and Excited State Properties through Ligand Changes in Ruthenium Polypyridyl Complexes. *Inorganic Chemistry* **2014,** *53* (11), 5637-5646.

135. Aguirre, J. D.; Lutterman, D. A.; Angeles-Boza, A. M.; Dunbar, K. R.; Turro, C., Effect of Axial Coordination on the Electronic Structure and Biological Activity of Dirhodium(II,II) Complexes. *Inorganic Chemistry* **2007,** *46* (18), 7494-7502.

136. Zhu, T. P.; Ahsan, M. Q.; Malinski, T.; Kadish, K. M.; Bear, J. L., Electrochemical studies of a series of dirhodium(II) complexes with acetate and acetamidate bridging ligands. *Inorganic Chemistry* **1984,** *23* (1), 2-3.

137. Ren, T.; Lin, C.; Valente, E. J.; Zubkowski, J. D., The influence of remote substituent in tetrakis( μ -N,N′ -diarylformamidinato) ‑ dirhodium(II) compounds. Part 7. Linear free energy relationships in dinuclear compounds. *Inorganica Chimica Acta* **2000,** *297* (1), 283-290.

138. Campos-Fernández, C. S.; Thomson, L. M.; Galán-Mascarós, J. R.; Ouyang, X.; Dunbar, K. R., Homologous Series of Redox-Active, Dinuclear Cations [M2(O2CCH3)2(pynp)2]2+ (M = Mo, Ru, Rh) with the Bridging Ligand 2-(2-Pyridyl)-1,8-naphthyridine (pynp). *Inorganic Chemistry* **2002,** *41* (6), 1523-1533.

139. Inoue, M.; Sumii, Y.; Shibata, N., Contribution of Organofluorine Compounds to Pharmaceuticals. *ACS Omega* **2020,** *5* (19), 10633-10640.

140. Zhou, Y.; Wang, J.; Gu, Z.; Wang, S.; Zhu, W.; Aceña, J. L.; Soloshonok, V. A.; Izawa, K.; Liu, H., Next Generation of Fluorine-Containing Pharmaceuticals, Compounds Currently in Phase II–III Clinical Trials of Major Pharmaceutical Companies: New Structural Trends and Therapeutic Areas. *Chemical Reviews* **2016,** *116* (2), 422-518.

141. Chen, S.-H.; Chang, J.-Y., New Insights into Mechanisms of Cisplatin Resistance: From Tumor Cell to Microenvironment. *Int. J. Mol. Sci.* **2019,** *20* (17).

142. Shen, D.-W.; Pouliot, L. M.; Hall, M. D.; Gottesman, M. M., Cisplatin Resistance: A Cellular Self-Defense Mechanism Resulting from Multiple Epigenetic and Genetic Changes. *Pharmacol. Rev.* **2012,** *64* (3), 706.

143. Medina, M. A.; Oza, G.; Sharma, A.; Arriaga, L. G.; Hernández Hernández, J. M.; Rotello, V. M.; Ramirez, J. T., Triple-Negative Breast Cancer: A Review of Conventional and Advanced Therapeutic Strategies. *Int. J. Environ. Res. Public Health* **2020,** *17* (6).

144. Smith, R. C.; Tennyson, A. G.; Lippard, S. J., Polymer-Bound Dirhodium Tetracarboxylate Films for Fluorescent Detection of Nitric Oxide. *Inorganic Chemistry* **2006,** *45* (16), 6222-6226.

145. Pena, B.; Barhoumi, R.; Burghardt, R. C.; Turro, C.; Dunbar, K. R., Confocal fluorescence microscopy studies of a fluorophore-labeled dirhodium compound: visualizing metal-metal bonded molecules in lung cancer (A549) cells. *J Am Chem Soc* **2014,** *136* (22), 7861-4.

146. Wang, D.; Niu, F.; Mortelliti, M. J.; Sheridan, M. V.; Sherman, B. D.; Zhu, Y.; McBride, J. R.; Dempsey, J. L.; Shen, S.; Dares, C. J.; Li, F.; Meyer, T. J., A stable dye-sensitized photoelectrosynthesis cell mediated by a NiO overlayer for water oxidation. *Proceedings of the National Academy of Sciences* **2020,** *117* (23), 12564.

147. Brennaman, M. K.; Dillon, R. J.; Alibabaei, L.; Gish, M. K.; Dares, C. J.; Ashford, D. L.; House, R. L.; Meyer, G. J.; Papanikolas, J. M.; Meyer, T. J., Finding

the Way to Solar Fuels with Dye-Sensitized Photoelectrosynthesis Cells. *Journal of the American Chemical Society* **2016,** *138* (40), 13085-13102.